ABSTRACT

Single-Electron Transistor: Effects of the Environment and Detecting Electron Motion in Real Time

by

Wei Lu

This thesis will be divided into two parts. In the first part, theory and results of a novel system in which a superconducting single-electron transistor (S-SET) coupled to a two-dimensional electron gas (2DEG) serving as a tunable electromagnetic environment for the S-SET will be discussed, including effects of dissipation, resonant tunneling with photon emission, and photon-assisted tunneling. In the second part, we discuss the techniques for which the SET is incorporated in an RF resonant circuit, resulting in an ultra high charge sensitivity and bandwidth. After the 2DEG is confined into a quantum dot, random telegraph signals (RTS) caused by individual electrons tunneling on and off the dot have been observed. In the equilibrium configuration, the occupational probabilities of the charge states of the dot can be directly measured from the RTS and were found to follow a Fermi distribution. In the non-equilibrium configuration, the RTS correctly detected the onset of the current through the dot.

Acknowledgments

I would never have made it through graduate school without help, encouragement, and guidance from many different people. I would like to give my heartfelt thanks to everyone who has provided me with such support.

First, I would like to thank Alex Rimberg, my advisor and the chairman of my thesis committee. Alex has provided me with advice, encouragement, and support throughout my graduate career. He has shown me the value of careful design, the importance of paying attention to the smallest detail, and the meaning of hard work. As the first student of the group, I have learned from Alex the operation of the SEM, the dilution fridge, and many other equipment as well. I am deeply indebted to him for being the kind of researcher I am today.

I would never have survived these years and finished this thesis without my wife, Xiao. She has been constantly giving me courage and support, and literally, a helpful hand when I was alone in the lab at midnight and needed some help to put the sample on the fridge.

I would like to thank the other members of my defense committee, Prof. Peter Nordlander and Prof. William Wilson, for their help and for the interest they showed in my work.

Thanks to Zhongqing Ji, my roommate at Tsinghua University and labmate since 2001, who has helped me a lot since he joined the lab. It is Zhongqing who fabricated the last couple of samples discussed in this thesis when I had started writing this thesis and looking for a postdoctoral position.

I would also like to thank my fellow graduate students in the lab, Michael Cox, Jennifer Steele, Madhu Thalakulam, Joy Sarkar and Sasa Zaric, for their help and friendship. I am also indebted to all my friends who helped my stay at Rice joyful.

Finally, I want to thank my parents, my brother, and my sister. Their love, encouragement, patience, and support have made possible my accomplishments and successes.

Contents

Abstract ii

Acknowledgments iii

List of Figures viii

List of Tables xix

1 INTRODUCTION **1**

2 THEORETICAL BACKGROUND **6**

2.1 Theory of the SET 6

2.1.1 SET in Normal State 7

2.1.2 SET in Superconducting State 11

2.2 Theory of Quantum Dots 14

2.2.1 2DEG in GaAs/AlGaAs Heterostructure 14

2.2.2 Quantum Point Contacts and Quantum Dots 16

3 EXPERIMENTAL TECHNIQUES **19**

3.1 Electron-Beam Lithography of Au Gates 19

3.1.1 Electron-Beam Resist System 19

3.1.2 Pattern Generation System 23

3.1.3 Sample Exposure 25

3.1.4 Evaporation 26

3.2 Fabrication of Al Junctions 27

3.2.1 Shadow Evaporation 27

3.2.2 Alignment 29

3.3 Ohmic Contacts 30

3.4 Chemical Etching 32

3.5 Refrigeration 35
3.5.1 Principles 35
3.5.2 Heat Sinks 38
3.5.3 Sample Wiring and Filtering 39

4 VERIFICATION OF THE ENVIRONMENTAL THEORY 42

4.1 Charge Tunneling Rates and Effects of The Environment 42
4.1.1 Single Junction In Normal State 42
4.1.2 $P(E)$ Function 45
4.1.3 Single Junction In Superconducting State 47
4.1.4 Double Junction System 50
4.2 Model System 53
4.2.1 Introduction 53
4.2.2 Sample Design 54
4.3 Theoretical Results 59
4.3.1 Calculation of Re$[Z_t(\omega)]$ 59
4.3.2 Model of the Environment 60
4.3.3 Calculation of $K(t)$ and $P(E)$ 67
4.3.4 Multisection Transmission Lines 71
4.3.5 Calculation of I-V Curves 74
4.4 Experimental Results 76
4.4.1 Measurements 76
4.4.2 Comparison with Theory 84
4.4.3 Discussion 91

5 OTHER DC RESULTS 95

5.1 SET Coupled to a Resonant Mode 95

5.1.1 $I(V, Q_0)$ Surface Plot 95
5.1.2 Emission of Photons into a Resonant Mode 99
5.1.3 Photon-Assisted Tunneling 105
5.2 SET Coupled to a Quantum Dot 107

6 REAL-TIME DETECTION OF ELECTRON MOTION 114

6.1 Radio-Frequency Single-Electron Transistor as a Fast Electrometer . . 114
6.1.1 Introduction 114
6.1.2 Principles 116
6.2 Experimental Setup 124
6.2.1 Sample Design 124
6.2.2 RF Set-Up 127
6.2.3 Characterization of the RF-SET 131
6.2.4 Characterization of the Dot 138
6.3 Real-time Results 140
6.3.1 "Change" Routine 141
6.3.2 Gate Dependence 144
6.3.3 "Bias" Dependence 148
6.3.4 Line Shape Analysis 151
6.3.5 Spectrum Analysis 156
6.4 Comparison of Tunneling Counts with Current 158
6.4.1 Improved Sample Design 158
6.4.2 Characterization of the Sample 160
6.4.3 Real-Time Results 163
6.5 Discussion 168

List of Figures

2.1 The SET consists of two tunnel junctions in series forming an island. The offset charge on the island and therefore its electrostatic potential is varied by the gate voltage V_g through the capacitance C_g . The transport voltage V induces a net flow of charge through the device, the value of current I being controlled by V_g 7

2.2 Schematic illustration for single-electron tunneling conditions. The parabolas represent the energy for $n = 0$ and $n = 1$ states vs offset charge Q_0, respectively. Tunneling processes can only happen when the energy provided by the bias eV is larger than the energy difference between the initial and final states. 9

2.3 The stability diagram of a normal state SET with $2C_2 = 10C_g = C_1$. The transistor conducts only outside the rhombic-shaped regions. Inside these regions, there is a constant number of electrons on the island. 10

2.4 Coulomb blockade oscillations of an SET for a fixed bias voltage $V < e/C_\Sigma$. Each current peak indicates the addition of a single electron. . 11

2.5 Schematic illustration of energetic requirements for Cooper pair and quasiparticle tunneling processes. A cooper pair tunnelling process (double line) will change n by 2, while a quasiparticle tunneling process (single line) changes n by 1 and requires sufficient energy to both break a Cooper pair and to satisfy the difference in charging energy. 13

2.6 Band bending diagram of a modulation doped GaAs/$Al_xGa_{1-x}As$ heterostructure. A 2DEG is formed in the undoped GaAs at the interface with the n-type doped AlGaAs. 15

2.7 Split gate scheme. The electrons under the gates are depleted, leaving a narrow channel under the gap. 16

2.8 Conductance of a quantum point contact as a function of the gate voltage. The conductance is quantized due to the discrete 1D conduction states. 17

2.9 Formation of a quantum dot using three pairs of gates. The two quantum point contacts serve as tunnel junctions while the island is formed by depletion of electrons under the central gates. 17

3.1 Schematic illustration of electron-beam lithography process. 21

3.2 A conventional electron microscope converted to an e-beam writer. The microcomputer is equipped with a commercial package, the Nanometer Pattern Generation System (NPGS), which interprets CAD drawings on the microcomputer to perform an exposure via control of the scan coils and beam blanker of the SEM. 24

3.3 Major steps involved in fabricating Al/AlO_x junctions. A hanging resist bridge is formed during the e-beam lithography process. A shadow evaporation technique is then used to produce the junction, which is a thin oxide layer sandwiched by two layers of Al evaporated from different angles. 28

3.4 Schematic drawing of the alignment process. Only the areas in the windows are exposed in this process. Adjusting the overlays to the alignment marks allows NPGS to calculate translation and rotation matrices. 30

3.5 ^{3}He/^{4}He mixture separates into two phases at low temperatures. Pumping on the ^{3}He dilute phase causes ^{3}He to diffuse across the phase boundary, thereby cooling the sample. 37

4.1 Schematic illustration of a double junction system coupled to a voltage source V via an external impedance $Z(\omega)$. 50

4.2 (a) Thevenin configuration: A voltage source V in series with the impedance $Z(\omega)$. (b) The equivalent Norton Configuration: A current source $I(\omega) = V(\omega)/Z(\omega)$ in parallel with the impedance $Z(\omega)$. . 51

4.3 Transformation of a double junction circuit into an equivalent effective circuit. (a) Original circuit as seen from the first junction. The second junction is treated as a capacitor. (b) Equivalent Norton configuration. (c) Effective circuit for tunneling through the first junction. 52

4.4 Schematic illustration of the sample, showing the ohmic contacts, Au gates and macroscopic pads for making contact to the SET. 55

4.5 Top: expanded view of the center of the sample, showing the Al/AlO_x tunnel junctions, and the depletion of the 2DEG. The energized gates are colored. Bottom: cross sectional view of the sample, showing the vertical coupling between the SET and the 2DEG. 56

4.6 Electron micrograph of a test sample. The white bar at the lower left represents 100 nm. The tunnel junctions are visible as overlaps between the leads and the island. The sizes of the junctions in this sample are about 50 nm $\times$ 50 nm, and the thickness of the oxide layer is about 10 Å. 58

4.7 Lumped-element circuit for the model system. The SET island is coupled to the macroscopic leads of impedance $Z_L(\omega)$ via tunnel junctions with resistance R and capacitance C. The island is also coupled by a capacitance C_{2D} to the 2DEG whose impedance to ground Z_{2D} can be tuned. 60

4.8 (a) $\mathrm{Re}[Z_t(\omega)]$ for three different environmental models, all based on a transmission line with $r_\ell = 2.9 \times 10^6\,\omega/\mathrm{m}$ and $c_\ell = 1.0 \times 10^{-8}\,\mathrm{F/m}$ and $\ell = 6.94 \times 10^{-4}\,\mathrm{m}$. For this graph we have used $Z_{2D} = 100\,\Omega$. Solid line: exact result based on the full forms for $Z_t(\omega)$ and $Z_L(\omega)$. Dotted line: approximate form based on the low frequency approximation to $Z_L(\omega)$ and the decomposition of $\mathrm{Re}[Z_t(\omega)]$. Dashed line: infinite line result for the same values of r_ℓ and c_ℓ. (b) Solid lines: $P_s(E)$ for the same transmission line parameters, for (top to bottom) $T = 10$, 20, 50, 100, 150, and 200 mK. Dashed line: $P(E)$ for an infinite RC line at $T = 0$. 66

4.9 $\mathrm{Re}[Z_t(\omega)]$ for four cascaded RC lines and a ground plane, using the parameters given in Table 4.1, for (top to bottom) $Z_{2D} = 6445$, 3227, 1291, 258 and 100Ω. Solid lines: exact calculation of $\mathrm{Re}[Z_t(\omega)]$. Dashed lines: approximate version of $\mathrm{Re}[Z_t(\omega)]$ as described in the text. . . . 73

4.10 Calculated $P^{(1)}_{\mathrm{tot}}(E)$ for S2, based on the transmission line parameters from Table 4.1 for a series of values of Z_{2D}. Top to bottom: $Z_{2D} = 0$, 65, 129, 258, 430, 645, 860, 1291, 1613, 2151, 3227, 4302 and 6445 Ω. Insets: $P^{(1)}_{2D}(E)$ for Z_{2D} equal to (a) 65 (b) 430 (c) 1291 (d) 3227 and (e) 6445 Ω. Note the scale change for $Z_{2D} = 65$ and 430 Ω. 75

4.11 Schematic illustration of a differential conductance measurement on the point contacts. The 50 mV signal is scaled down to 5 μV by a 10 $\Omega + 100$ KΩ voltage divider. 77

4.12 (a) Conductance of the quantum point contacts vs. gate voltage. (b) Conductance through the 2DEG for the pool (upper) geometry and stripe (lower) geometry. In both (a) and (b), the upper curve has been offset $2G_0$ for clarity. 79

4.13 Representative I-V curve for Sample 2 around zero-bias with an unconfined 2DEG. The linear region is $\approx \pm 8\,\mu$V. 81

4.14 (a)Zero-bias conductance of the SET as a function of V_g in the "pool" geometry. (b)Zero-bias conductance of the SET as a function of V_g in the "stripe" geometry. Numerous Coulomb blockade oscillations are observed in both cases due to change in V_g. Markedly different behaviors of the maximum values $G_{\rm SET}$ are observed in the two cases. 82

4.15 $G_{\rm SET}$ vs. V_g for S2 in the pool geometry for $T =$ (a) 50, (b) 100, (c) 150, and (d) 200 mK. 83

4.16 (a) Peak values of $G_{\rm SET}$ versus $G_{\rm 2D}$ for $T = 100$ mK ($\triangle$), 150 mK ($\diamond$), and 200 mK (+). Calculated values $G^c_{\rm SET}$ scaled to equal $G_{\rm SET}$ at its maximum value at $G^{\rm max}_{\rm 2D}$ at 200 mK are shown as the heavy solid lines. (b) On the left axis we plot measured $G_{\rm 2D}$ versus V_g (solid line), and the smooth function fitted to $G_{\rm 2D}$ vs. V_g (heavy dashed line). On the right axis we plot values of σ_{ch} in the pool geometry for $T = 100$ mK ($\triangle$), 150 mK ($\diamond$), and 200 mK (+). We also show σ_{ch} for the stripe geometry ($\circ$). 85

4.17 (a) I-V characteristics for S1 at an estimated electron temperature of 100 mK for an unconfined 2DEG ($\circ$), $V_g = -0.3$ V ($\square$), and $Z_{2D} = 1613$ ($+$), 2151 ($\diamond$) and 6453 Ω ($\times$). (b) Calculated I-V characteristics (top to bottom at peak) for $Z_{2D} = 0$, 129, 258, 430, 645, 860, 1613, 2151, 3227, 4302 and 6453 Ω. Here $\sigma_{ch} = 0$ for all curves. (c) Calculated I-V characteristics for (top to bottom) $\sigma_{ch} = 0$, 1, 2, 3, 4, 5, 6 and $7\times10^{-2}e$. Here $Z_{2D} = 0$ for all curves. (d) Calculated I-V characteristics for the same 2DEG condition as in (a). To fit the data at $V_g = 0$ and -0.3 V, we use $\sigma_{ch} = 0.07$ and $0.05e$, respectively. For the remaining curves we take $\sigma_{ch} = 0$. 90

4.18 G_{SET} measured at $C_gV_g = Ne$ for an unconfined 2DEG as a function of temperature. A non-monotonic behavior is observed. 93

5.1 Schematic illustration of a dc measurement on the SET. The sweep box generates two symmetric ramping voltages across the SET. The 2DEG is grounded in this measurement. 96

5.2 False color image of $I(V, Q_0)$ surface with 2DEG unconfined. A color table giving the current scale is shown at the bottom. Transition lines are calculated by the rules in Eq. 2.10. A contour plot is also added to the positive half of the image to accentuate the features. 98

5.3 Formation of the JQP cycle involving one Cooper pair tunneling through one junction followed by two consecutive quasiparticle tunneling through the other. This charge cycle is repeated many times and on average, a current flows from right to left through the SET. 100

5.4 Tunneling processes discussed in the text, for positive bias voltage and increasing island charge. 102

5.5 (a) Image plot of the I-V plane. Dotted line: J process. Dashed line: J-ph process. Solid line: e process. (b) Simulation results including JQP-ph processes. (c) Simulation results including both JQP-ph and PAT. 103

5.6 Main figure: simulated current with and without PAT. The inclusion of PAT increases the primary JPQ peaks for both J1 and J2. Insert: comparison of the simulation with and without PAT with the measured current. The inclusion of PAT brings the simulation in much closer agreement with the data. 107

5.7 An SET coupled to a quantum dot through a capacitance C_C . The dot and SET are biased independently by voltages V_1 and V_2. The gate capacitances C_s and C_d can have significantly different values. 108

5.8 (a) Current through the SET at $V_{bias} = 810$ μV, illustrating two oscillation periods. (b) Zero-bias conductance through the dot, showing simple Coulomb oscillations. A phase shift is visible at $V_g \approx -0.58$ V, when N_s changes by one. The inset shows an expanded view of I_s and G_d around -0.53 V. (c) Current through the SET at the same bias voltage when the dot is not formed. The different scales in (a) and (c) are caused by a change in the charging energy of the SET with and without the dot. 111

6.1 Schematic of the resonant circuit. The SET is represented by its differential resistance R_d. Z_0 is the characteristic impedance of the cable. V^+ and V_A are the incoming voltage and total voltage at points AA', respectively. 116

6.2 Schematic of the resonant circuit with the loss modelled by a resistance Z_i. 121

6.3 Simulation of $|\Gamma|$ as a function of frequency for (a) no extra loss (b) $Z_i = 10\,\Omega$ (c) $Z_i = 40\,\Omega$ and (d) $Z_i = 100\,\Omega$. The red lines represent the SET in blockade case, *i. e.*, the SET resistance $R_d \sim \infty$, and blue lines represent $R_d = 50\,\mathrm{k}\Omega$. The resonant frequency is not changed by the addition of Z_i. The bandwidth of the resonance does not change until $Z_i > 50\,\Omega$, in which case a crossover between the red and blue lines also occurs. 123

6.4 Electron micrograph of a sample based on the new design, with the dot schematically illustrated. Gates $\mathrm{G_{L1}}$, $\mathrm{G_{R1}}$ form one point contact while $\mathrm{G_{L2}}$ and $\mathrm{G_{R2}}$ form the other. Gate $\mathrm{G_d}$ is used to control the dot offset charge. 125

6.5 Schematic of the RF-SET circuit. Showing the various devices used at different temperatures. 128

6.6 Photo of the insert, showing the various components used in the RF-SET measurement. 132

6.7 (a) Power of the reflected signal for sample S4 as a function of frequency for $R_d \sim \infty$ (blue) and $R_d = 39\,\mathrm{K}\Omega$ (red). (b) Shot noise power in the reflected signal. The red curve is taken as the difference of the shot noise power measured at $I_{\mathrm{SET}} = 8\,\mu\mathrm{A}$ and $I_{\mathrm{SET}} = 1\,\mu\mathrm{A}$, and the blue curve is a fit which gives $\omega_0 = 1025\,\mathrm{MHz}$. 134

6.8 Representative I-V curves for sample S5 with $R_n = 25\,\mathrm{K}\Omega$. The optimal working point is between the $3e$ peak and the JQP peak as indicated by the arrow. The optimal size of the carrier wave is also illustrated. 135

6.9 (a) Modulation of the reflected signal corresponding to a 100 KHz, $0.05e$ rms offset charge excitation on the SET of S6. (b) The offset charge excitation is clearly captured by the digital scope after the mixer. No averaging is performed. 137

6.10 (a) Current through the SET as a function of gate voltage V_g for sample S4. The size of the oscillation caused by dot charge change increases gradually as the total capacitance of the dot decreases. (b) Conductance of the dot taken simultaneously. (c) Current through the SET when the dot is more closed. The size of oscillations caused by changes in the dot charge is much larger than that in (a). (d) Current through the SET vs. V_g for sample S6 when the dot is sufficiently closed. Oscillations caused by dot charge change are again visible. 139

6.11 Representative switching events captured by the scope. 141

6.12 (a) Number of switching events as a function of V_g. (b),(c), representative data in real time record captured by the scope at points A and B in (a), respectively. There are fewer switching events at point B, with a longer dwell time. 146

6.13 Evolution of the count peaks as a function of the gate voltages. V_1 and V_2 are increased by 9.3 mV after each V_g sweep. 147

6.14 (a),(c) Counts (n) of switching events as a function of $V_{\rm bias}$ and V_g when the bias voltage is applied on the "source" side in Fig. 6.4, with different QPC formations in (a) and (c). (b) $n(V_{\rm bias}, V_g)$ image when the bias voltage is applied on the "drain" side of the dot. (d) $n(V_{\rm bias}, V_g)$ image when the bias voltage is applied symmetrically. 149

6.15 (a) Calculated occupational probabilities (blue squares: P_0, red circles: P_1) from the real time measurements as a function of Q_0 near a degeneracy point. The solid lines are a fit based on Fermi distribution. Left inset: real time data for $Q_0 = 0.39e$; right inset: real time data for $Q_0 = 0.59e$. (b) Evolution of the"capture" rate (blue squares) and "escape" rate (red circles) as a function of Q_0. The solid lines are calculated from Eq. 6.47, with no adjustable parameters used. 155

6.16 (a) Spectra (markers) of the signal at three representative peaks as the gate voltage is increased. The solid lines are least square fits using Eq. 6.49. (b) Histogram of the dwell time on the "1" state for switching events corresponding to the red curve in (a). The solid line is a fit based on an exponential decay. 157

6.17 Electron micrograph for the improved sample design. The edge of the etched region is clearly visible. By completely etching the 2DEG away on the left side of the dot, the side channel is closely naturally. 159

6.18 (a) Current through the SET as a function of gate voltage V_g. The small "bumps" at higher V_g are caused to changes in dot charge. The size of the bumps increases gradually as the total capacitance of the dot decreases. (b) Conductance of the dot taken simultaneously. . . . 161

6.19 (a) Spectrum of the reflected RF signal around the carrier wave frequency for S7. The side peaks correspond to a $0.05e$ rms offset charge excitation. (b) Current through the SET vs. Q_0. High sensitivity can only be obtained within a limited region for S7 as indicated by the arrows. 162

6.20 Induced current I_C (red curve) from the counts of the switching events as a function of the dot bias voltage. No adjustable parameters are used. The blue curve is the absolute value of the measured DC current I_d for comparison. Inset: blue curve, same I_d data as in the main figure; green curve, I_d measured at a different gate voltage for which the gap is narrower. 164

6.21 Schematic illustration of the condition in which the bias voltage V_{bias} is just below the threshold voltage. Thermally activated electrons can tunnel through the left junction. Once there, the electron can either tunnel back through the same junction or forward through the right junction. 167

6.22 Schematic illustration of the setup for which an RF-SET is coupled to a single junction formed by a QPC. Six other QPCs serve as high impedance leads to the junction. 170

List of Tables

4.1 Transmission line parameters for the various sections of the sample leads, with w and ℓ in μm, r_ℓ in MΩ/m, c_ℓ in nF/m, $r_\ell\ell$ in Ω, and $\mathcal{T}$ calculated for $T = 100\,\mathrm{mK}$. 72

4.2 Parameters for samples S1 and S2. Capacitances are in aF, energies in μeV, and resistances in KΩ. 78

6.1 Properties of samples S3–S6, where R_n and E_C are the normal-state resistance and charging energy of the SET, respectively. f_C is the frequency at which maximum gain is achieved on the RF-SET. δq is measured charge sensitivity with a $0.05e$ offset charge excitation for an unconfined 2DEG. 2DEG substrate for sampless S3 and S4 was provided by Dr. Gossard at UC Santa Barbara with 2DEG located 50 nm below surface, while the substrate for samples S5 and S6 was provided by Dr. Pfeiffer at Bell Labs with 2DEG located 190 nm below surface. 127

6.2 Parameters for the various amplifiers used in the RF-SET measurement. The noise temperature T_n for the cold amplifier is estimated as described in the text. T_n for the other amplifiers are obtained from manufacture specifications. 131

CHAPTER 1

INTRODUCTION

Single-electron tunneling processes have recently invoked a lot of interest for both reasons of fundamental scientific interest [1] and potential technological application [2]. Recently, single-electron tunneling has been observed in lithographically patterned structures whose dimensions are only a few tens of nanometers [3, 4], in nanocrystals [5], in carbon nanotubes [6–8], and in single molecules [9, 10]. Because tunneling is inherently quantum-mechanical, it is ideally described by a Schrödinger equation containing the internal degrees of freedom of the nanostructures involved. In the real world however, no system exists in isolation. A more accurate description of tunneling must take into account external degrees of freedom, which are often termed "the environment." The environment usually involves many degrees of freedom and is often dissipative. A large body of theoretical work has been devoted to incorporating such dissipative phenomena in a conservative Hamiltonian description [11–13]. The interaction between quantum variables and their environment remains a topic of considerable interest today, in connection with the fields of quantum computation [14, 15] and mesoscopic transport [16].

Previous studies of the effects of the environment have often involved system of either normal metal or Josephson tunnel junctions [17]. While in many experiments care was taken to ensure that the environment was well-characterized [18–20], and some variation was achieved [21], in general dissipation was not a tunable parameter. Recently, however, it has been demonstrated that well-characterized experimental systems can be fabricated in which some part of the environment can be tuned *in*

situ [22]. Moreover, since tunneling is extremely sensitive to the nature of its environment, tunnel junctions also provide a form of sensor for investing the electrodynamic structure of their surroundings. This capability should allow for the study of the impedance and energetic structure of nanostructures at very low power levels (typically sub-picowatt) without direct electrical contact, only capacitive coupling. The results of such measurements can provide information of interest to numerous disciplines involved in nanoscale science and technology.

On the other hand, the SET is an ultra-sensitive electrometer and has long been proposed to detect charge motion in real time in another mesoscopic device. Such true electron counting experiments will provide direct measurement such as temporal electronic correlations [23]. Although there is ample evidence that such correlation exist [18], electron dynamics in engineered nanostructures have been observed directly only on very long time scales, usually in an electron trap geometry [24]. The faster dynamics associated with electrical currents or charge fluctuations [25] are usually inferred from DC or quasi-DC measurements. Recently, interest in electron dynamics has risen, in part due to the realization that additional information about electronic interactions can be found in the shot noise [26] or higher statistical moments [27, 28] of a DC current. Furthermore, interest in quantum computation has stimulated investigation of qubit readout [29, 30], which for many condensed matter systems ultimately reduces to single-shot measurements of individual electronic charges.

Two types of experiments will be discussed in this thesis to address these two interesting issues. The structure on which we have based our investigation consists of an island linked to macroscopic leads by two Al/AlO_x tunnel junctions, and surrounded by several gates which control the tunneling of individual electrons. Such a device is referred to as an "single electron transistor" (SET). The substrate on which the SET is fabricated contains a $GaAs/Al_xGa_{1-x}As$ heterostructure. A layer of two-

dimensional electron gas (2DEG) forms between GaAs and $Al_xGa_{1-x}As$ layers [31] about 50 nm or 190 nm below the surface in our samples. By applying sufficient negative voltages on the gates surrounding the SET, the 2DEG beneath the gates can be depleted and its impedance adjusted. The tunability of the SET/2DEG system makes it well suited for the problems we want to investigate.

In the first type of experiments, the 2DEG is treated as an environment which is strongly coupled to the SET. and the impedance of the environment can therefore be tuned *in situ*. Corresponding changes in the transport properties of the SET may then be observed.

We have developed a model based on the environmental theory [17] in which both the SET lead and 2DEG impedances are accounted for. Good agreements are achieved between the measured SET conductance and the theory as the dissipation in the 2DEG is monotonically increased. The I-V behavior of the SET at low biases are well predicted by a model including both the environmental theory and low-frequency variations in the SET offset charge.

The SET behavior is also studied at higher biases, in which we have observed phenomena associated with resonant tunneling of Cooper pairs with photon emission into a resonant mode. Photon-assisted tunneling phenomena is also observed and good agreement between the data and theory is once again achieved for this strongly coupled SET/2DEG system.

In the second type of experiments, we have confined the 2DEG into a quantum dot, and used the radio-frequency single-electron transistor (RF-SET) technique [32] to perform real electron counting on the dot. Random telegraph signals (RTS) corresponding to individual electron tunneling on and off the dot have been observed in our system. By calculating the number of switching, the tunneling rate of the dot can be measured directly. Gate and bias dependence measurements have verified

that the RTS are indeed caused by electron tunneling on or off the dot, instead of caused by charge traps. From the real time data, we have studied the charge occupational probabilities near a charge degeneracy point of the dot, and found they follow a Fermi-Dirac distribution. Dwell time in each charge state and associated tunneling rates are also studied. Power spectrum analysis of the RTS verified that the tunneling is a Poisson process. Finally, non-equilibrium properties of the dot is also studied by driving a current through the dot. Comparison between the derived current from the counts of switching and directly measured DC current agrees with a thermally activated tunneling model.

A brief overview of the structure of this thesis is as follows:

In **Chapter 2** we will discuss the theory of single-electron tunneling. We will present a very simple semiclassical description of the behavior of a simple SET in the normal state, and extend the theory to an SET in the superconducting state. We will then briefly discuss the effects of the environment on transport properties of the SET and the model system we designed to study those effects. In the end, we will discuss the case of an SET coupled to a quantum dot, *i. e.*, a double dot system.

In **Chapter 3** we will discuss the experimental techniques used in obtaining our results. These include sample design, sample fabrication, cryogenic techniques, low-noise electronic techniques, and data acquisition techniques.

In **Chapter 4** we present the first type of measurements to systemically test the environmental theory. We will first present an introduction of the environmental theory, followed by a model based on our system. Numerical results based on this model will also be given and compared with experimental data.

In **Chapter 5** we will discuss results obtained on the SET/2DEG system at higher voltage biases. Such results include Cooper pair tunneling with photon emission into a resonant mode and photon-assisted tunneling. We will also demonstrate that the

SET is an ultra-sensitive electrometer to changes in the dot charge.

Finally in **Chapter 6** we will discuss the true electron counting experiments performed on a strongly coupled SET/quantum dot system, using the RF-SET technique. Both equilibrium and non-equilibrium properties of the dot can be analyzed by counting the switching in the RF-SET signal, and the results from such real time measurements agree well with predictions of a theory for a two-level system. Discussions and future experiments are given in the end.

CHAPTER 2

THEORETICAL BACKGROUND

In this chapter we give a theoretical overview of the experiment. The discussion is organized as follows: Section 2.1 discusses the theory of a single SET, in both the normal and superconducting states. Section 2.2 describes quantum dots and their formation in a semiconductor heterostructure. Sections 2.3 and 2.4 discuss the effects of the environment on the SET, and the model system we designed to study those effects, respectively. In Section 2.5 we will give an description for an extreme case when the environment consists of a quantum dot. All of the discussion in this chapter is in the $T = 0$ limit.

2.1 Theory of the SET

A single-electron transistor (SET) consists of two ultra small tunnel junctions and an "island" between them, usually with a third gate electrode capacitively coupled to the island, as illustrated in Fig. 2.1. The first observation of single charge tunneling in microfabricated samples was made by Fulton and Dolan [33] in a similar structure.

When the island of the SET is metallic, (usually Al), it contains billions of electrons, and the energy spectrum can be disregarded. We can then treat the SET semiclassically.

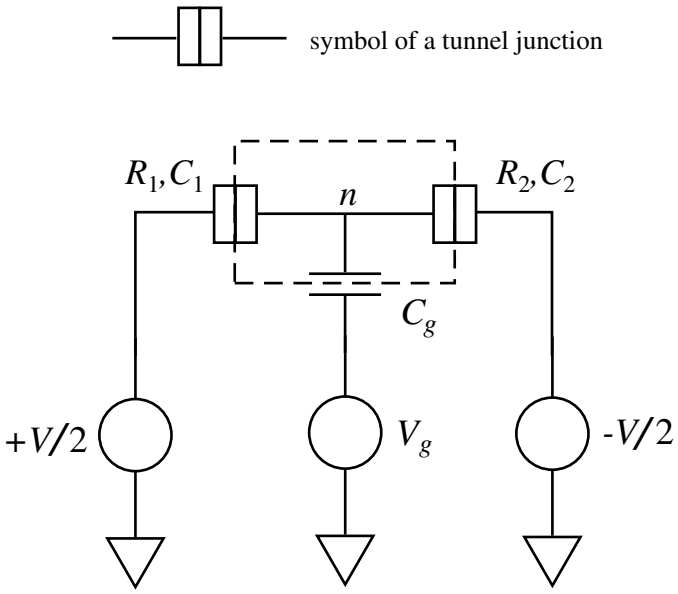

Figure 2.1: The SET consists of two tunnel junctions in series forming an island. The offset charge on the island and therefore its electrostatic potential is varied by the gate voltage V_g through the capacitance C_g . The transport voltage V induces a net flow of charge through the device, the value of current I being controlled by V_g .

2.1.1 SET in Normal State

Suppose that the SET is in the normal state. Let R_T and C denote the resistance and capacitance of a tunnel junction. In what follows, we assume that the following two conditions are satisfied. First, we assume the island is small enough and the temperature low enough that the Coulomb energy corresponding to one excess electron $E_C = e^2/2C$ is large compared to the ambient thermal energy k_BT , *i. e.*

$$E_C \gg k_BT \tag{2.1}$$

Second, we assume the lifetime due to tunneling $\tau_r = R_TC$ is much larger than the uncertainty time $\Delta t \sim h/2E_C$ associated with the Coulomb energy E_C . This ensures that the wave function of an excess electron on the island will be localized

there. This assumption requires

$$R_T \gg R_K \tag{2.2}$$

where $R_K = h/e^2 \simeq 25.8\ k\Omega$ is the resistance quantum.

Under these conditions, the system is in the well-known Coulomb-blockade regime [34], and the excess charge on the island is well defined. When an electron tunnels onto the island, it will change the net charge of the island by e, thereby increasing the potential of the island. The change in the island potential due to the presence of the excess electron can be large enough to affect subsequent tunneling of other electrons. For the system illustrated in Fig. 2.1, when an electron tunnels across the first junction hence changing the net electrons on the island from n to $n+1$, the electrostatic energy difference is found to be

$$\Delta E_1 = \frac{e[(C_2 + \frac{1}{2}C_g)V - C_g V_g + ne - \frac{e}{2}]}{C_\Sigma} \tag{2.3}$$

where

$$C_\Sigma = C_1 + C_2 + C_g \tag{2.4}$$

is the total capacitance of the island. In Eq. 2.3 the gate voltage V_g only appears in the combination $C_g V_g - ne$, so that $C_g V_g$ acts effectively as an offset charge $Q_0 = C_g V_g$ on the island. Thus, by adjusting V_g we can control Q_0, hence the electrostatic potential of the island.

For an electron to tunnel onto the island through junction i ($i = 1$ or 2), the transition must be electrostatically favorable, requiring $\Delta E_i > 0$. A straightforward analysis of Eq. 2.3 then gives the tunneling rule

$$\kappa_i e V(Q_0) \geq 2E_C[(-1)^{i-1}(\frac{Q_0}{e} - n) + \frac{1}{2}] \tag{2.5}$$

where

$$\kappa_i = \tfrac{1}{2} + (-1)^i (C_1 - C_2)/2C_\Sigma \tag{2.6}$$

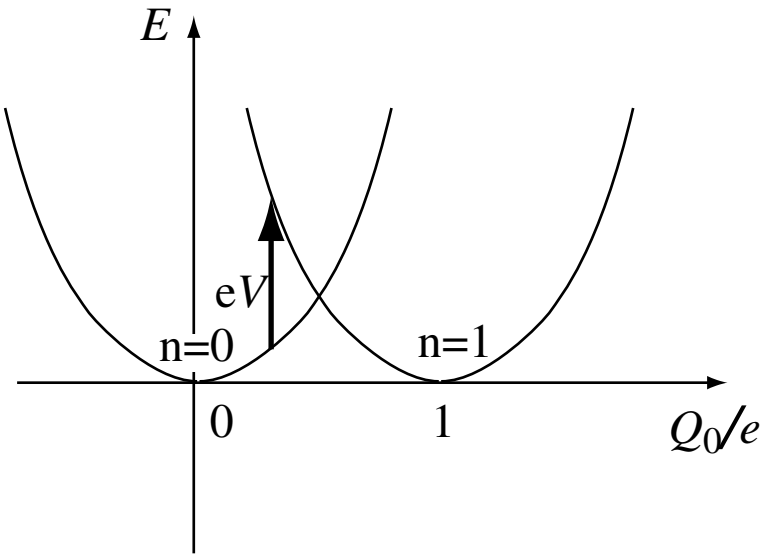

Figure 2.2: Schematic illustration for single-electron tunneling conditions. The parabolas represent the energy for $n = 0$ and $n = 1$ states vs offset charge Q_0, respectively. Tunneling processes can only happen when the energy provided by the bias eV is larger than the energy difference between the initial and final states.

determines the fraction of the applied bias voltage appearing across junction i, and

$$E_C = e^2/2C_\Sigma \tag{2.7}$$

is the Coulomb charging energy of the island. This energetic requirement is illustrated in Fig. 2.2, in which an electron can tunnel onto the island thereby changing n from 0 to 1 only when eV is larger than the energy difference between the $n = 1$ and $n = 0$ states. This energy difference can be tuned by adjusting V_g and hence Q_0. For example, when $Q_0 = e$, the required energy is largest; while when $Q_0 = \frac{1}{2}e$, the two charge states are degenerate and no excess energy is required.

By considering tunneling events on and off the island through each junction, it can be shown [17] that the state with n electrons on the island of the SET is stable

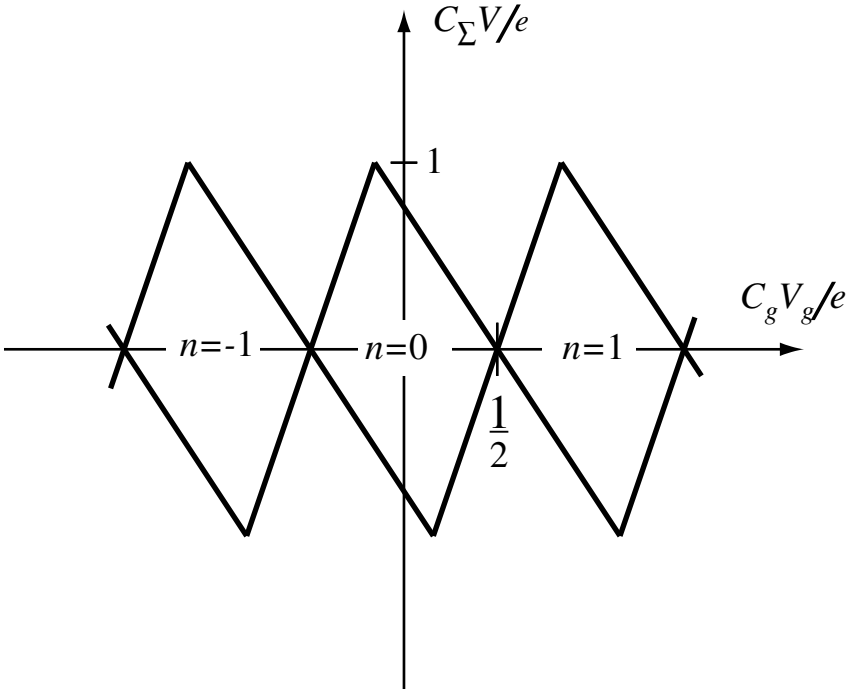

Figure 2.3: The stability diagram of a normal state SET with $2C_2 = 10C_g = C_1$. The transistor conducts only outside the rhombic-shaped regions. Inside these regions, there is a constant number of electrons on the island.

with respect to tunneling across the first and second junctions for voltages satisfying

$$e(n - \frac{1}{2}) < C_g V_g + (C_2 + \frac{1}{2}C_g)V < e(n + \frac{1}{2})$$
$$e(n - \frac{1}{2}) < C_g V_g - (C_1 + \frac{1}{2}C_g)V < e(n + \frac{1}{2}) \quad (2.8)$$

respectively. Hence, in the V_g-V plane rhombic-shaped regions form along the V_g axis within which the island is charged with a fixed number of excess electrons, as illustrated in Fig. 2.3. Inside these rhombi all transitions are suppressed by Coulomb blockade and no current flows through the device.

If we apply a fixed bias voltage $V < e/C_\Sigma$, and change the offset charge on the island by sweeping the gate voltage V_g monotonically, periodic current peaks will be

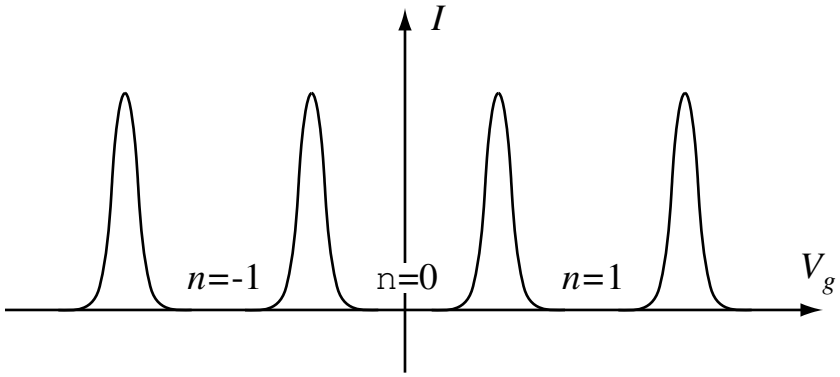

Figure 2.4: Coulomb blockade oscillations of an SET for a fixed bias voltage $V < e/C_\Sigma$. Each current peak indicates the addition of a single electron.

observed corresponding to the island charge moves from one stable region to another. This phenomena gives rise to the well-known "Coulomb blockade oscillations", as illustrated in Fig. 2.4.

2.1.2 SET in Superconducting State

Ultra small Al/AlO_x barriers (lateral dimensions below 100 nm) are commonly used as tunnel junctions in a metallic SET due to the high quality native oxide which grows on Al. If the leads and central island of the SET are made of Al, they will become superconducting at sufficiently low temperatures. In this case, the carriers are Cooper pairs and quasiparticles instead of electrons. For an SET with both superconducting leads and a superconducting island (S-SET), there are three important energy scales: the superconducting energy gap Δ, the charging energy E_C and the Josephson coupling energy E_J given by the Ambegaokar-Baratoff relation [37]:

$$E_J = h\Delta/8e^2R. \tag{2.9}$$

In this thesis we are concerned with the limit $E_J \ll E_C$, for which the number of Cooper pairs n on the island is well-defined, and the system is governed by the charging energy of the island. If instead $E_J \gg E_C$, the island charge is no longer well defined, and the system is governed by the phase difference across the superconducting tunnel barriers.

Similar to the normal state SET case, tunneling rules can be calculated with some modifications:

- When a Cooper pair tunnels across a junction, it will change the island charge by $2e$.
- Quasiparticles can only be created after a Cooper pair is broken, in this case an excess energy larger than the gap energy Δ must be provided.
- Cooper pair tunneling, unlike quasiparticle tunneling, is dissipationless, *i. e.* the energy provided by the bias eV must be exactly the same as the energy difference between the initial and final states.

The transition rule in Eq. 2.5 now becomes

$$m\kappa_i eV(Q_0) = 2mE_C[(-1)^{i-1}(\frac{Q_0}{e} - n) + \frac{m}{2}] + q\Delta \tag{2.10}$$

where $\kappa_i V$ is the effective voltage on junction i, as defined in Eq. 2.6, m is the number of electrons transferred and q the number of quasiparticle created in the tunneling process [41].

For a Cooper pair tunneling process, two electrons are transferred at once and no quasiparticle is created. We have $m = 2, q = 0$.

For a quasiparticle tunneling process, a Cooper pair is broken, and a "quasihole" is left on the other side of the junction. We have $m = 1, q = 2$. Since this process

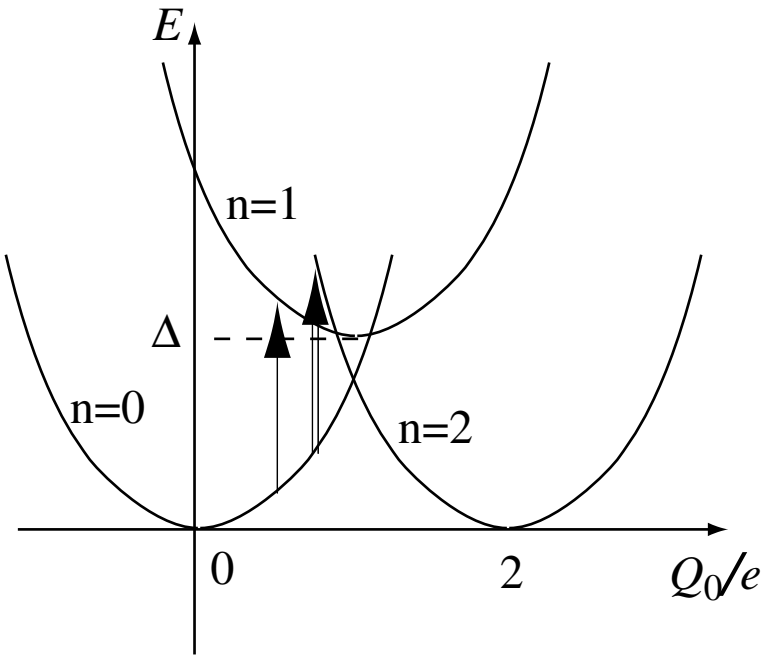

Figure 2.5: Schematic illustration of energetic requirements for Cooper pair and quasiparticle tunneling processes. A cooper pair tunnelling process (double line) will change n by 2, while a quasiparticle tunneling process (single line) changes n by 1 and requires sufficient energy to both break a Cooper pair and to satisfy the difference in charging energy.

requires sufficient energy to break a Cooper pair, it is more pronounced at higher bias, while Cooper pair tunneling dominates at lower biases.

Notice also that Eq. 2.10 gives a threshold for quasiparticle tunneling, but a resonant condition for Cooper pair tunneling.

In an ideal system, the states with an odd number of electrons on the island are of energy Δ higher than those with an even number of electrons, due to the increased free energy associated with the unpaired electron [38–40]. The energy diagram of an S-SET and tunneling rules are then illustrated in Fig. 2.5.

2.2 Theory of Quantum Dots

A quantum dot, by its name, is a zero-dimensional system. Various types of quantum dots, including those formed by molecules and nanofabricated in semiconductors have been studied. The type of quantum dot we will concentrate on is lithographically defined in a semiconductor heterostructure. A quantum dot is also an SET in that it also consists of two tunnel barriers and a central island. Unlike a metallic SET, a quantum dot usually contains only a few hundred electrons due to the low sheet density and small effective mass associated with the semiconductor forming the island. As a result, energy level structure of the electron states is present along with the normal Coulomb blockade phenomena.

2.2.1 2DEG in GaAs/AlGaAs Heterostructure

The quantum dot in our system is formed by lateral confinement of a two-dimensional electron gas (2DEG) present in a GaAs/$Al_xGa_{1-x}As$ heterostructure, created by growing a layer of $Al_xGa_{1-x}As$ on top of a GaAs substrate using molecular beam epitaxy (MBE) [43]. Typically, the Al mole fraction $x = 0.3$. The band-bending diagram of such a structure is illustrated in Fig. 2.6. A conduction band offset of about 0.3 V forms at the GaAs/AlGaAs interface due to the larger bandgap of AlGaAs. Furthermore, the AlGaAs layer is usually n-doped. As a result, in equilibrium the Fermi level at the interface lies inside the conduction band of the GaAs layer, which assures that electrons will be present at the interface even at $T = 0$. These electrons are confined by the potential well formed at the interface, and by the attractive electrostatic potential due to the positively charged ionized donors in the AlGaAs layer. To reduce scattering from the charged donor ions, the doped layer is separated from the interface by an undoped AlGaAs spacer layer. Two-dimensional subbands are formed

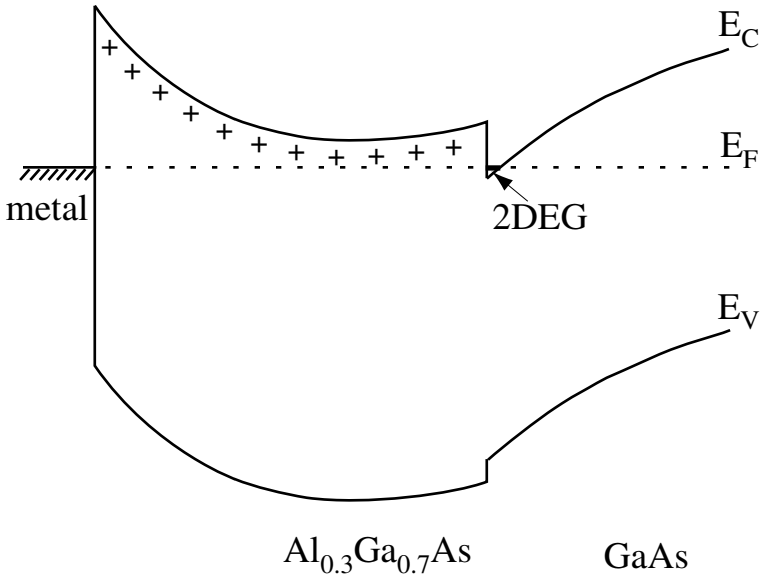

Figure 2.6: Band bending diagram of a modulation doped GaAs/$Al_xGa_{1-x}As$ heterostructure. A 2DEG is formed in the undoped GaAs at the interface with the n-type doped AlGaAs.

as a result of confinement perpendicular to the interface and free motion parallel to the interface. Usually, only a single two-dimensional subband (associated with the lowest discrete confinement level in the well) is populated, which gives us the so-called "two dimensional electron gas."

If metal gates are fabricated on the surface, and a large enough ($\sim$ 0.3V) negative bias is applied on them, the 2DEG beneath them will be depleted. We can think this of either as repulsion from the negative biased gates or as lowering of the Fermi level in GaAs. Increasing the voltage will deplete the 2DEG in a larger region surrounding the gates due to fringing fields.

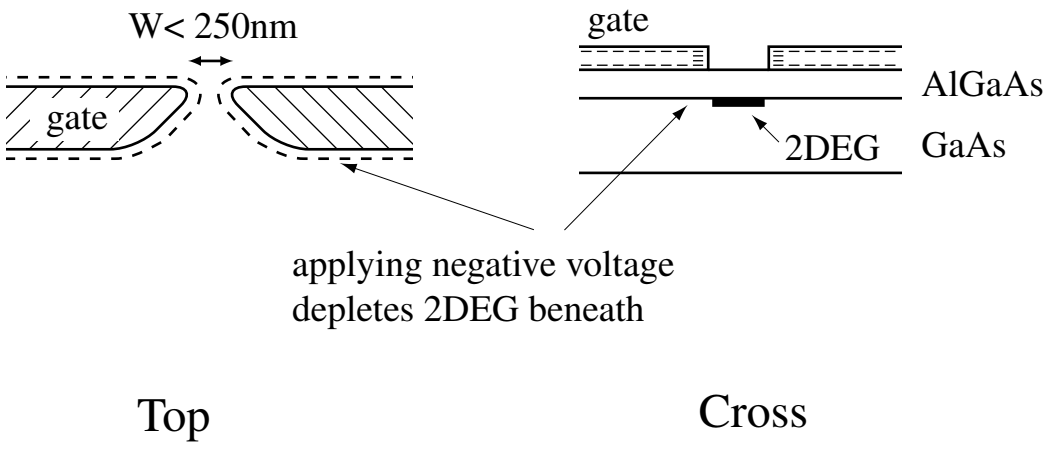

Figure 2.7: Split gate scheme. The electrons under the gates are depleted, leaving a narrow channel under the gap.

2.2.2 Quantum Point Contacts and Quantum Dots

In a split gate scheme [44, 45], a negative voltage is applied on two gates pointing toward each other, as illustrated in Fig. 2.7.

Wide 2DEG regions under the gate are depleted, leaving a narrow channel under the gap. If the gap is small enough, typically < 250 nm, and the voltage large enough, the 2DEG in the channel will split into a series of one-dimensional subbands, forming a so-called quantum point contact (QPC) [46, 47]. The conductance G of such a point contact is quantized due to the discreteness of the 1D levels [48]. Each 1D conductance channel acts as an electron waveguide and provides a conductance of $2e^2/h$, where the factor of 2 arises from spin degeneracy. Thus we get

$$G = (2e^2/h)N = 2G_0N \tag{2.11}$$

where N is the number of subbands occupied, and e^2/h is usually referred to as G_0, the conductance quantum. Increasing the gate voltage will depopulate the 1D subbands, thereby decreasing N. Fig. 2.8 shows a schematic illustration of point

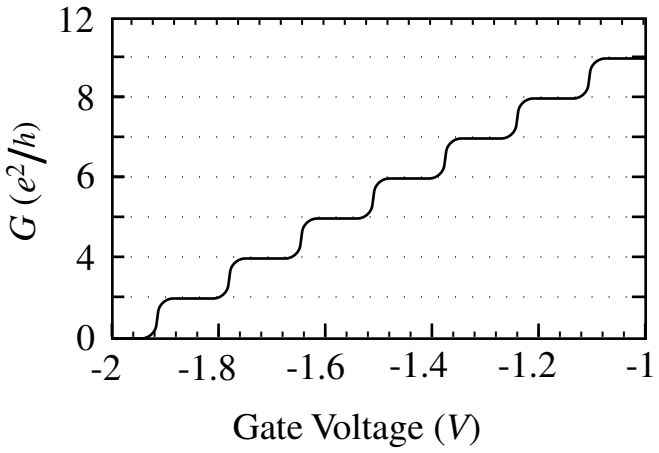

Figure 2.8: Conductance of a quantum point contact as a function of the gate voltage. The conductance is quantized due to the discrete 1D conduction states.

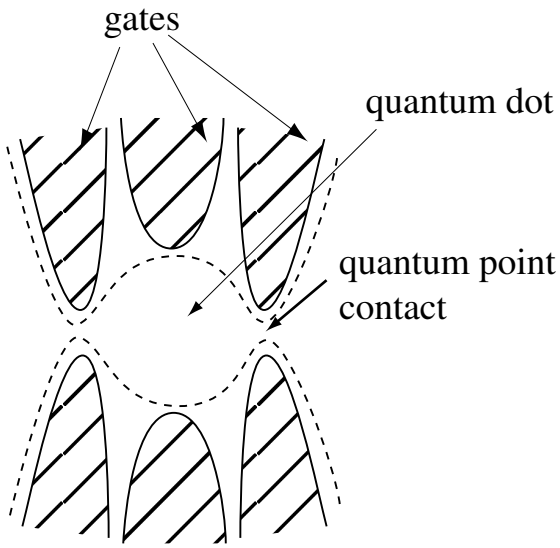

Figure 2.9: Formation of a quantum dot using three pairs of gates. The two quantum point contacts serve as tunnel junctions while the island is formed by depletion of electrons under the central gates.

contact conductance G vs. gate voltage V.

A quantum dot can by formed by putting two narrow split gates in series with another pair of more widely spaced gates, as illustrated in Fig. 2.9. An island will be formed in the center with the two point contacts serving as tunnel barriers when proper voltages are applied on the gates.

CHAPTER 3

EXPERIMENTAL TECHNIQUES

This chapter describes some of the basic experimental techniques we use in fabrication and measurement of the samples. We start by discussing the most important technique in our sample fabrication, namely electron-beam lithography in sections 3.1, and 3.2, which also cover other techniques like shadow evaporation and aligning two patterns together. Section 3.3 describes techniques to make Ohmic contacts to the 2DEG while Section 3.4 describes ways to remove unwanted 2DEG via chemical etching. Section 3.5 deals with the problems associated with low-temperature, small signal measurements.

3.1 Electron-Beam Lithography of Au Gates

A standard electron-beam lithography process involves depositing resist layers on the sample, exposing the sample to a high energy electron beam, developing the exposed area, evaporating material on the sample and liftoff. This process is used to fabricate the Au gates we will use to define the quantum dot. It is illustrated in Fig. 3.1.

3.1.1 Electron-Beam Resist System

Electron-beam lithography is widely used to produce features with size < 500 nm. Unlike photo-lithography, whose resolution is limited by the wavelength of light to

a few hundred nanometers, the resolution of electron-beam lithography is limited by the spot size of backscattered electrons to $\sim$ 50 nm in our systems. Like photolithography, e-beam lithography depends on selective exposure of a resist which is sensitive to ionizing radiation. There are two kinds of resists. In a positive resist, exposure to the electron beam breaks the bonds holding together the monomers in a resist molecule. The weakened part of the resist can then be removed by a weak solvent (developer) while the unexposed resist remains. In a negative resist, exposure to the electron beam causes bonds (crosslinks) to form between the monomers of different resist molecules, hardening the resist and making the exposed areas insoluble to particular solvents. Positive resists are more widely used. The particular resists we use are polymethylmethacrylate (PMMA) and polymethylmethacrylate-methacrylic acid (PMMA-MAA), both positive resists. The critical energy needed in a volume of positive resist for the resist to be soluble in a developer is called the critical irradiation ε_c. In practice, the known quantities in an exposure are the beam current density and the exposure time, which in turn determine the number of electrons (the dose) received by the resist. The critical dose D_c is proportional to ε_c for fixed incident electron energy, resist thickness, substrate type and so forth. In practice, the proper dose is determined experimentally.

A bilayer PMMA system [54, 55] is used in our lab for fabrication of Au gates. The motivation for using a system of this sort is to produce an undercut resist profile as shown in Fig. 3.1. The low molecular-weight bottom layer is more sensitive to irradiation than the high molecular-weight upper layer, since fewer bonds must be broken to make the lower layer soluble. As a result, more of the lower layer will be removed during the development, leaving some overhanging high molecular-weight resist. An undercut profile facilitates liftoff by minimizing the chance of connection between the metal deposited on the resist and that on the surface of the sample.

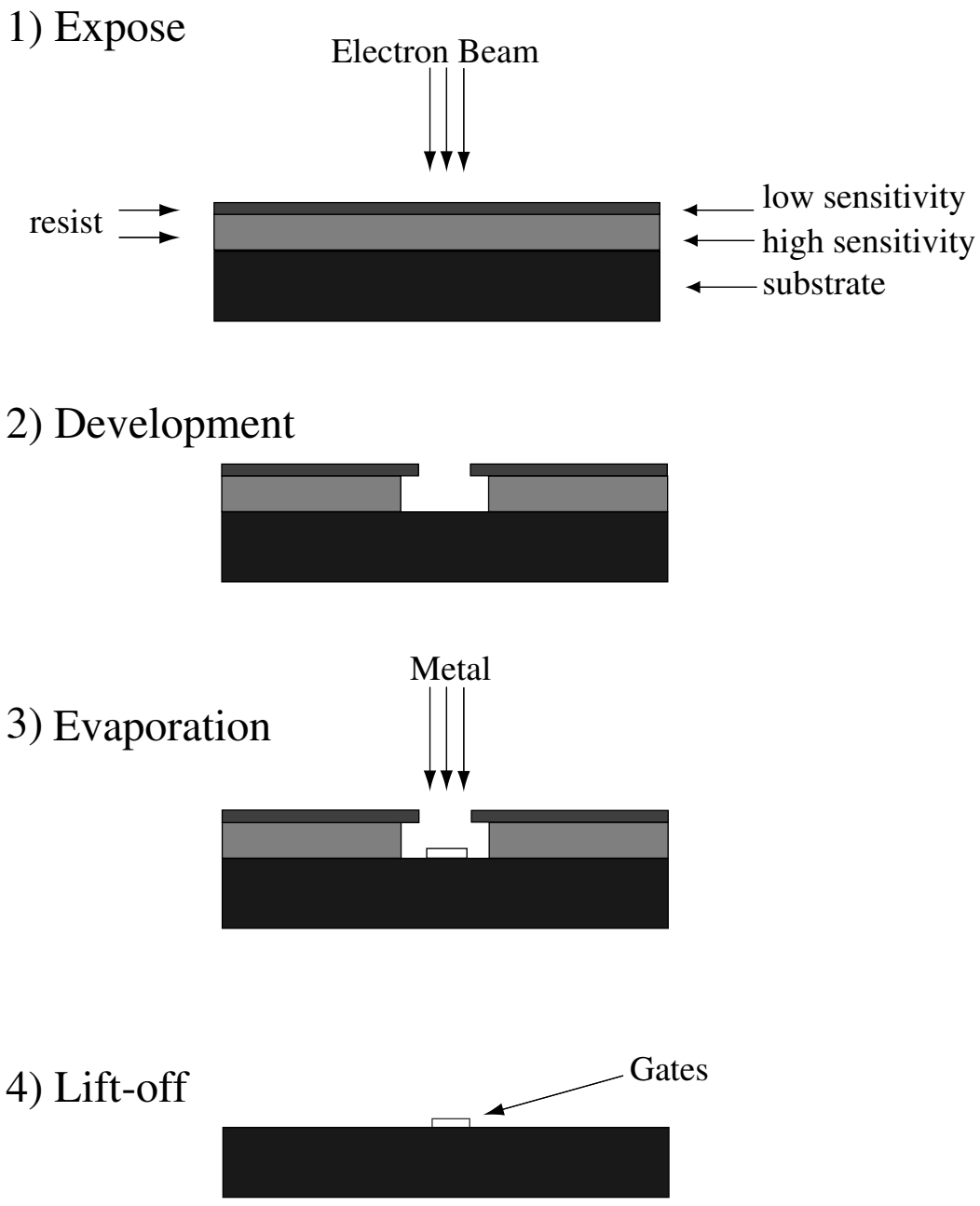

Figure 3.1: Schematic illustration of electron-beam lithography process.

Liftoff can therefore be accomplished easily with layers of deposited metal up to $\sim 1/3$ of the thickness of the lower resist layer. Bilayer systems also help to reduce the minimum linewidth, which is determined by the exposed area in the upper resist layer. This area is reduced since fewer electrons scattered from the substrate surface reach the upper layer of resist.

The particular bilayer resist we use to fabricate Au leads consists of a lower layer of 495 K PMMA and an upper layer of 950 K PMMA, both 4% in anisole, fabricated by Microlithography Chemical Corp. The thickness of the lower and upper layers is roughly 300 nm and 100 nm respectively.

A typical sequence of steps in producing a bilayer resist is as follows:

1. Clean sample in acetone (ACE) ultrasound for 20 min. Rinse the sample in isoproponal (IPA) afterwards since ACE evaporates rapidly and may leave residue on the surface. Blow sample dry with an air gun.

2. Clean a glass pipette in ACE ultrasound for 10 min, followed by rinsing in IPA and blow dry.

3. Apply a drop of 495 K PMMA on the sample. Immediately start the spinner; spin @ 6000 rpm for 40 s .

4. Check for uniformity of resist.

5. Bake on hot plate @ 180° C for 1 hr.

6. Clean a second pipette for application of the upper layer.

7. Spin on a drop of 950 K PMMA in the same fashion.

8. Check for uniformity of resist.

9. Bake on hot plate @ 180° C for 1 hr.

Immediately starting to spin on the resist is important in creating a uniform resist layer. Furthermore, anisole is a strong solvent for PMMA, and it is possible that the lower layer could be dissolved when PMMA for the upper layer is applied if spinning does not begin immediately.

3.1.2 Pattern Generation System

The pattern generation system we use consists of a LEO 440 scanning electron microscope (SEM), a Gateway microcomputer, and pattern generation software and hardware obtained from J. C. Nabity Lithography Systems.

The principle of the NPGS system is illustrated in Fig. 3.2. We first draw the desired pattern using a CAD program. Different doses and SEM settings (*e. g.* magnification and beam current) can be allowed for by assigning corresponding parts of the drawing different colors and layers, respectively. A run file is then created by running a program called MRF (make run file). During this step, the specific values of doses and SEM settings are given to the run file. To perform an exposure, NPGS uses a program called PG (pattern generation) to access the information stored in the run file. PG interfaces with the LEO 440 via two 16-bit digital-to-analog converters (DACs) for x and y control of the beam position within the field of view of the microscope and a third line to control the beam blanker. The beam blanker in our system is a pair of parallel plates. When a large enough voltage (normally 70 V) is applied across the plates, the electron beam is deflected and does not pass through the final aperture. The role of blanking the electron beam is two-fold: first, by controlling when the beam is blanked, we are controlling the exposure time and hence the dose received by the resist; second, the beam must be blanked when it is moved to another

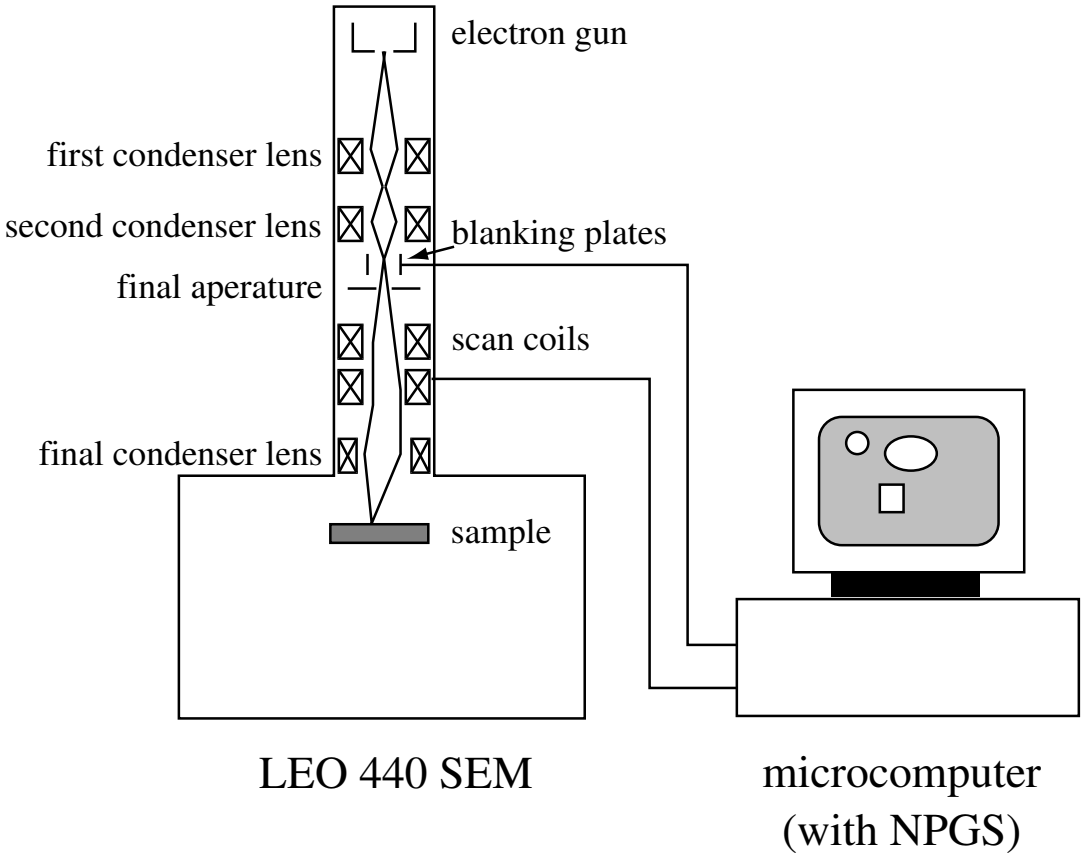

Figure 3.2: A conventional electron microscope converted to an e-beam writer. The microcomputer is equipped with a commercial package, the Nanometer Pattern Generation System (NPGS), which interprets CAD drawings on the microcomputer to perform an exposure via control of the scan coils and beam blanker of the SEM.

place of the sample, so that the path it follows will not be unintentionally exposed.

3.1.3 Sample Exposure

Sample exposure is a complex process. The major steps are as follows:

1. Ramp up the SEM to the desired voltage (35 kV in this case) and saturate the filament.
2. Adjust the settings of the SEM. This includes aligning the gun, aligning the final aperture, adjusting the astigmatism and focus of the beam, and setting the proper magnification and beam current.
3. Turn on the beam blanker. Move the sample to the desired position.
4. Run NPGS to draw the smallest features.
5. Change the final aperture for patterning of larger features if necessary.
6. Change the corresponding SEM parameters for larger features, such as magnification and probe current.
7. Run NPGS to draw the larger features.
8. Change the SEM settings back and return to the smallest aperture.
9. Turn down the filament and shut down SEM.

For the finest gates (with width $\approx$ 150 nm), small spot size is necessary and a small electron beam current (normally 10 pA) is used. A much larger current and a lower magnification are used to draw the larger leads and pads since patterning them does not require a very small spot size. The final aperture must be changed to a

larger one then since we do not want the large beam current to cause contamination of the smallest aperture used for patterning of the gates. For a typical sample, three different beam settings and apertures are used for features of different sizes.

After the pattern is drawn, the sample is removed from the SEM and is ready for development. We use a 3 to 1 mixture of isopropanol and MIBK (methyl-isobutylketone) as a developer. The sample is developed in this solvent at 23° C for 60 s, followed by rinsing in IPA for another 30 s. To prevent residue formation on the surface, the sample is immediately blown dry with an air gun and examined under an optical microscope. The optical microscope cannot resolve features with sizes $< 10\mu$m, but it will give us some idea if the larger features have been exposed successfully. If all appears well, it is time to proceed to evaporation and liftoff.

3.1.4 Evaporation

We use Au as the material to form the gates. Au is not superconducting, will not disturb magnet field lines if such a field is applied, and will not oxidize, which make it a popular metal for gate deposition. Au also gives off a strong secondary electron signal, making it easy to see in the SEM and simplifying the alignment process we will discuss later. One problem with Au is that it does not adhere well to GaAs surface. To solve this problem, a thin layer of Cr is usually deposited first. This combination is very widely used for depositing non-superconducting and non-magnetic patterns.

The metal deposition is performed in a CVC thermal evaporator, which has two evaporating sources. For our samples, the thickness of Cr film deposited is about 20 Å, and the thickness of Au deposited is about 200 Å. The sample is then taken out and put in ACE for liftoff. The last process usually takes about 4 hrs.

3.2 Fabrication of Al Junctions

3.2.1 Shadow Evaporation

Fabrication of Al junctions employs the same e-beam lithography techniques discussed above. This time, however, while the top layer is still 950 K PMMA, as for Au gates, the bottom layer is PMMA-MAA, which has a much higher electron sensitivity than 950 K PMMA. In addition, a relatively low accelerating voltage of 20 kV (compared to the 35 kV used for fabricating Au gates) is used so that backscattering of electrons is more prominent, resulting in a higher dose in the bottom layer. Due to these measures, a much larger undercut is formed in the bottom layer than in a usual bilayer resist system. In a carefully designed pattern, a suspended "bridge" can be created by exposing two regions separated by a small gap. A junction can then be fabricated by first evaporating Al from one angle, introducing O_2 to form a thin (a few angstrom) oxide on the Al surface, then evaporating a second layer of Al from a different angle so that a small overlap is formed between the two Al layers, as illustrated in Fig. 3.3. This technique is called "shadow evaporation," and is now a standard process used to produce ultra small Al/AlO_x junctions [52].

A liquid nitrogen trap is used in our evaporator which helps prevent diffusion pump oil from backstreaming into the sample chamber. Typically, a vacuum $\sim 5 \times 10^{-7}$ torr can be achieved after pumping for an hour. After the first evaporation, the oxidation is done by introducing a small amount of O_2/Ar mixture with 5% O_2. Normally, an oxidation for 3 min with 45 milibar of the mixture will gives a junction resistance of $\sim 50\,\mathrm{K}\Omega$. Although this is adjusted as necessary. The O_2/Ar mixture is then pumped out and the second evaporation is performed. Pump oil contamination, sometimes not obvious, can play an important role during oxidation of the Al junctions. Contrast to

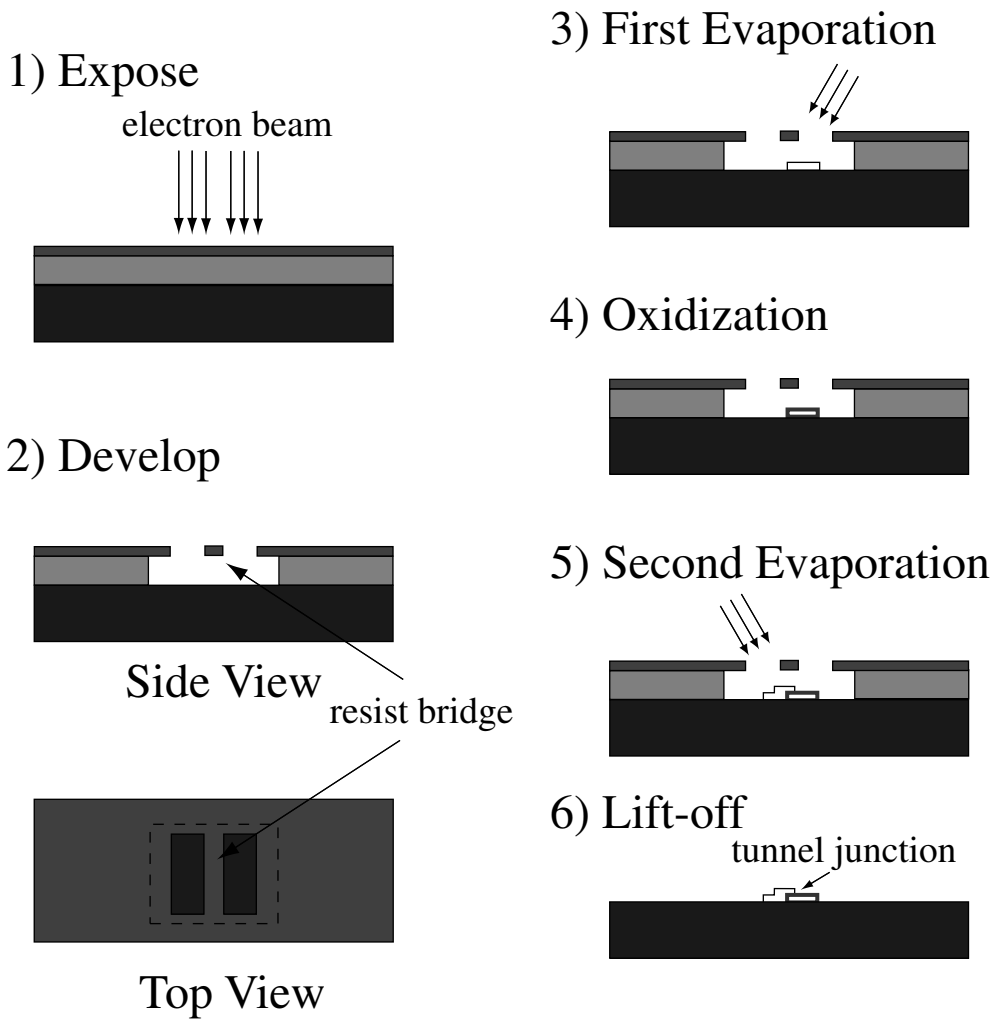

Figure 3.3: Major steps involved in fabricating Al/AlO_x junctions. A hanging resist bridge is formed during the e-beam lithography process. A shadow evaporation technique is then used to produce the junction, which is a thin oxide layer sandwiched by two layers of Al evaporated from different angles.

the more usual variations which still occur if everything is going well, contamination can cause vary large variations in the resistance of the junctions from one sample to the next, and also seems to make the junctions more vulnerable to static charge damage. For example, the junction resistance may vary from 20 KΩ to 60 KΩ even when everything is going well. However, it may vary from a few hundred Ohms to megohms if there is a contamination problem. Regular cleaning of the tubing to the gas cylinders and the O-ring seals of the sample tilting structure and the shutter is recommended.

3.2.2 Alignment

For reasons we will discuss later, the SET island needs to be fabricated at the center of the Au gates, so that an alignment accuracy of $\leq$ 30nm is needed. This turns out to be tricky. Since the sample has been removed from the SEM for deposition of the gates and resist preparation, physical alignment alone cannot achieve the required accuracy. In addition, imaging the sample while everything is in place is not practical because the beam will expose the resist while imaging. A special program in the NPGS package called "AL" (align) is used to solve this problem. Before AL can be used, a series of alignment marks are fabricated along with the Au gates on the sample, a safe distance away from the center. A corresponding series of windows containing overlays having the same shape as the alignment marks are also created in NPGS. By running AL, only the areas corresponding to the windows will be exposed. If everything is carefully designed, images of the regions containing the alignment marks will be captured. By adjusting the overlays to the corresponding alignment marks, AL will record information such as shifts in the pattern position, rotation and magnification, and create a matrix to compensate for these shifts. This process

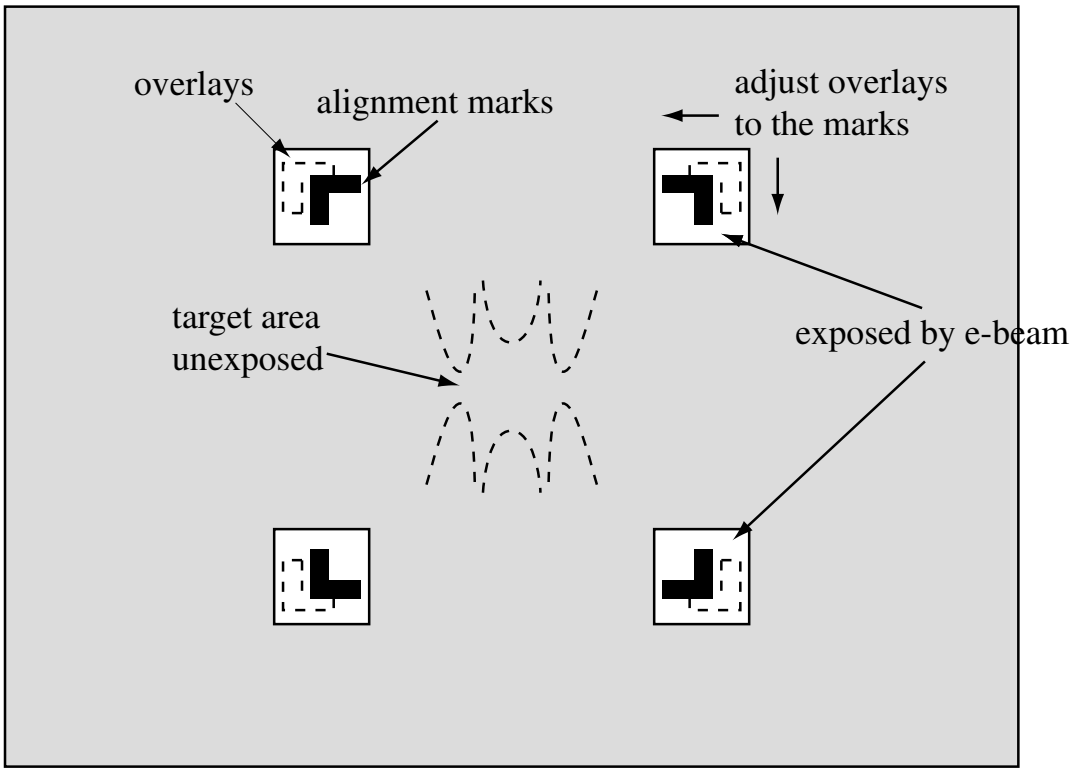

Figure 3.4: Schematic drawing of the alignment process. Only the areas in the windows are exposed in this process. Adjusting the overlays to the alignment marks allows NPGS to calculate translation and rotation matrices.

is illustrated in Fig. 3.4. NPGS then applies this matrix to the pattern drawing procedure so that the pattern is drawn in the correct position and orientation, and with the correct magnification.

3.3 Ohmic Contacts

Numerous recipes are available which will give ohmic contact to the electron gas in GaAs/$Al_xGa_{1-x}As$ heterostructures [53]. The one we use is one of the oldest and best-known techniques, namely alloyed indium.

The exact physical process by which In alloy makes a good ohmic contact is complicated and not well-understood. Possible explanations include that the formation of InAs by the alloyed In may have an electron affinity close to that of GaAs, or that a large number of surface states created in the alloying process may have pinned the Fermi level near the conduction band edge, giving a small barrier height for the InAs/GaAs interface.

Typical steps involved in making ohmic contacts include:

1. Cleave a 2 mm × 3 mm piece of material from the wafer.
2. Clean sample in ACE ultrasound for 20 min to remove dust created during the cleaving process, followed by rinsing in IPA and blow dry.
3. Prepare In on a clean microscope slide by melting In wire (Indium Corp, 99.99%, 0.02 in) using a soldering iron at 700° F.
4. Press In onto surface of sample using a soldering iron at 600° F.
5. Check "solder" points. It may be necessary to press some extra In down using tweezers.
6. Place sample into tape heater oven. Flush oven with forming gas (20% H_2, 80% He) for 10 min. to remove any air from the chamber.
7. Use a flow meter, set flow of forming gas to desired rate for baking, typically 70 ml/min.
8. Bake sample at 110° C for 1 min. to remove adsorbed water.
9. Ramp temperature to 400° C; hold at 400° C for 4 min.
10. Turn off heater. Leave forming gas flowing until sample is cool.

11. Test contacts at 4.2 K.

Baking time is the most important parameter. Since contact must be made to a very thin electron layer, either too short or too long a bake time will cause the contacts to fail. A failed contact will exhibit either an open circuit or a diode behavior. If the baking time turns out to be too short, rebaking the sample may help. A 4 min bake seems to work well for both the 50 nm and 190 nm deep 2DEG materials. Another trick is that if the contact area is too small to begin with, the contacts will not be very reliable.

The tape heater oven is a home-made $4 \times 4 \times 4$ in^3 clear plastic box with gas inlet and outlet ports, and a rubber gasket seal. Two high current (~ 20 A) Cu wire feedthroughs are attached to each end of a $1 \times 0.25 \times 0.015$ in^3 nichrome tape (80% Ni, 20% Cr), on which the sample is placed. The sample is heated by running a large dc current through the tape, the temperature of which is measured via a thermocouple spot welded to the underside of the tape. The baking is performed in a forming gas atmosphere, in which the H_2 acts as a reducing agent, minimizing oxidation of the In and the sample.

3.4 Chemical Etching

The 2DEG serves effectively as a ground plane capacitively coupled to the SET. For a typical SET design, the pad area is about 250 μm$\times$250 μm, which corresponds to a capacitance on the order of tens of picofarads to a 50 nm deep 2DEG. In the radio-frequency single-electron transistor experiments we will discuss later in this thesis, a capacitance to ground $C_s \leq 0.3$ pF is needed. In this case, 2DEG beneath the large pads and leads of the SET has to be etched away. This process is performed in our lab with chemical etching (wet etching).

In order to prevent the formation of the 2DEG, it is only necessary to destroy the δ dopant layer, or just etch close enough to the δ dopant layer so that all the donor electrons will be bonded to the surface states. For example, for the 200 nm deep 2DEG material, a 50 nm deep etch is proven to be sufficient.

Almost all GaAs etchants operate by first oxidizing the surface and then dissolving the oxide, thereby removing some of the gallium and arsenic atoms [53]. As for all chemical reactions, temperature plays an important role in the etch rate: an increase of 10° C will roughly double the etch rate. The etchant we use is made by first mixing citric acid with de-ionized (DI) water with a 1:1 ratio by weight. The solution is then mixed with hydrogen peroxide (H_2O_2) with a ratio of 30:1 by volume, in which hydrogen peroxide serves as the oxidizer and citric acid as the dissolving agent. This very dilute solution allows a slow etch rate about a few nanometers per second. The etch rate of such dilute etchant is typically limited by the rate of reaction and not sensitive to agitation, whereas the etch rate in a concentrated etchant is often limited by the rate the regent molecules reaching the surface or the reaction products leaving the surface and hence sensitive to the level of agitation. PMMA 495K resist turns out to be a good mask for this etchant. To increase adhesion between the resist and the GaAs surface, a thin layer of hexamethyldisilazane (HMDS) is used. In the area exposed to e-beam, HMDS is damaged together with the resist and dissolved in the development process. Since no liftoff is performed, pronounced undercut in resist profile is no longer necessary and only one layer of resist is used.

A potential concern of GaAs etching is the edge profile of the etched region. An outward slope profile is preferable and an undercut profile should be avoided for step coverage of the metallization. In general, the edge profile is related to the crystal structure of GaAs and can be controlled by selecting the orientation of the pattern and adjusting the ratio of the etchant. However, for a very shallow etch like ours, the

edge profile turns out to be always more or less vertical and the metal crossover is always continuous.

The condition of the substrate surface, on the other hand, plays an important role in this kind of shallow etch. In fact, for a total etch time of $\sim$ 55 seconds, it takes about 40 seconds or so only to etch away a very thin surface layer ($\sim$ 3 nm). After that, a more stable etch rate about 3 nm/s is achieved. The time it takes to etch away the surface layer depends on the type of substrate, the manufacturer of the wafer and more importantly, the cleanness of the sample. For example, if an e-beam lithography step has already been performed on the sample, some organic residue will be left which is difficult to remove completely even after a long lift-off. As a result, the subsequent etching tends to be hard to control. Further more, baking the sample at high temperatures seems to "harden" the surface and makes etching difficult as well. For example, after the sample is baked at 400° C to form the Ohmic contacts to the 2DEG, we have never been able to etch through the surface layer using the dilute etchant. To circumvent these issues, etching is always performed as the first procedure in our sample fabrication.

The etched area also needs to be aligned with the Au and Al leads. This time, however, a resolution on the order of micrometers is sufficient, which can be achieved mechanically by the precision stage in the LEO SEM. Before etching, two scratch marks are put on the opposite corners of the sample chip, by imaging the marks at a magnification $\sim$ 10000, distinct features on the marks are selected and positions are saved with micrometer accuracy. The center of the chip is then calculated by calculating the average of the two saved positions and e-beam exposure is performed. Before the Au or Al exposure, the same features are located again on the SEM, and the center is calculated accordingly.

The procedure is summarized as following:

1. Put scratch marks near two opposite corners of the sample. Clean sample in acetone (ACE) ultrasound as usual.
2. Apply a drop of HMDS on the sample. Immediately start the spinner; spin @ 4000 rpm for 30 s. No baking is required in this step.
3. Apply a drop of PMMA 495 K. Spin @ 3000 rpm for 30 s.
4. Bake on hot plate @ 180° C for 1 hr.
5. Perform e-beam lithography.
6. Develop sample in HIBK/IPA as usual.
7. Mix 15 ml CA/H_2O and 0.5 ml H_2O_2 together in a beaker to form the etchant. While holding the beaker by hand, stir the etchant with a thermal couple probe, temperature controlling the etchant to 24.5° C.
8. Etch for 55 s while gently agitating the sample.
9. Rinse the sample in DI water for another 30 s. Blow dry.
10. Liftoff in ACE. Normally 1 hour is sufficient.

3.5 Refrigeration

3.5.1 Principles

All the measurements we discuss in this thesis are performed in an Oxford Instruments Model 100 dilution refrigerator, which has a base temperature of 20 mK and is equipped with a 10 Tesla magnet. A good review of the principles of dilution

refrigerator can be found in the Oxford manual and Richardson and Smith [56]. Here we give a very brief description of its operation.

In normal evaporative cooling, atoms are removed from the liquid together with latent heat. However, as temperature drops, so does the vapor pressure. Eventually the system will reach a point where the vapor pressure is so low that not enough atoms can be pumped out to keep cooling the system down. This limits the achievable temperature to ~ 1 K if using ^{4}He and ~ 0.3 K if using ^{3}He. A dilution fridge works with a different mechanism. If we cool any ^{3}He/^{4}He mixture with more than 6% ^{3}He concentration to a low enough temperature, the mixture will separate into two phases. One of the phases will be almost pure ^{3}He (the "concentrated" phase). The other one will be primarily ^{4}He, but will still have 6% ^{3}He concentration even as the temperature approaches absolute zero (the "dilute" phase). However, since the vapor pressure of ^{3}He is much higher than that of ^{4}He (roughly 1000:1), the equilibrium vapor of the dilute phase is also almost pure ^{3}He. These unique properties of ^{3}He/^{4}He mixtures provide a means of cooling samples to very low temperatures.

Fig. 3.5 shows the separation of the two phases. Pumping on the ^{3}He dilute phase results primarily in removing ^{3}He from the liquid. The equilibrium of the two phases is then broken and ^{3}He atoms in the ^{3}He concentrated phase will diffuse across the phase boundary to the ^{3}He dilute phase. Latent heat will be absorbed in this process, and samples thermally anchored to the mixture will be cooled down. In practice, the initial cooling is achieved by simple evaporative cooling of the mixture. Phase separation occurs when the mixture temperature reaches 0.86 K in a chamber called "mixing chamber". Evaporation of ^{3}He is performed at a different chamber (the "still") at a temperature of 0.6 K–0.7 K where vapor pressure can reach up to 1 milibar, even though the temperature at the mixing chamber where cooling takes place can reach as low as 0.005 K. The separation of pumping and cooling is the key

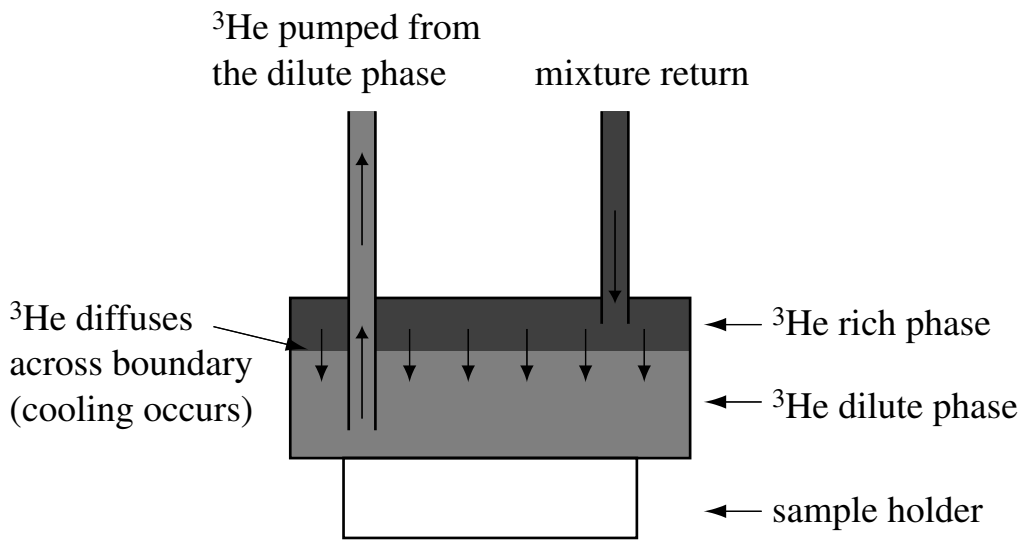

Figure 3.5: ^{3}He/^{4}He mixture separates into two phases at low temperatures. Pumping on the ^{3}He dilute phase causes ^{3}He to diffuse across the phase boundary, thereby cooling the sample.

in ensuring the continuous cooling of a dilution fridge into the milikelvin range, where various thermal leaks finally set the limit.

To reduce heat leaks to the fridge, in our system, the fridge (called "the insert") works inside a vacuum chamber (the "inner vacuum chamber", IVC), which is in turn immersed in a ^{4}He bath. The mixing chamber part is further protected by a Cu shield to reduce heat leak via radiation from the ^{4}He environment. The ^{4}He bath is stored in a chamber with vacuumed walls (the "outer vacuum chamber", OVC), which also has many layers of radiation shield (the "super-insulation") to prevent heat leak via radiation. Furthermore, the OVC is surrounded by a liquid nitrogen jacket, so that radiation from room temperature will mostly be obsorbed by the LN2 jacket, and radiation to the OVC is mainly from a much lower temperature (77 K).

3.5.2 Heat Sinks

In our system, 24 wires and two 0.085" semi-rigid co-axial cables run from room temperature down to the sample. They, especially the cables which carry signal at high frequencies, need to have a good electrical conductance to reduce signal loss. On the other hand, they should not have a large thermal conductance to reduce heat leak through them. Since a good electrical conductor is normally also a good thermal conductor (except for superconductors), a comprise must be made. The wires we use are 0.005" Manganin 290, type H-ML fabricated by California Fine Wire Co. The co-axial cables from room temperature down to the IVC part (at $T \approx 4\,\mathrm{K}$) have both a stainless-steel (SS) outer conductor and a stainless-steel inner conductor, and is pre-installed by Oxford. The cables from the IVC down to the sample chamber have a copper clad SS outer conductor and a silver-plated berillium-copper (BeCu) inner conductor (Precision Tube Co, model JN50085) as a comprise for both a satisfactory electrical conductance and thermal conductance.

The wires and cables must also be thermalized at various temperatures to minimize the heat load at the mixing chamber. To heat sink the wires, we anchor 0.3" OD, 1" long copper bobbins at various stages of the fridge, and wrap the wires around the bobbins multiple times. Low temperature GE varnish is painted on the wires in the end to improve thermal contact.

Heat sinking of the cables is trickier and can only be done to the shield of the cables. A length of 20 gauge magnet (Cu) wire is wrapped alternatively around the cable and the bobbins at various stages of the fridge. Normally, at least 20 turns should be made at each stage. The lower the temperature, the more turns are needed. Once again, GE varnish is used in the end to improve thermal contact. This technique seems effective in our system and the performance of the fridge does not seem to have

deteriorated after installation of the cables.

The sample is mounted on a home-made "tail" screwed into the mixing chamber. Sample heat dissipation must also be carefully considered, *i. e.* the mixing chamber reading is not necessarily the same as the sample temperature. Heat generated in the sample by electrical measurements can be dissipated both through the on-chip leads and through the substrate. Calculations show that in systems like ours, the heat is mostly dissipated through the on-chip leads. Several more heat sinks are screwed on the tail to help thermally anchor these wires. The tail must be carefully designed to ensure there is no large temperature difference between the mixing chamber and the end of the tail where the sample is mounted. The tail is also carefully designed to minimize eddy current heating when the magnet is in use.

3.5.3 Sample Wiring and Filtering

The Manganin wires terminate on a set of PC boards where fine copper wires are then used to connect them to the sample pads. Normally, the sample is tested on a test box first. The connection to the sample pads is made by a "sandwich technique." An indium dot (a slice of indium wire) is first placed on the on-chip pad. After laying a piece of fine Cu wire on top of the indium dot, another indium dot is placed on top and pressed down using tweezers. To make good low resistance contacts, the surfaces of the pad and the indium dot must be very clean. The first condition is satisfied by making the connection right after liftoff, while the second is satisfied by using the freshly cut surface of the indium slice.

Electrostatic discharge can cause serious problems during wiring and sample handling. A very small discharge can easily destroy the sample by either burning out the fuse-like leads or punching holes in the thin oxide layer. Numerous measures are

taken to reduce the chances of static charge damage. These include:

- Ground all wires before connecting them to the sample.
- Use grounding straps and pads.
- Use ionizing (antistatic) fans (Ion Systems, Z-Stat 6441) and blowers (Simco, AFC-2, PG-5) to neutralize static charges accumulated on the surfaces.
- Use static-safe tweezers.

The fans turn out to be critical, since charge accumulation on the semi-insulating surface of the sample will not be dissipated easily by other means. When the sample is to be moved around, for example, from the test box to the tail, the wires directly connected to the on-chip pads must be disconnected first and reconnected later following the same procedure. The wires then need to be grounded at all times until the measurement is performed.

High frequency noise is a significant concern in these low-temperature, small-signal measurements. Radio frequency or microwave noise can easily heat the sample or contaminate the results of the measurements. To deal with this problem, the sample is mounted inside a metallic enclosure which is carefully sealed with conductive tape. This measure is intended to block any microwave black body radiation present inside the insert. The fridge itself serves as a shield for radiations from room temperature. Furthermore, all the measurements are performed inside an rf shielded room with an attenuation of more than 100 dB at 1 GHz, and battery powered electronics are used to avoid noise associated with the electrical mains.

To reduce magnetic pickup, the 24 wires are grouped into 6 twisted quads. The wires must also be carefully filtered to prevent high frequency noise going along them to the sample. In our set-up, each wire is filtered by a "T" filter (Murata Electronics,

Inc.) at room temperature and RC and Cu powder microwave filters [57] at mixing chamber temperature. Recently, a new type of microwave filter was suggested by Schoelkopf at Yale University, consisting of a length of the Manganin twisted quads (1.5 m to 2 m) sandwiched between two pieces of Cu tape. The idea is that the wire/tape system behaves like a lossy transmission line, and attenuation exceeding 70 dB has been measured in our new filters around 1 GHz.

CHAPTER 4

VERIFICATION OF THE ENVIRONMENTAL THEORY

4.1 Charge Tunneling Rates and Effects of The Environment

In Chapter 2, we gave a qualitative description of the behavior of the single-electron transistor. To understand its behavior quantitatively, a more detailed analysis is needed. In this section, following the discussion in Grabert and Devoret [17], we use the golden rule approach to calculate charge tunneling rates in ultra small junctions, especially emphasizing the effects of the environment. $I(V)$ curves of a single-electron transistor will later be derived from the detailed balance equation.

4.1.1 Single Junction In Normal State

The box-like junction symbol in Fig. 2.1 emphasizes the two important properties of an ultra small tunnel junction: a) it has a capacitance C. b) charges can tunnel through it. To calculate the tunneling rate of the junction, we start by looking at its Hamiltonian. In the normal state, the Hamiltonian should first include a term describing the states of quasiparticles in the two metal electrodes

$$\tilde{H}_{qp} = \sum_{k\sigma} \epsilon_k c^{\dagger}_{k\sigma} c_{k\sigma} + \sum_{q\sigma} \epsilon_q c^{\dagger}_{q\sigma} c_{q\sigma} \tag{4.1}$$

where the first and second sum correspond to the left and right electrode, respectively. ϵ_k and ϵ_q are the energies of quasiparticles with wave vector k and q while σ denotes their spin. $c^\dagger$ and c are electron creation and annihilation operators.

Tunneling will mix states in the two electrodes together, and can be described by the Hamiltonian

$$H_T = \sum_{kq\sigma} T_{kq} c^\dagger_{q\sigma} c_{k\sigma} e^{-i\varphi} + \text{H.c.} \tag{4.2}$$

where T_{kq} represents the tunneling matrix element. The phase

$$\varphi(t) = \frac{e}{\hbar} \int_{-\infty}^{t} dt' U(t')$$

is necessary to account for the fact that a tunneling event changes the charge on the junction by an elementary charge e, where $U = Q/C$ is the voltage across the junction.

It can be proven that φ and Q are conjugate variables and they satisfy the commutation relation.

$$[\varphi, Q] = ie$$

It is more convenient to consider the variables

$$\tilde{\varphi}(t) = \varphi(t) - \frac{e}{\hbar} V t$$

and

$$\tilde{Q} = Q - CV$$

describing the fluctuations around the mean value determined by the external voltage. After a time-dependent unitary transformation, Eq. 4.1 and Eq. 4.2 now become

$$\tilde{H}_{qp} = \sum_{k\sigma} (\epsilon_k + eV) c^\dagger_{k\sigma} c_{k\sigma} + \sum_{q\sigma} \epsilon_q c^\dagger_{q\sigma} c_{q\sigma} \tag{4.3}$$

$$\tilde{H}_T = \sum_{kq\sigma} T_{kq} c^\dagger_{q\sigma} c_{k\sigma} e^{-i\tilde{\varphi}} + \text{H.c.} \tag{4.4}$$

Finally, there is the Hamiltonian of the environment to which the junction is coupled. In the approach introduced by Caldeira and Leggett [12], the environment is modeled by a set of LC harmonic oscillators and its Hamiltonian can be written as

$$H_{\text{env}} = \frac{\tilde{Q}^2}{2C} + \sum_{n=1}^{N} [\frac{q_n^2}{2C_n} + (\frac{\hbar}{e})^2 \frac{1}{2L_n} (\tilde{\varphi} - \varphi_n)^2] \tag{4.5}$$

The first term describes the charging energy of the junction capacitor C. In the second term we sum over the environmental degrees of freedom represented by harmonic oscillators of frequency $\omega_n = 1/\sqrt{L_n C_n}$ which are bilinearly coupled to the phase of the tunnel junction. In order to describe an effectively dissipative environment the number N of the environmental degrees of freedom has to be rather large. Usually, in practice the limit $N \to \infty$ has to be performed.

The total Hamiltonian is now described as

$$H = \tilde{H}_{qp} + H_{\text{env}} + \tilde{H}_T \tag{4.6}$$

which we will use to calculate the tunneling rates.

In the following, we assume two conditions are satisfied. First, the tunneling resistance R_T is large compared to the resistance quantum $R_K = h/e^2$. Second, charge equilibrium is established before a tunneling event occurs. The first requirement implies that the quasiparticle states are only weakly mixed and perturbation theory can be used. The second requirement further implies that equilibrium states can be used in the perturbation theory. Under these limits, we consider the tunneling Hamiltonian $\tilde{H}_T$ as a perturbation and use the golden rule to calculate tunneling rates in leading order

$$\Gamma_{i \to f} = \frac{2\pi}{\hbar} |\langle f | \tilde{H}_T | i \rangle|^2 \delta(E_i - E_f) \tag{4.7}$$

which gives the rate for transitions between the initial state $|i\rangle$ and the final state $|f\rangle$.

We further break the states $|i\rangle$ and $|j\rangle$ into $|i\rangle = |E\rangle|R\rangle$ and $|j\rangle = |E'\rangle|R'\rangle$, where $|E\rangle$ and $|E'\rangle$ are quasiparticle states of energy E and E', respectively, and $|R\rangle$ and $|R'\rangle$ are reservoir states which are connected with the coupling to the environment. The tunneling rate should be calculated over the integration of all possible $|E\rangle$ and $|E'\rangle$. After some math, we finally get the forward tunneling rate through the junction

$$\begin{aligned}\vec{\Gamma}(V) &= \frac{1}{e^2 R_T}\int_{-\infty}^{+\infty} dE dE' f(E)[1-f(E')] \\ &\quad \times \sum_{R,R'} |\langle R|e^{-i\tilde{\varphi}}|R'\rangle|^2 P_\beta(R)\delta(E+eV+E_R-E'-E'_R) \end{aligned} \tag{4.8}$$

where R_T turns out to be an effective tunneling resistance and $P_\beta(R)$ is the probability of finding the initial reservoir state $|R\rangle$ at inverse temperature $\beta = 1/k_B T$.

After summing over reservoir states $|R\rangle$ and $|R'\rangle$, Eq. 4.8 can be further simplified by introducing a correlation function

$$K(t) = \langle[\tilde{\varphi}(t) - \tilde{\varphi}(0)]\tilde{\varphi}(0)\rangle \tag{4.9}$$

which inherited the effects of the environment H_{env}, and its Fourier transform

$$P(E) = \frac{1}{2\pi\hbar}\int_{-\infty}^{+\infty} dt \exp[K(t) + \frac{i}{\hbar}Et] \tag{4.10}$$

The tunneling rate is then

$$\vec{\Gamma}(V) = \frac{1}{e^2 R_T}\int_{-\infty}^{+\infty} dE \frac{E}{1-\exp(-\beta E)} P(eV-E) \tag{4.11}$$

Eq. 4.11 will be used to calculate tunneling rates from now on.

4.1.2 $P(E)$ Function

The $P(E)$ function in Eq. 4.11 has a straightforward physical interpretation. It represents the probability the tunneling electron will exchange energy E with the

environment while tunneling. This interpretation can be further confirmed by the following properties of $P(E)$

$$\int_{-\infty}^{+\infty} dE P(E) = 1$$

$$\int_{-\infty}^{+\infty} dE E P(E) = E_c \equiv e^2/2C$$

and the detailed balance symmetry

$$P(-E) = e^{-\beta E} P(E).$$

The last equation agrees with the fact that the probability to emit energy E to the environment is larger than that of absorbing energy E from the environment by a Boltzmann factor.

In practice, $P(E)$ is calculated from $K(t)$ from Eq. 4.10, where $K(t)$ in turn is related to the real part of the total impedance seen by the junction $\mathrm{Re}[Z_t(\omega)]$:

$$K(t) = R_K^{-1} \int_{-\infty}^{\infty} \frac{d\omega}{\omega} \mathrm{Re}[Z_t(\omega)] \times \{\coth(\frac{1}{2}\beta\hbar\omega)[\cos(\omega t) - 1] - i \sin(\omega t)\}. \qquad (4.12)$$

Once we know the tunneling rate from Eq. 4.11, the $I(V)$ characteristics of the junction can be easily obtained by subtracting the reverse tunneling from forward tunneling

$$I(V) = e(\vec{\Gamma}\ (V) - \overleftarrow{\Gamma}\ (V))$$

to be

$$I(V) = \frac{1}{eR_T}(1 - e^{-\beta eV}) \int_{-\infty}^{+\infty} dE \frac{E}{1 - e^{-\beta E}} P(eV - E). \qquad (4.13)$$

In the zero temperature limit, Eq. 4.13 can be rewritten as

$$I(V) = \frac{1}{eR_T} \int_0^{eV} dE (eV - E) P(E) \qquad (4.14)$$

since no energy can be absorbed from the environment and the tunneling electron has a maximum energy eV to give to the environment. $P(E)$ is now directly related

to the second derivative of $I(V)$

$$\frac{\mathrm{d}^2 I}{\mathrm{d}V^2} = \frac{e}{R_T} P(eV). \tag{4.15}$$

From Eq. 4.10–4.15 it is clear that $P(E)$ serves as a bridge between tunneling properties of the junction and the environment the junction couples to, more specifically, the real part of the impedance of the environment $\mathrm{Re}[Z_t(\omega)]$ up to a frequency of $eV/\hbar$ (one electronvolt corresponds roughly to 242 THz). By studying tunneling properties of the junction, high frequency properties of the environment can thus be obtained.

Some important limiting behaviors of $P(E)$:

- For a low impedance environment, $P(E) = \delta(E)$, *i. e.*, in the absence of environmental modes only elastic tunneling processes are possible.

- For a high impedance environment,

  $$P(E) = \frac{1}{\sqrt{4\pi E_C k_B T}} \exp[-\frac{(E - E_C)^2}{4E_C k_B T}]$$

  and is centered around E_C. For very low temperatures $k_B T \ll E_C$, in the high impedance limit

  $$P(E) = \delta(E - E_C)$$

4.1.3 Single Junction In Superconducting State

For Josephson junctions, there are two kinds of charge carriers, namely Cooper pairs and quasiparticles. Two additional energy scales come into play besides E_C and $k_B T$, namely the Joesphson coupling energy E_J and the superconducting gap Δ. Once again, the charge Q and the phase φ are conjugate variables. In the regime $E_C \gg E_J$, charge is well defined and the phase fluctuations are large; while in the

opposite regime $E_C \ll E_J$ the phase fluctuates only a little and becomes the well defined variable. In the following, we concentrate in the regime of well-defined charge.

We further restrict ourselves to the limit in which the temperature is low compared to the critical temperature and voltage below the gap voltage $2\Delta/e$. In this limit, quasiparticle excitations can be neglected and only Cooper pair tunneling need to be considered.

In contrast to the quasiparticles we discussed in the earlier section, Cooper pairs form a condensate and do not lead to additional degrees of freedom. As a result, there is no counterpart of H_{qp} in the total Hamiltonian of Josephson junctions. The counterpart of the tunneling Hamiltonian H_T is now just the Josephson energy across the junction. The total Hamiltonian can then be written as

$$H = H_{\text{env}} + E_J \cos(2\varphi), \tag{4.16}$$

where the definition of H_{env} is the same as in Eq. 4.5. After writing the Joesphson term as

$$E_J \cos(2\varphi) = \frac{E_J}{2} e^{-2i\varphi} + \text{H.c.} \tag{4.17}$$

The analogy between Eq. 4.16 and Eq. 4.6 is obvious. In the limit $E_J P(2eV) \ll 1$, we can again treat the E_J term as a perturbation. Following the methods in Sec. 4.1.1 and Sec. 4.1.2, we can define

$$K(t) = R_Q^{-1} \int_{-\infty}^{\infty} \frac{d\omega}{\omega} \text{Re}[Z_t(\omega)] \times \{\coth(\frac{1}{2}\beta\hbar\omega)[\cos(\omega t) - 1] - i \sin(\omega t)\}. \tag{4.18}$$

and

$$P(E) = \frac{1}{2\pi\hbar} \int_{-\infty}^{+\infty} dt \exp[K(t) + \frac{i}{\hbar} E t] \tag{4.19}$$

Once again, $P(E)$ has the physical interpretation as the probability of exchange energy E with the environment. The only difference here is that $R_K \equiv \hbar/e^2$ in

Eq. 4.12 has been replaced by $R_Q \equiv \hbar/4e^2$ in Eq. 4.18, to take into account that a Cooper pair carries twice the electron charge.

Following the Golden rule approach in Sec. 4.1.1, we readily get

$$\vec{\Gamma}\,(V) = \frac{\pi}{2\hbar} E_J^2 P(2eV). \tag{4.20}$$

No integration over E is performed in Eq. 4.20 compared with Eq. 4.11. This is due to the fact that Cooper pairs form a condensate and no "individual" state is considered. It also agrees with the fact that the total energy $2eV$, rather than a part of it, has to be transferred to the environment, since the Cooper pairs, unlike quasipartles, have no kinetic energy to absorb a part of the energy.

The current through the junction is now

$$I(V) = \frac{\pi e E_J^2}{\hbar}(P(2eV) - P(-2eV)) \tag{4.21}$$

Unlike the normal junction case where $P(E)$ is proportional to the second derivative of $I(V)$, for a Joesphson junction the current through the junction is related to $P(E)$ in a more direct fashion. This property makes Joesphson junctions better suited for studying properties of the environment.

From Eq. 4.21, one can predict that there is a peak in the current as a function of voltage. The height and position of the current peak depend on $\mathrm{Re}[Z_t(\omega)]$. At very low bias, the I-V curve is more or less linear, and the current decreases with increasing $\mathrm{Re}[Z_t(\omega)]$. However, at biases larger than the peak voltage, the current decreases with increasing voltage, and increases with $\mathrm{Re}[Z_t(\omega)]$ [85].

Finally, the quasiparticle tunneling rate in a Josephson junction can be treated just as in the normal junction case. However, in the normal junction case, we have assumed that the density of states at the Fermi surface is constant, while in the

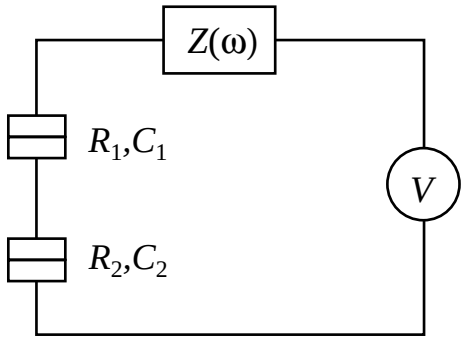

Figure 4.1: Schematic illustration of a double junction system coupled to a voltage source V via an external impedance $Z(\omega)$.

Josephson junction case, following the BCS-theory

$$\frac{N_S(E)}{N(0)} = \begin{cases} \frac{|E|}{(E^2-\Delta^2)^{1/2}} & \text{for } |E| > \Delta \\ 0 & \text{for } |E| < \Delta \end{cases} \tag{4.22}$$

where $N_S(E)$ is the reduced quasiparticle density of states and $N(0)$ is the density of states in the normal metal at an energy in the middle of the superconducting gap.

Following Sec. 4.1.1, we readily get

$$I_{qp} = \frac{1}{eR_T}\int_{-\infty}^{+\infty} dEdE' \frac{N_S(E')N_S(E'+E)}{N(0)^2}\frac{1-e^{-\beta eV}}{1-e^{-\beta E}} \times P(eV-E)[f(E')-f(E'+E)] \tag{4.23}$$

One important inference from Eq. 4.23 is that at finite temperature, the quasiparticle current always increases as $\mathrm{Re}[Z_t(\omega)]$ increases, in contrary to the Cooper pair behavior at very low biases.

4.1.4 Double Junction System

A typical double junction system is illustrated in Fig. 4.1 In the limit where tunneling through both both junctions is uncorrelated, from an individual junction's

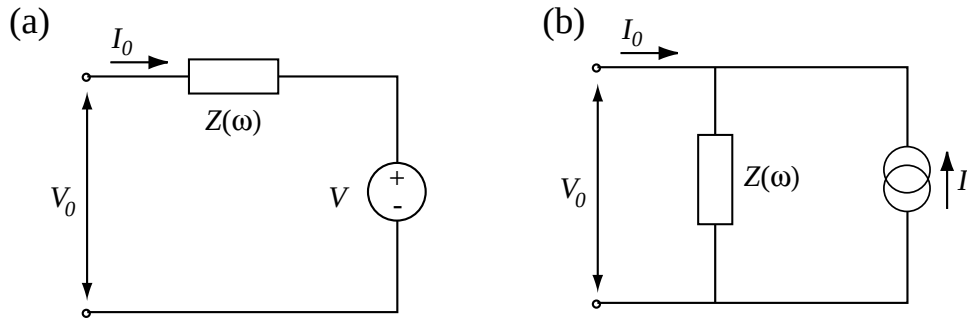

Figure 4.2: (a) Thevenin configuration: A voltage source V in series with the impedance $Z(\omega)$. (b) The equivalent Norton Configuration: A current source $I(\omega) = V(\omega)/Z(\omega)$ in parallel with the impedance $Z(\omega)$.

point of view, the other junction can then be simply treated as a capacitor. In order to calculate the tunneling rates from it, we only need to know the real part of the effective impedance sensed by the junction, $\mathrm{Re}[Z_t(\omega)]$.

The basic rule is the transformation between the Thevenin and Norton configurations shown in Fig. 4.2. The two configurations form two-terminal devices through which a current $I_0(\omega)$ flows if a voltage $V_0(\omega)$ is applied. From the outside the two configurations appear as equivalent if the same voltage V_0 leads to the same current I_0. In the Thevenin configuration the voltage drop is given by $V_0(\omega) = I_0(\omega)Z(\omega)+V(\omega)$, while in the Norton configuration the current is given by $I_0(\omega) = -I(\omega)+V_0(\omega)/Z(\omega)$. These two equations lead to the relation $V(\omega) = Z(\omega)I(\omega)$ between the voltage and current sources in the two configurations.

In Fig. 4.3, after a couple of transformations between the Thevenin and Norton configurations, we eventually reach to the Thevenin configuration in Fig. 4.3(c) for a double junction system. The effective voltage is now $\kappa_1 V$ where

$$\kappa_1 = 1 - C_1/(C_1 + C_2) \tag{4.24}$$

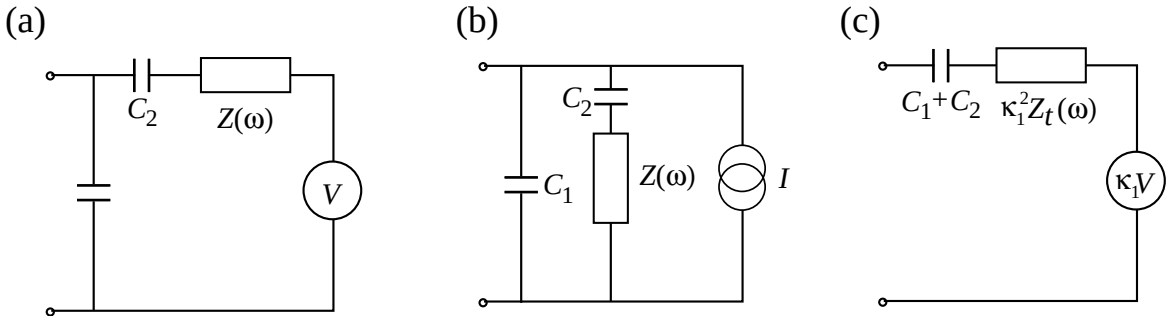

Figure 4.3: Transformation of a double junction circuit into an equivalent effective circuit. (a) Original circuit as seen from the first junction. The second junction is treated as a capacitor. (b) Equivalent Norton configuration. (c) Effective circuit for tunneling through the first junction.

which agrees with the fact that only a portion of the voltage V provided by the voltage source is applied across junction one. The effective impedance sensed by the junction is also reduced by κ_1 to be $\kappa_1^2 Z_t$ where

$$Z_t = \frac{1}{i\omega C} + Z^{-1}(\omega). \tag{4.25}$$

We can then apply the results obtained earlier for individual junctions and calculate $P(E)$ hence the tunneling rates for the double-junction system.

The energy difference for elastic tunneling of an electron through the j-th junction ($j = 1, 2$) on the the island is given by

$$\begin{aligned} \delta E_j(V, q) \equiv E_i - E_f &= \kappa_j eV + \frac{q^2}{2C_\Sigma} - \frac{(q-e)^2}{2C_\Sigma} \\ &= \kappa_j eV + \frac{e(q - e/2)}{C_\Sigma} \end{aligned} \tag{4.26}$$

where C_Σ is the total capacitance, and $C_\Sigma = C_1 + C_2, q = ne$ for a double junction and $C_\Sigma = C_1 + C_2 + C_g, q = ne + c_g V_g$ for an SET. The tunneling rate Γ can then be calculated from Eq. 4.11 or Eq. 4.20.

The current through the double junction system is

$$I = e \sum_{n=-\infty}^{+\infty} p_n(\vec{\Gamma}_1\,(n) - \overleftarrow{\Gamma}_1\,(n)) = e \sum_{n=-\infty}^{+\infty} p_n(\vec{\Gamma}_2\,(n) - \overleftarrow{\Gamma}_2\,(n)) \tag{4.27}$$

where p_n is the probability to find the double junction with a net charge of n electrons on the island, and the sum is over all possible states.

4.2 Model System

4.2.1 Introduction

From the pervious sections, we see that the electromagnetic environment plays an important role on electric transport in mesoscopic systems. The effects of the environment have been a subject of extensive theoretical and experimental interest in recent years. The reasons for interest are varied, as are the systems for which studies of the effects of the environment have been performed. Recent interest in quantum computation [64–67] has prompted interest in the effects of dissipation on decoherence rates in superconducting qubits [68, 69]. Double quantum dots have been used to study the effects of the environment on inelastic tunneling rates [16], and have been proposed as detectors of high-frequency noise produced by mesoscopic devices [70]. Finally, interest in quantum phase transitions [71] has prompted study of the effects of dissipation on superconducting systems such as thin films [72, 73] and Josephson junction arrays [22].

The $P(E)$ function is used in the theories to predict behavior of the mesoscopic systems studied. However, to date, $P(E)$ thoery has not been systematically tested experimentally. To do so, a well defined and tunable environment is a necessity. Unless great care is taken, in most experiments to date, the environment sensed by the junctions is dominated by macroscopic leads coupling the junctions to the room tem-

perature measurement electronics. The leads can be modeled as transmission lines, with some distributed resistance, inductance and capacitance per unit length [50, 51], and they typically present a low impedance to the junctions at microwave frequencies, limited by the impedance of free space (337 Ω).

In order to address this problem, the environment has to be tuned locally. A two-dimensional electron gas (2DEG), which can be formed in a layer in close proximity to the SET and whose properties can be varied by lighographically defined gates, becomes a natural choice. In our model system [74, 75], a superconducting SET (S-SET) is capacitively coupled and closely adjacent to a layer of 2DEG in the substrate about 50nm below the surface [77], as illustrated in Fig. 4.7. The coupling capacitance between the island of the SET and the 2DEG C_{2D} is comparable to the SET junction capacitances, which ensures that variations in the 2DEG will have a strong effect on properties of the SET.

4.2.2 Sample Design

Fig. 4.4 gives a schematic illustration of the sample design at a large scale. The central part of the sample is illustrated in Fig. 4.5, in both top and cross sectional views.

The sample fabrication procedures are:

1. Alloying Ohmic contacts to the 2DEG.

2. Fabrication of the Au gates and leads, together with a set of alignment marks. These alignment marks will be used to align the SET to the Au gates.

3. Alignment and exposure of the SET pattern.

4. Performing shadow evaporation.

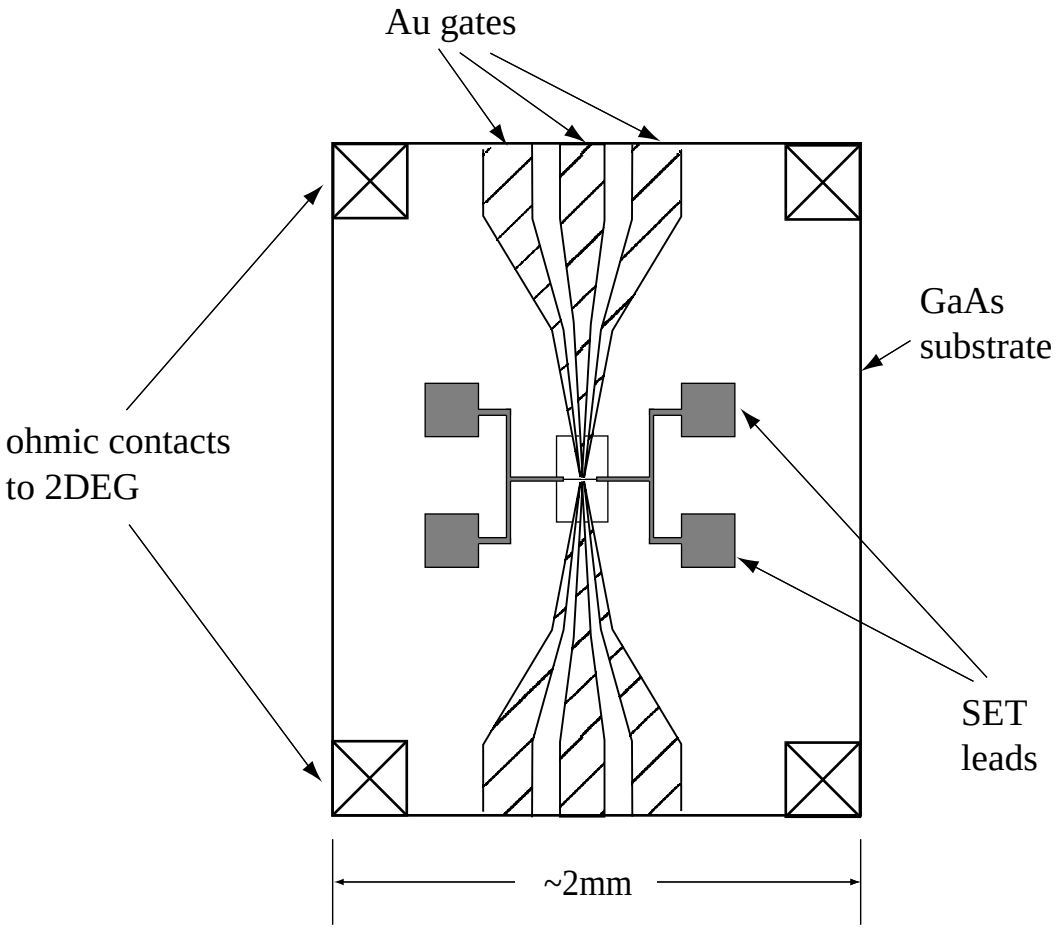

Figure 4.4: Schematic illustration of the sample, showing the ohmic contacts, Au gates and macroscopic pads for making contact to the SET.

The initial alignment in all these steps is performed by the "scratch mark" technique.

The substrate material we use is provided by Dr. Art Gossard's group at UC Santa Barbara. It contains a GaAs/$Al_xGa_{1-x}As$ heterostructure grown on a GaAs substrate using molecular beam epitaxy, consisting of the following layers: 1000 nm of GaAs, 47 nm of $Al_{0.3}Ga_{0.7}As$ and 5 nm of GaAs. The $Al_{0.3}Ga_{0.7}As$ is delta-doped with Si 22 nm from the lower GaAs/$Al_{0.3}Ga_{0.7}As$ interface, at which forms a two-dimensional electron gas (2DEG) with $R_{sq} = 20\,\Omega$ and sheet density $n_s = 3.6 \times 10^{11}\ \mathrm{cm}^{-2}$. After

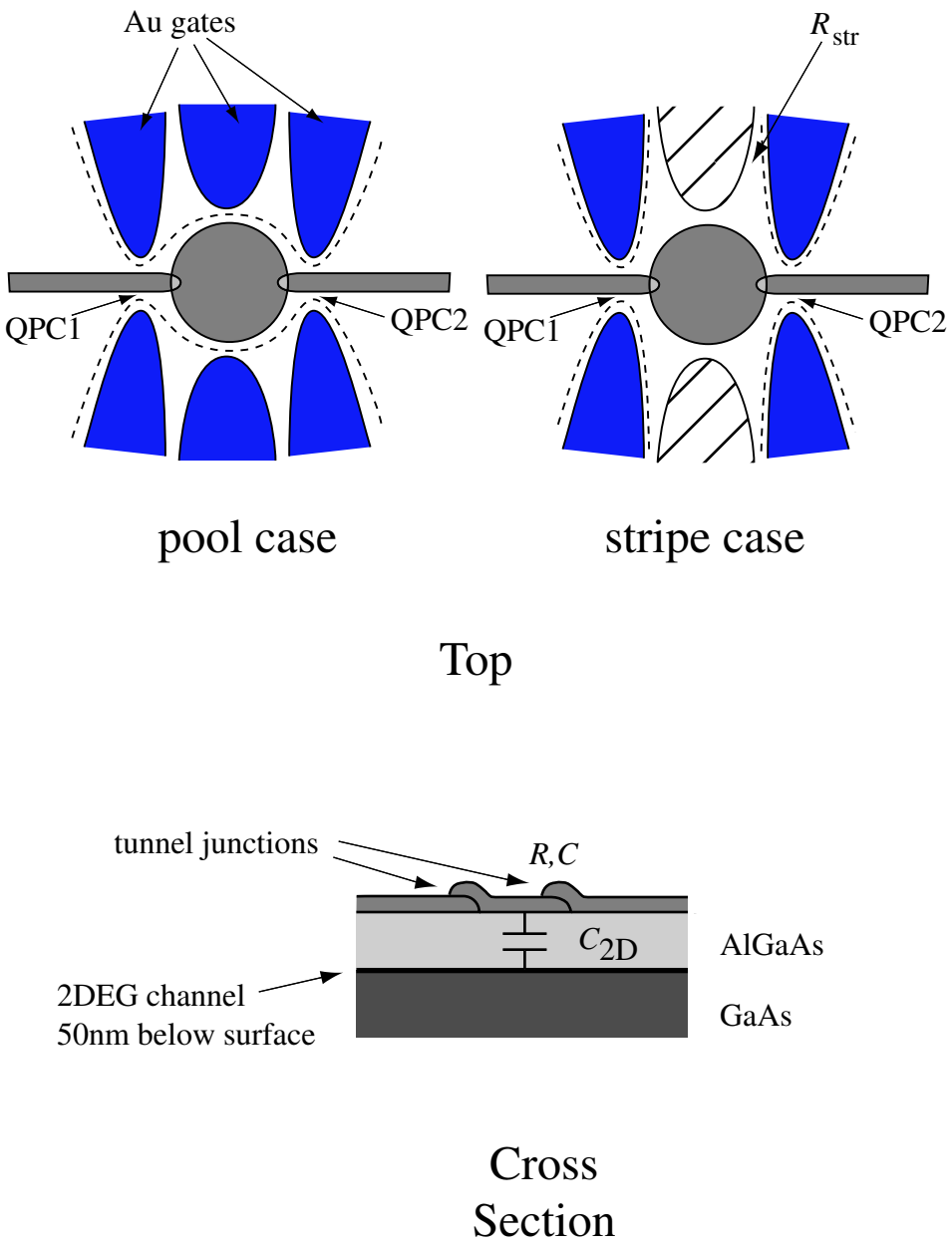

Figure 4.5: Top: expanded view of the center of the sample, showing the Al/AlO_x tunnel junctions, and the depletion of the 2DEG. The energized gates are colored. Bottom: cross sectional view of the sample, showing the vertical coupling between the SET and the 2DEG.

Ohmic contacts are made to the 2DEG, six Au gates are fabricated using e-beam lithography. The Au gates can be used to deplete the electrons beneath them by application of a negative gate voltage V_g. The Al/AlO_xbased S-SET is fabricated in a second lithography step with the SET located in the center of the Au gates. An electron micrograph of the sample is shown in Fig. 4.6.

Note that as shown in the larger diagram (Fig. 4.4) the S-SET leads extend over the 2DEG to macroscopic contact pads. For the vast majority of their length they are well away from the Au gates and the 2DEG beneath them is independent of V_g. When we apply a gate voltage V_g to all six Au gates, the electrons immediately beneath them are depleted, leaving a small pool of electrons beneath the S-SET, as illustrated in the top view of Fig. 4.5. This pool is connected to the rest of the 2DEG (held at ground) only by two quantum point contacts (QPCs) with conductances $1/R_{\rm QPC}$ (assumed equal) as shown in the illustration. When all six Au gates are energized as described above, we say that the electrons are confined in the "pool" geometry. We do not refer to the pool as a quantum dot since for these experiments the QPCs are sufficiently open that the charge in the pool is not quantized and discrete energy levels have not formed.

Because the Au gates can be biased independently, we can also apply V_g to only the four outermost gates which form the QPCs. As before, the electrons beneath the S-SET are coupled to ground through the QPCs. In addition, however, they are now coupled through a resistance $R_{\rm str}$ to two large reservoirs of electrons located between the four outermost gates, as illustrated in Fig. 4.5. The reservoirs are in turn capacitively coupled to the 2DEG held at ground with a capacitance $C_{\rm str}$. When only the four outer gates are energized, we say that the electrons in the 2DEG are confined in the "stripe" geometry. We observe significant differences between the measured S-SET conductance $G_{\rm SET}$ versus applied gate voltage V_g for the two different geometries,

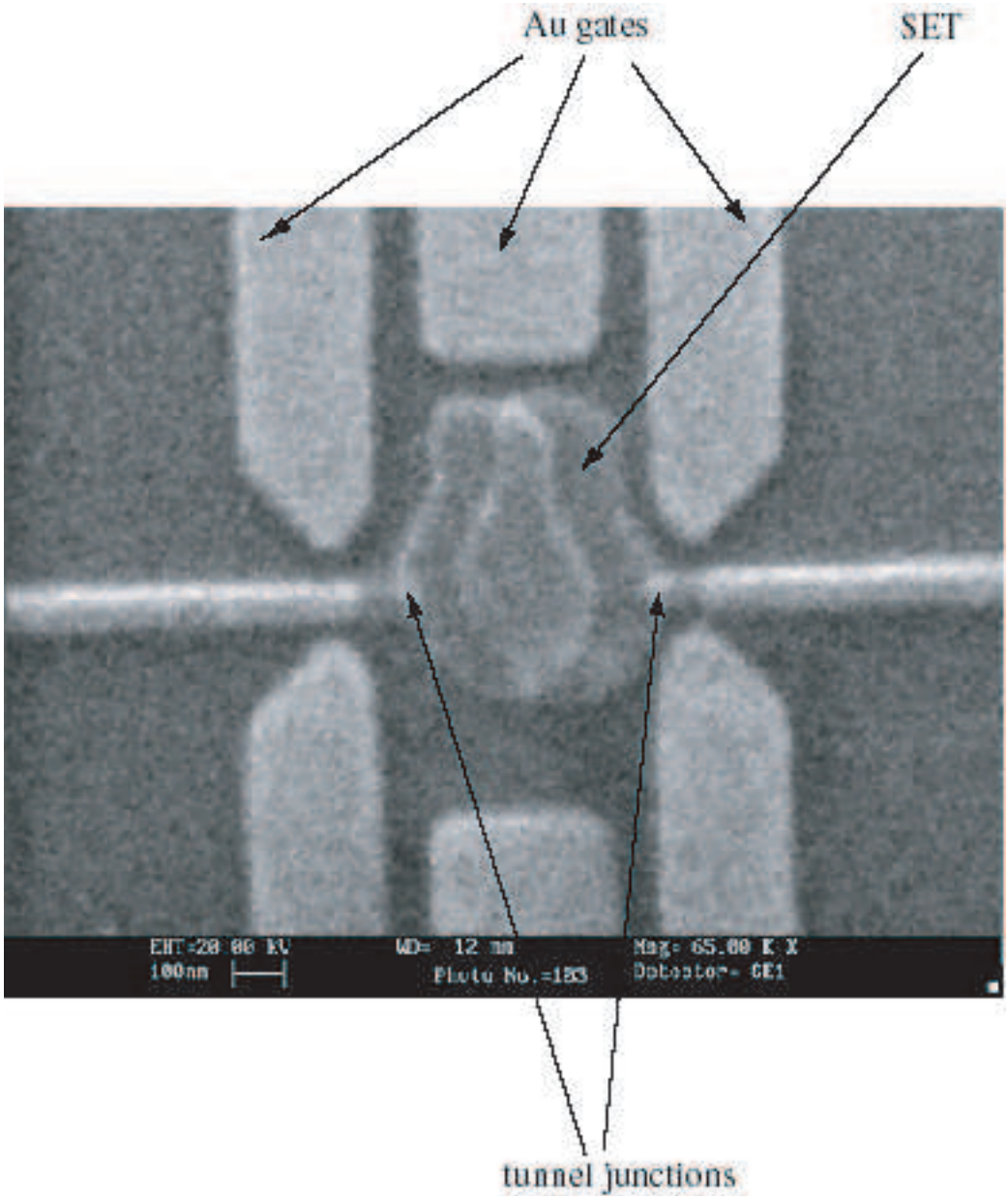

Figure 4.6: Electron micrograph of a test sample. The white bar at the lower left represents 100 nm. The tunnel junctions are visible as overlaps between the leads and the island. The sizes of the junctions in this sample are about 50 nm × 50 nm, and the thickness of the oxide layer is about 10 Å.

as will be discussed below.

Regardless of the gate configuration used, we can apply a single model of the environment to our results, as shown in Fig. 4.7. The SET island is connected to its leads through junctions with resistance $R_{1(2)}$ and capacitance $C_{1(2)}$. We assume that the S-SET leads present an impedance $Z_L(\omega)$ to the SET while the 2DEG electrons have a total impedance $Z_{2\mathrm{D}}$ to ground which is coupled to the SET through the capacitance $C_{2\mathrm{D}}$. Nearly the entire length of the SET leads is far from the Au gates, so that $Z_L(\omega)$ is almost completely unaffected by the gate voltage V_g. The electrons immediately beneath the SET are strongly affected by V_g so that $Z_{2\mathrm{D}}$ will in general be a function of V_g, and may also depend on the configuration of gates used (*i. e.*, on the pool versus stripe geometry). Finally, the SET is also coupled to the Au gates directly by a capacitance C_g. We neglect the possibility of a substantial impedance on the gate lines largely because $C_g \approx 20$ aF is by far the smallest capacitance in the problem. Furthermore, any gate impedance would be substantially reduced since there are six gates whose impedances would combine in parallel. This general model (excluding the small gate capacitance C_g) has been investigated previously [79, 80], but without considering any particular form for the impedances $Z_L(\omega)$ and $Z_{2\mathrm{D}}$.

4.3 Theoretical Results

4.3.1 Calculation of $\mathrm{Re}[Z_t(\omega)]$

The total capacitance of the SET in our samples is now defined as

$$C_\Sigma = C_1 + C_2 + C_{2\mathrm{D}} + C_g \tag{4.28}$$

and the samples are in the limit $E_{J_i} < E_C \ll k_B T$. As a result, theoretical results in the previous sections are directly applicable, *i. e.*, after $K(t)$ and $P(E)$ are calculated

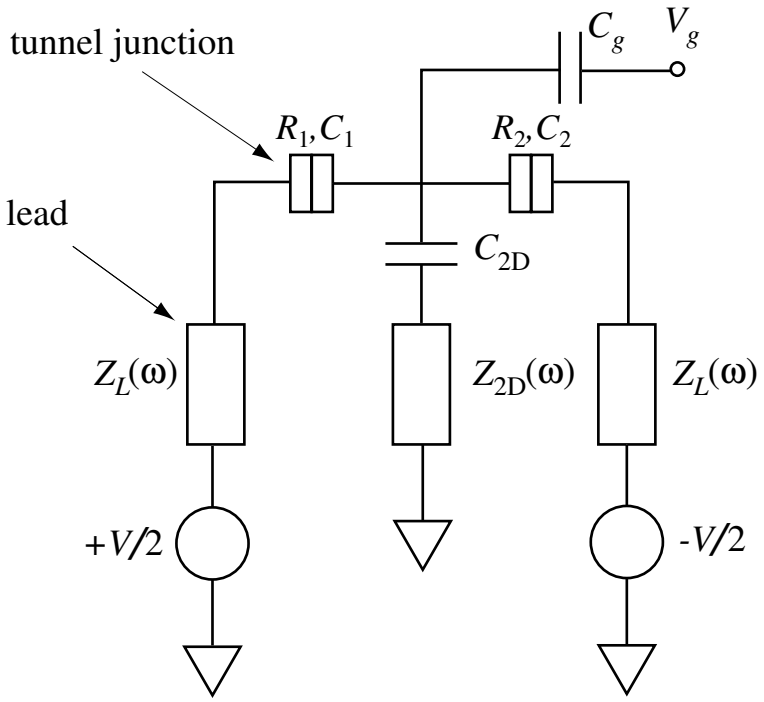

Figure 4.7: Lumped-element circuit for the model system. The SET island is coupled to the macroscopic leads of impedance $Z_L(\omega)$ via tunnel junctions with resistance R and capacitance C. The island is also coupled by a capacitance C_{2D} to the 2DEG whose impedance to ground Z_{2D} can be tuned.

from Re$[Z_t(\omega)]$, $I(V)$ can then be calculated from Eq. 4.27.

4.3.2 Model of the Environment

To calculate the effective impedance sensed by the junctions, we start with the circuit in Fig. 4.7. Once again, standard network analysis is used as in Sec. 4.1.4 to convert the capacitances and impedances into a single effective impedance. The result is given by [79]

$$Z_t(\omega) = \frac{1}{i\omega\widetilde{C} + \widetilde{Y}} \tag{4.29}$$

where

$$\widetilde{C} = \frac{C_\Sigma C_j}{C_{j'} + C_{2\mathrm{D}}} \tag{4.30}$$

where $j' = 2(1)$ for $j = 1(2)$ and

$$\widetilde{Y} = \frac{C_\Sigma^2}{(C_{j'} + C_{2\mathrm{D}})C_{j'}C_{2\mathrm{D}}} \times \frac{(C_{j'} + C_{2\mathrm{D}})C_{j'}C_{2\mathrm{D}} + i\omega(C_{j'}C_{2\mathrm{D}})^2(Z_L + Z_{2\mathrm{D}})}{[(C_{j'} + C_{2\mathrm{D}})^2 + C_{j'}^2]Z_L + C_{2\mathrm{D}}^2 Z_{2\mathrm{D}} + i\omega(C_{j'} + C_{2\mathrm{D}})C_{j'}C_{2\mathrm{D}}(Z_L + 2Z_{2\mathrm{D}})Z_L} \tag{4.31}$$

ignoring terms of order $C_g/C_{2\mathrm{D}}$. To proceed, we need accurate models of $Z_L(\omega)$ and $Z_{2\mathrm{D}}$; we begin by considering $Z_L(\omega)$.

Model of $Z_L(\omega)$

Since our leads are fabricated above the 2DEG, which acts as a ground plane, it is appropriate to model them as transmission lines [81]. The most general form for the impedance Z_{tr} of a lossy transmission line terminated in a load Z_L is given by

$$Z_{\mathrm{tr}} = Z_0 \frac{Z_L + Z_0 \tanh\gamma\ell}{Z_0 + Z_L \tanh\gamma\ell} \tag{4.32}$$

where Z_0 is the characteristic impedance of the line, γ its complex propagation constant and ℓ its length. At the relatively low frequencies ($\lesssim 10^{11}\,\mathrm{Hz}$) considered here, it is reasonable to ignore the inductive reactance of the line and treat it as a simple RC line with a resistance and capacitance per unit length r_ℓ and c_ℓ. Doing so, we have that $Z_0 = \sqrt{r_\ell/i\omega c_\ell}$ and $\gamma = \sqrt{i\omega c_\ell r_\ell}$. Looking out at the line from the sample, the line termination Z_L is provided by the bias circuitry, which typically presents a low impedance $\lesssim 50\,\Omega$. For simplicity we therefore take $Z_L = 0$ in Eq. 4.32, and obtain the resulting approximation

$$Z_{RC}(\omega) = \sqrt{\frac{r_\ell}{i\omega c_\ell}} \tanh\sqrt{i\omega r_\ell c_\ell \ell^2} \tag{4.33}$$

which we take as the basic form for the impedance of a finite RC line. This form has been considered previously in the context of incoherent tunneling of Cooper pairs in individual Josephson junctions [82].

While this is likely a fairly accurate description of the impedance of a section of our leads, when used in evaluating the kernel $K(t)$ in Eq. 4.18 it leads to integrals which are analytically intractable. Fortunately a further simplification is possible. We are interested in the low energy part of $P(E)$, which we expect from Eq. 4.19 to be dominated by the long time behavior of $K(t)$, which is in turn dominated by the low frequency part of the impedance Z_{RC}. We therefore expand Eq. 4.33 around $\omega = 0$ to obtain

$$Z_{RC}(\omega) \approx \frac{r_\ell \ell}{1 + (\omega r_\ell c_\ell \ell^2/\sqrt{6})^2} \tag{4.34}$$

as a reasonable approximation to Z_{RC} in the interesting limit.

Another common treatment [84] of the RC transmission line problem is to consider an infinite RC line, whose impedance is given by $Z_0 = \sqrt{r_\ell/i\omega c_\ell}$. Unlike the finite RC line, for which the impedance Z_{RC} approaches a constant $r_\ell \ell$ at $\omega = 0$, the infinite RC line has a $1/\sqrt{\omega}$ singularity at $\omega = 0$ which dominates the long-time limit of $K(t)$ and therefore $P(E)$. The kernel $K(t)$ for the infinite line, as well as $P(E)$, can be calculated exactly in the $T = 0$ limit. At non-zero temperatures, a high-temperature expansion must be performed instead [85].

Model of Z_{2D}

Having developed a model for $Z_L(\omega)$, we now consider a model for Z_{2D}. The particular model will depend on the geometry of the 2DEG. For an unconfined 2DEG, the simplest choice is that Z_{2D} is ohmic with an impedance related to R_{sq} of the 2DEG: $Z_{2D} \approx R_{sq}/3$. When the electrons are confined in the pool geometry, they are coupled

to the remaining 2DEG by two QPCs with conductance $1/R_{\rm QPC}$ (assumed equal), which appear in parallel from the vantage point of the SET. There is likely some shunt capacitance C_{QPC} as well, but the associated roll-off frequency $1/R_{\rm QPC}C_{QPC}$ is typically large ($\sim 10^{11}\,{\rm s}^{-1}$) and we therefore neglect it. So for the pool geometry, we take

$$Z_{\rm 2D} = R_{\rm QPC}/2. \tag{4.35}$$

The stripe geometry is more complex. Here, in addition to the QPC conductances, the electrons beneath the SET are coupled to two large electron reservoirs with resistance $R_{\rm str}$ located between the outermost Au gates. At their narrowest, the reservoirs are $0.6\,\mu$m wide, but broaden in five sections to a width of $500\,\mu$m. Each section contributes roughly $2R_{sq}$, so that $R_{\rm str} \approx 10R_{sq} = 200\,\Omega$. These reservoirs are in turn coupled to ground capacitively through a capacitance $C_{\rm str}$, which we estimate from the size of the reservoirs to be on the order of 0.3 pF. Using $Z_{\rm 2D}^{-1} = 2(R_{\rm QPC}^{-1} + Z_{\rm str}^{-1})^{-1}$ where $Z_{\rm str} = R_{\rm str} + 1/i\omega C_{\rm str}$ we find

$$Re[Z_{\rm 2D}] = \frac{R_{\rm QPC}}{2}\left[\frac{1+\omega^2\tau_{\rm str}^2 R_{\rm str}/(R_{\rm QPC}+R_{\rm str})}{1+\omega^2\tau_{\rm str}^2}\right] \tag{4.36}$$

where $\tau_{\rm str} = C_{\rm str}(R_{\rm str} + R_{\rm QPC})$. For $\omega^2\tau_{\rm str}^2 \ll 1$, then, $Re[Z_{\rm 2D}]$ approaches $R_{\rm QPC}/2$, while for $\omega^2\tau_{\rm str}^2 \gg 1$, $Re[Z_{\rm 2D}]$ approaches $\frac{1}{2}(R_{\rm str}^{-1} + R_{\rm QPC}^{-1})^{-1}$. The imaginary part of $Z_{\rm 2D}$ in the stripe geometry is nonnegligible only in the vicinity of $\omega \sim 1/\tau_{\rm str}$, so for our purposes we neglect it. In general then, at low frequencies $Re[Z_{\rm 2D}]$ is kept finite by the presence of the QPCs, and at higher frequencies is dominated by the smaller of $R_{\rm QPC}/2$ and $R_{\rm str}/2$.

Decomposition of $Z_t(\omega)$

While the form for $Z_t(\omega)$ given by Eqs. (4.29)–(4.31) is complete, it is generally too complex to make significant headway in calculating $K(t)$. Fortunately, significant

simplification is possible. For typical values of $r_\ell \approx 1 \times 10^6$–$1 \times 10^7\ \Omega$/m and typical line lengths $\ell \approx 0.5$–1 mm, $Z_L(\omega) \gg Z_{2\mathrm{D}}$ for small ω. In contrast, for sufficiently large ω, Z_{RC} becomes quite small ($\lesssim 10\,\Omega$) and the condition $Z_{2\mathrm{D}} \gg Z_L(\omega)$ is usually satisfied. It then becomes possible to decompose $\widetilde{Y}$ in Eq. 4.31 into a low ω part dominated by $Z_L(\omega)$ and a high ω part dominated by $Z_{2\mathrm{D}}$.

For small ω, as long as $Z_L(\omega) \gg Z_{2\mathrm{D}}$, we can safely neglect the terms in Eq. 4.31 involving $Z_{2\mathrm{D}}$. Furthermore, for ω such that $\omega \ll \min(1/C_j Z_L(\omega), 1/C_{2\mathrm{D}} Z_L(\omega))$ we can ignore terms in Eqs. 4.29 and 4.31 that depend explicitly on ω. Making these simplifications, we have that in the small ω, large $Z_L(\omega)$ limit

$$Z_t(\omega) \approx \widetilde{Y}^{-1} = \frac{(C_{j'} + C_{2\mathrm{D}})^2 + C_{j'}^2}{C_\Sigma} Z_L(\omega) \equiv \alpha_1 Z_L(\omega). \tag{4.37}$$

For large ω, we drop terms of order $Z_L(\omega)/Z_{2\mathrm{D}}$, and find that we can neglect the explicit frequency dependence in the denominator of Eq. 4.31 for $\omega \ll c_\ell/(C_{j'})^2 r_\ell \sim 1 \times 10^{16}$ rad/s. In contrast, we cannot necessarily neglect the explicit frequency dependence in the numerator, and find

$$\widetilde{Y} \approx \left(\frac{C_\Sigma}{C_{2\mathrm{D}}}\right)^2 \frac{1}{Z_{2\mathrm{D}}} + i\omega \frac{C_\Sigma^2 C_{j'}}{(C_{j'} + C_{2\mathrm{D}}) C_{2\mathrm{D}}}. \tag{4.38}$$

We combine this with Eq. 4.29 to find in this limit

$$\begin{aligned} Z_t &= \frac{1}{i\omega(C_1 + C_2)C_\Sigma/C_{2\mathrm{D}} + (C_\Sigma/C_{2\mathrm{D}})^2 Z_{2\mathrm{D}}^{-1}} \\ &\equiv \frac{1}{i\omega C_{\mathrm{eff}} + \alpha_2^{-1} Z_{2\mathrm{D}}^{-1}}. \end{aligned} \tag{4.39}$$

Combining this result with Eq. 4.37, we obtain for the real part of $Z_t(\omega)$

$$\mathrm{Re}[Z_t(\omega)] = \alpha_1 \mathrm{Re}[Z_L(\omega)] + \frac{\alpha_2 Z_{2\mathrm{D}}}{1 + [\omega C_{\mathrm{eff}} \alpha_2 Z_{2\mathrm{D}}]^2}, \tag{4.40}$$

which we take as our basic model for the real part of the impedance seen by an S-SET fabricated above a 2DEG ground plane. We believe this model should be applicable

not only to our own system, but to all systems including an SET strongly coupled to 2DEG, for example, samples of the Berkeley group as well [76].

To illustrate the degree of approximation associated with Eqs. 4.34 and 4.40, we show in Fig. 4.8(a) $\mathrm{Re}[Z_t(\omega)]$ for three separate models of the environment; all are based on an RC line with $r_\ell = 2.9 \times 10^6\,\omega/\mathrm{m}$ and $c_\ell = 1 \times 10^{-8}\,\mathrm{F/m}$. The solid line shows $\mathrm{Re}[Z_t(\omega)]$ based on Eqs. 4.29–4.31 and Eq. 4.33, *i. e.*, on the impedance of a finite RC line coupled to a ground plane with impedance $Z_{2\mathrm{D}}$, using the full form for $\mathrm{Re}[Z_t(\omega)]$. The dotted line is $\mathrm{Re}[Z_t(\omega)]$ calculated using the low-frequency version of $Z_L(\omega)$ given in Eq. 4.34 and using the decomposition Eq. 4.40 of $\mathrm{Re}[Z_t(\omega)]$, while the dashed line is the impedance of an infinite RC line using the same values of r_ℓ and c_ℓ (with no ground plane). We have not included a curve using the decomposition Eq. 4.40 and the exact form for a finite RC line in Eq. 4.33 since it is virtually indistinguishable from the full $\mathrm{Re}[Z_t(\omega)]$ shown.

We note that the impedance of the infinite line rises above that of the more realistic forms for frequencies below a few MHz, so that in general it gives more weight to the low frequency modes and may be expected to give a more sharply peaked $P(E)$. More importantly, the low-frequency approximation to $Z_L(\omega)$, while agreeing quite well below $\sim 10^7$ Hz with the exact finite line result, significantly underestimates it for intermediate frequencies below $\sim 10^{12}$ Hz. The approximation may therefore be of limited use for larger bias voltages; for low biases, however, it is likely to be more accurate than a model based on an infinite transmission line, which overestimates the impedance at low frequencies. Finally, at sufficiently high frequencies, the approximate and exact forms for $\mathrm{Re}[Z_t(\omega)]$ converge.

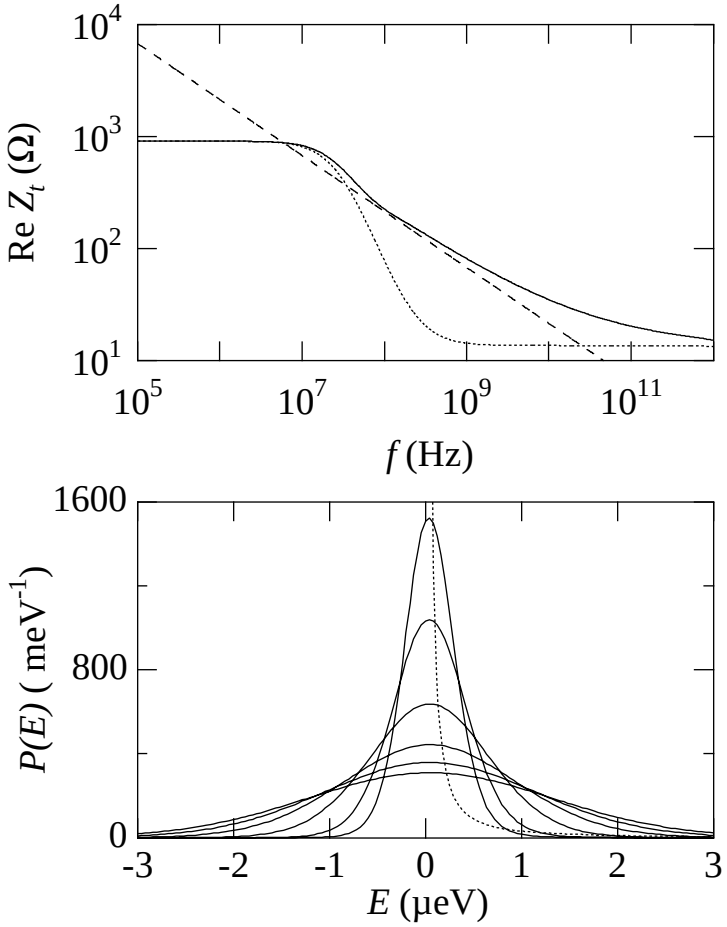

Figure 4.8: (a) Re$[Z_t(\omega)]$ for three different environmental models, all based on a transmission line with $r_\ell = 2.9\times10^6\omega$/m and $c_\ell = 1.0\times10^{-8}$F/m and $\ell = 6.94\times10^{-4}$m. For this graph we have used $Z_{2D} = 100\,\Omega$. Solid line: exact result based on the full forms for $Z_t(\omega)$ and $Z_L(\omega)$. Dotted line: approximate form based on the low frequency approximation to $Z_L(\omega)$ and the decomposition of Re$[Z_t(\omega)]$. Dashed line: infinite line result for the same values of r_ℓ and c_ℓ. (b) Solid lines: $P_s(E)$ for the same transmission line parameters, for (top to bottom) T = 10, 20, 50, 100, 150, and 200 mK. Dashed line: $P(E)$ for an infinite RC line at $T = 0$.

4.3.3 Calculation of $K(t)$ and $P(E)$

Calculation of $K(t)$

Having produced a tractable form for $\mathrm{Re}[Z_t(\omega)]$, we can now proceed to a calculation of $K(t)$ and $P(E)$ through Eqs. 4.18 and 4.19. We begin by noting that when using the low frequency form for $Z_L(\omega)$ in Eq. 4.34, both parts of $\mathrm{Re}[Z_t(\omega)]$ have the same form, namely

$$\mathrm{Re}[Z_t(\omega)] = \frac{R}{1+\omega^2\tau^2} \tag{4.41}$$

for appropriate R and τ. Calculations for $K(t)$ and $P(t)$ for this form have been given in detail elsewhere [86, 87], but emphasize a different range for R and result in different forms for $P(E)$. Using

$$\frac{1}{\omega}\frac{R}{1+\omega^2\tau^2} = \frac{R}{\omega} - \frac{R\tau^2\omega}{1+\omega^2\tau^2} \tag{4.42}$$

and $\coth(\hbar\omega/2k_BT) = 1 + 2/[\exp(\hbar\omega/k_BT) - 1]$ we find that

$$K(t) = R_Q^{-1}\left\{\mathcal{F}_c\left[\frac{R}{\omega}\right] - \int \mathcal{F}_s\left[\frac{2R}{\exp(\hbar\omega/k_BT)-1}\right] dt - i\,\mathrm{sign}(t)\,\mathcal{F}_s\left[\frac{1}{\omega}\frac{R}{1+\omega^2\tau^2}\right] - \mathcal{F}_c\left[\frac{R\tau^2\omega}{1+\omega^2\tau^2}\coth\left(\frac{\hbar\omega}{2k_BT}\right)\right]\right\} \tag{4.43}$$

where $\mathcal{F}_c[f(\omega)] = 2\int_0^\infty f(\omega)\cos\omega t\, d\omega$ and $\mathcal{F}_s[f(\omega)] = 2\int_0^\infty f(\omega)\sin\omega t\, d\omega$ are the Fourier cosine and sine transforms of $f(\omega)$ respectively, taken to be functions of $|t|$. We have ignored terms in $K(t)$ independent of t; since for $P(E)$ to satisfy the normalization condition $\int_{-\infty}^{\infty} P(E)\, dE = 1$ we must have $K(0) = 0$ [49], we will later ensure normalization by adding an appropriate constant in any case.

Of the four terms in curly braces in Eq. 4.43 for $K(t)$, the first three can all be evaluated analytically [85]. An analytic form for the entire kernel has also been found [86], and analyzed for the overdamped case such that $1/\tau$ is large compared to the Josephson frequency $\omega_J = \pi\Delta/\hbar$. However, the range of R and τ in which we are

interested was not investigated. Nevertheless, we have made some progress in certain limits. We note first that the fourth term in Eq. 4.43 depends on the temperature T only through the dimensionless combination $\mathcal{T} = \hbar/(2k_B T\tau)$, and write

$$\mathcal{F}_c\left[\frac{\tau^2\omega}{1+\omega^2\tau^2}\coth\left(\frac{\hbar\omega}{2k_BT}\right)\right] = k_{\mathcal{T}}(t,\mathcal{T}) \tag{4.44}$$

For zero temperature ($\mathcal{T} = \infty$), we have

$$k_{\mathcal{T}}(t,\infty) = \sqrt{\pi}G^{2\,1}_{1\,3}\left(\frac{t^2}{4\tau^2}\,\middle|\,\begin{matrix}0\\ 0,0,\frac{1}{2}\end{matrix}\right) \tag{4.45}$$

where G is a Meijer G function. In the long time limit, this result goes as $-2(\tau/t)^2$.

More generally, for $T \neq 0$, we find that it is important to consider the relative importance of the terms in Eq. 4.43. If we evaluate the integrals which we can treat analytically, we have

$$\begin{aligned} K(t) = -\frac{2R}{R_Q}\Big\{&\frac{\pi k_B T|t|}{\hbar} + \ln(1-e^{-2\pi k_B T|t|/\hbar}) + \gamma \\ &- \ln 2 + i\frac{\pi}{2}\mathrm{sign}(t)[1-e^{-|t|/\tau}] + \frac{1}{2}k_{\mathcal{T}}(t,\mathcal{T})\Big\} \end{aligned} \tag{4.46}$$

where $\gamma \approx 0.577216$ is Euler's constant. In order to compare the relative size of the terms, we evaluate $k_{\mathcal{T}}$ numerically. We find that for $\mathcal{T} \gg 1$, (either low temperature or small τ), $k_{\mathcal{T}}$ decays slowly with time. For long times then the term going as $e^{-|t|/\tau}$ is by far the smallest, and can be neglected. Of the remaining terms, in the long time limit the logarithmic term dominates over $k_{\mathcal{T}}$ and we write the kernel as

$$\begin{aligned} K_l(t) = -\frac{2R}{R_Q}\Big\{&\frac{\pi k_B T|t|}{\hbar} + \ln(1-e^{-2\pi k_B T|t|/\hbar}) \\ &+ i\frac{\pi}{2}\mathrm{sign}(t) - \ln(\pi/\mathcal{T})\Big\} \end{aligned} \tag{4.47}$$

where the constant term $\ln(\pi/\mathcal{T})$ will allow $P(E)$ to be approximately normalized. This is essentially the result of Wilhelm *et al.* [85], and is generally appropriate for

dealing with the high-frequency part of Eq. 4.40 due to the relatively small values of Z_{2D} and C_{eff}. However, this form may also be used for a sufficiently short and narrow section of transmission line.

In the opposite limit, for which $\mathcal{T} < 1$, we find that the approximate analytic result

$$k_{\mathcal{T}}(t, \mathcal{T}) \approx \pi e^{-|t|/\tau} \cot \mathcal{T} \tag{4.48}$$

holds for times $|t|/\tau > \mathcal{T}$. For typical temperature scales available in a dilution refrigerator (T = 20–400 mK), the logarithmic term is very small when Eq. 4.48 is applicable. We can therefore neglect it, and find [78] that

$$K_s(t) = -\frac{2R}{R_Q}\Big\{\pi k_B T|t|/\hbar + \frac{\pi}{2}[\cot(\mathcal{T}) - i\text{sign}(t)](e^{-|t|/\tau} - 1)\Big\} \tag{4.49}$$

This result is typically most useful for dealing with finite RC lines, for which τ^{-1} is typically on the order of $10^7\ \text{s}^{-1}$.

Finally, for $1 \lesssim \mathcal{T} \lesssim 10$, both the logarithmic term and $k_{\mathcal{T}}$ are of the same magnitude for the relevant time scales. The analytic forms for $K(t)$ in Eqs. 4.47 and 4.49 must then neglect some potentially important term.

Calculation of $P(E)$

Having obtained analytic forms for $K(t)$, a straightforward application of Eq. 4.19 allows one to calculate $P(E)$. Letting $g = R_Q/R$, we have from Eq. 4.47 for the large $\mathcal{T}$ limit

$$P_l(E) = \frac{(\pi/\mathcal{T})^{2/g}}{2\pi^2 k_B T}\text{Re}\left[e^{-\pi/g}B\left(\frac{1}{g} - \frac{iE}{2\pi k_B T}, 1 - \frac{2}{g}\right)\right] \tag{4.50}$$

where $B(x, y)$ is the beta function, in agreement with Wilhelm *et al.* [85]. For Z_{2D} we have from Eq. 4.40 that $R = \alpha_2 Z_{2D}$ and $\tau = \alpha_2 C_{\text{eff}} Z_{2D}$. While Eq. 4.50 is only valid

for $g > 1$, in terms of Z_{2D} this condition becomes $Z_{2D} < R_Q/\alpha_2$, so that the result remains valid for quite large Z_{2D} when α_2 is small.

In the small $\mathcal{T}$ limit, we use Eq. 4.49 to obtain [78]

$$P_s(E) = \frac{\tau}{\pi\hbar} e^{\gamma_3(\mathcal{T},g)} \mathrm{Re}[e^{-i\pi/g} \gamma_2(\mathcal{T},g)^{-\gamma_1(\mathcal{T},g)} \times \{\Gamma(\gamma_1(\mathcal{T},g)) - \Gamma(\gamma_1(\mathcal{T},g), \gamma_2(\mathcal{T},g))\}] \tag{4.51}$$

where $\Gamma(x,y)$ is the incomplete gamma function, and $\gamma_1 = \frac{\pi}{g}\mathcal{T} - i\frac{E\tau}{\hbar}$, $\gamma_2 = \frac{\pi}{g}(\cot\mathcal{T} - i)$ and $\gamma_3 = \frac{\pi}{g}\cot\mathcal{T}$. Typically, this will be applied to a finite RC line, for which $R = \alpha_1 r_\ell \ell$ and $\tau = r_\ell c_\ell \ell^2/\sqrt{6}$. In some cases, for a short RC line, it may be more correct to use $P_l(E)$, and substitute the appropriate forms for R and τ in Eq. 4.50 instead.

We show $P_s(E)$ in Fig. 4.8(b) for the same transmission line parameters as used in Fig. 4.8(a). For comparison, we also show the $T = 0$ form for an infinite transmission line given by $P_{\mathrm{inf}}(E) = \sqrt{eV_0/2\pi E^3} e^{-eV_0/2E}$ where $eV_0 = (4r_\ell\alpha_1/R_Q)(e^2/2c_\ell)$. Even at $T = 10\,\mathrm{mK}$, $P_s(E)$ is significantly broader than $P_{\mathrm{inf}}(E)$. While it is possible to obtain an analytic form for $P_{\mathrm{inf}}(E)$ by expanding Eq. 4.18 in the high temperature limit, the resulting expression is of limited use for $E \neq 0$, since it involves only even powers of E and therefore cannot satisfy detailed balance [49]. As a result, such an expression cannot be used to calculate I-V characteristics, for instance, whereas $P_s(E)$ in Eq. 4.51 can.

Ultimately, we are interested in calculating $P_{\mathrm{tot}}(E)$ for the total impedance $\mathrm{Re}[Z_t(\omega)]$ seen by the tunneling electrons. If we were to calculate the total kernel $K(t)$ for the decomposition in Eq. 4.40, it would in general include all the terms in Eq. 4.46. We were unable to find an analytic form for $P_{\mathrm{tot}}(E)$ under those circumstances. However, given the decomposition Eq. 4.40, it is possible to write $K(t) = K_{\mathrm{lf}}(t) + K_{\mathrm{hf}}(t)$ where $K_{\mathrm{lf}}(t)$ and $K_{\mathrm{hf}}(t)$ correspond to the low- and high-frequency parts of $\mathrm{Re}[Z_t(\omega)]$,

with corresponding $P_{\rm lf}(E)$ and $P_{\rm hf}(E)$. The total $P(E)$ is then given by the convolution $P(E) = P_{\rm lf}(t) * P_{\rm tot}(E) = \int_{-\infty}^{\infty} P_{\rm lf}(E - E')P_{\rm hf}(E')\,dE'$, which can be performed numerically.

4.3.4 Multisection Transmission Lines

In our particular case, the sample leads do not have a single width. Instead, they broaden in sections from 0.4 μm (section 1) to 375 μm (section 4) as detailed in Table 4.1 below. As a result, we must generalize Eq. 4.34 to allow for the possibility of multiple sections. In general, we use Eq. 4.32 for a loaded transmission line, beginning closest to the SET with section 1. For this section, Z_L is taken to be the impedance of the second section, which is in turn terminated by the following sections. This cascading process is taken to end at our macroscopic contact pads, which are so broad as to provide very little impedance, and we therefore take $Z_L = 0$ for the last section, so that its impedance is given by Eq. 4.33. We also ignore a short ($\ell = 1\,\mu$m) section with $w = 100$ nm since it contributes only 50 Ω to $Z_L(0)$, and its associated $P(E)$ is very sharply peaked around $E = 0$.

If we were to use the exact form for $Z_L(\omega)$ given by the above cascading procedure, it would be too complex to be of use. Fortunately, a simple approximation gives fairly accurate results. We take

$$\mathrm{Re}[Z_L(\omega)] = \sum_i \frac{r_{\ell_i}\ell_i}{1 + (\omega r_{\ell_i} c_{\ell_i} \ell_i^2/\sqrt{6})^2} \tag{4.52}$$

where r_{ℓ_i} and c_{ℓ_i} are the resistance and capacitance per unit length of section i, and ℓ_i is its length. We use the width w_i and length ℓ_i of each section along with the 2DEG sheet resistance $R_{sq} = 20\,\Omega$ and depth $h = 50$ nm to calculate [88] $r_{\ell_i} \approx R_{sq}/(w_i + 5.8h)$ and $c_{\ell_i} \approx \varepsilon\varepsilon_0(w_i/h + 1.393)$, where $\varepsilon = 13$ is the dielectric constant of GaAs. To find an approximate form for $\mathrm{Re}[Z_t(\omega)]$ we use the result Eq. 4.52 for

Table 4.1: Transmission line parameters for the various sections of the sample leads, with w and ℓ in μm, r_ℓ in MΩ/m, c_ℓ in nF/m, $r_\ell\ell$ in Ω, and $\mathcal{T}$ calculated for $T = 100$ mK.

section	w	ℓ	r_ℓ	c_ℓ	$r_\ell\ell$	$\mathcal{T}$
1	0.4	9	29	1.08	260	37
2	1	57	15.5	2.46	884	0.76
3	10	253	1.9	23	491	3.2×10^{-2}
4	20	375	1.0	46	375	1.5×10^{-2}

$Z_L(\omega)$ in the decomposition Eq. 4.40. For comparison, we plot both this approximate result as well as the exact one obtained from the full form for Re$[Z_t(\omega)]$ in Eqs. 4.29–4.31 and repeated applications of Eq. 4.32 versus frequency in Fig. 4.9 for different values of $Z_{2\mathrm{D}}$. The agreement is very good, especially considering the number of approximations required to develop a tractable approximate form for Re$[Z_t(\omega)]$. The approximate version tracks the exact result very well except between the various corner frequencies of the transmission line sections, where its slope is generally too small. Agreement is better overall for larger values of $Z_{2\mathrm{D}}$, but even for the smallest values is still acceptable.

We can calculate $P_\ell^{(j)}(E)$ for tunneling through junction j for the four section transmission line by choosing either $P_l(E)$ or $P_s(E)$ for a given section based on its value of $\mathcal{T}$ in Table 4.1, and numerically convolving the four functions through

$$P_\ell^{(j)}(E) = P_{1l}^{(j)}(E) * P_{2s}^{(j)}(E) * P_{3s}^{(j)}(E) * P_{4s}^{(j)}(E). \tag{4.53}$$

While somewhat time consuming, this procedure needs to be performed only once for a given temperature since the 2DEG beneath the transmission lines is not affected by the Au gates, and so the transmission line parameters do not change with V_g.

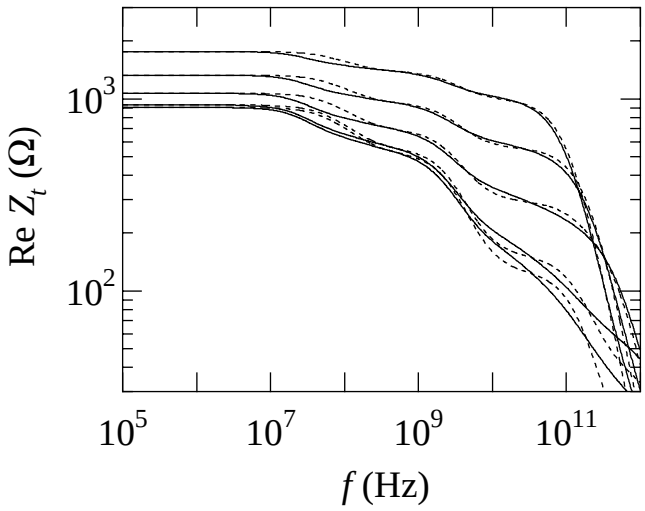

Figure 4.9: Re$[Z_t(\omega)]$ for four cascaded RC lines and a ground plane, using the parameters given in Table 4.1, for (top to bottom) $Z_{2\mathrm{D}} = 6445$, 3227, 1291, 258 and 100 Ω. Solid lines: exact calculation of Re$[Z_t(\omega)]$. Dashed lines: approximate version of Re$[Z_t(\omega)]$ as described in the text.

Finally, we then calculate the total $P_{\mathrm{tot}}^{(j)}(E)$ for tunneling through junction j by convolving $P_{\ell}^{(j)}(E)$ with $P_{2D}^{(j)}(E)$ calculated from $P_l(E)$ for the appropriate value of $Z_{2\mathrm{D}}$. This procedure typically must be performed many times, but can be done relatively quickly. Results for $P_{\mathrm{tot}}^{(1)}(E)$ for tunneling through junction 1 of S2 are shown in Fig. 4.10 for a series of different values of $Z_{2\mathrm{D}}$. For $Z_{2\mathrm{D}} = 0$, we take $P_{\mathrm{tot}}^{(1)}(E) = P_{\ell}(E)$, which is already relatively broad, with a width several microvolts. In contrast, for small $Z_{2\mathrm{D}}$, $P_{2D}^{(1)}(E)$ is very sharply peaked around $E = 0$ and approximates a delta function, as can be seen in the insets (a) and (b) in Fig. 4.10. As a result, $P_{\mathrm{tot}}^{(1)}(E)$ is not strongly affected by $P_{2D}^{(1)}(E)$ until $Z_{2\mathrm{D}} \gtrsim 200\,\Omega$. Finally, for sufficiently large $Z_{2\mathrm{D}}$, $P_{2D}^{(1)}(E)$ begins to dominate and $P_{\mathrm{tot}}^{(1)}(E)$ becomes very broad, indicating the high probability of inelastic transitions. Overall, the trend is for the transmission line to dominate energy exchange for small $Z_{2\mathrm{D}}$, while the 2DEG dominates energy exchange

for large Z_{2D}.

4.3.5 Calculation of I-V Curves

In general, Eq. 4.27 should be used to calculate the I-V characteristics for the S-SET. However, for temperatures and biases small compared to the charging energy E_C of the S-SET, only two charge states, N and $N+1$ where N is the number of Cooper pairs, are important. In this limit, we follow the master equation approach [84]. The change in free energy $\delta f = f_f - f_i$ for changing the island charge from N to $N+1$ (or vice versa) due to tunneling through junction j is a generation of Eq. 4.26

$$\begin{aligned} \delta f^{(j)}_{N\to N+1} &= -\delta f^{(j)}_{N+1\to N} \\ &= 4E_C(N - n_g + 1) - (-1)^j 2\kappa_j eV \end{aligned} \tag{4.54}$$

where $n_g = V_g C_g/e$ is the gate charge and $\kappa_j = \frac{1}{2} + (-1)^j(C_1 - C_2)/2C_\Sigma$ is the fraction of the bias voltage V appearing across junction j. We then use Eq. 4.20 to find the tunneling rates in terms of the sample parameters.

The master equation can be solved exactly when only two charge states are considered [84]. Doing so, and using the detailed balance relation $P(-E) = e^{-E/k_BT}P(E)$, we find

$$I(V) = \frac{\pi^2\Delta^2}{32eR_K} \frac{\sinh\left(\frac{eV}{k_BT}\right)}{\frac{\tilde{r}_2^2}{\widetilde{P}_2}\cosh\left(\frac{\delta f^{(1)}}{2k_BT}\right) + \frac{\tilde{r}_1^2}{\widetilde{P}_1}\cosh\left(\frac{\delta f^{(2)}}{2k_BT}\right)} \tag{4.55}$$

where $\delta f^{(j)}$ is the change in free energy for tunneling in the electrostatically favorable direction ($N+1 \to N$ for junction 1 and $N \to N+1$ junction 2), $\tilde{r}_j = R_j/R_K$, $\widetilde{P}_j = (P_j^+ P_j^-)^{1/2}$, $P_j^\pm = P_{\rm tot}^{(j)}(\mp\delta f^{(j)})$, and $R_K = h/e^2$ is the resistance quantum.

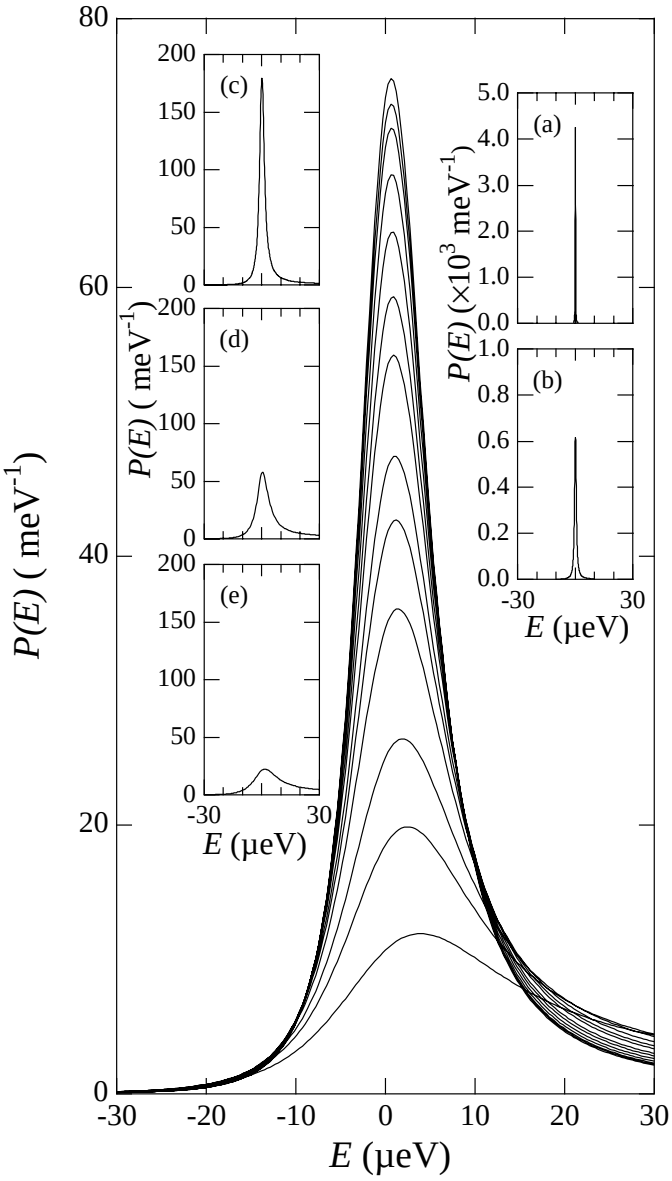

Figure 4.10: Calculated $P^{(1)}_{\rm tot}(E)$ for S2, based on the transmission line parameters from Table 4.1 for a series of values of $Z_{\rm 2D}$. Top to bottom: $Z_{\rm 2D} = 0$, 65, 129, 258, 430, 645, 860, 1291, 1613, 2151, 3227, 4302 and 6445 Ω. Insets: $P^{(1)}_{2D}(E)$ for $Z_{\rm 2D}$ equal to (a) 65 (b) 430 (c) 1291 (d) 3227 and (e) 6445 Ω. Note the scale change for $Z_{\rm 2D} = 65$ and 430 Ω.

4.4 Experimental Results

4.4.1 Measurements

We are interested in the current-voltage characteristics of the SET around zero-bias as a function of Z_{2D}. In the linear I-V regime, the current-voltage characteristics is best described by the conductance G_{SET}. For the pool geometry, $Z_{2D} = R_{QPC}/2$, and can be calculated from the total conductance through the series combination of the two QPCs G_{2D}

$$Z_{2D} = 1/(4G_{2D})$$

under the assumption that the two QPCs are pinched-off more or less equally. For the stripe geometry, we expect that $Z_{2D} \approx R_{QPC}/2$ at low frequencies and $Z_{2D} \approx R_{str}/2 \approx 100\,\Omega$, as discussed earlier.

G_{SET} and G_{2D} are measured with a lock-in technique in a similar configuration. Fig. 4.11 illustrates the set-up for measuring G_{2D}.

Two Stanford Research SR830 lock-in amplifiers are used in this measurement. An ac signal, here 50 mV, taken from the "Sync Out" of one lock-in is scaled down by a voltage divider to 5 μV. The frequency of the signal 11 Hz is chosen to avoid harmonics of 60 Hz, while also avoiding a large $1/f$ noise. Home-made low-noise voltage and current amplifiers are used, with current sensitivity of $\sim$ a few fA and voltage noise of ~ 25 nV/$\sqrt{\text{Hz}}$.

Typically, a DC offset voltage has to be compensated to achieve true zero-bias. This offset bias comes from two sources:

- Since the sample leads are at cryogenic temperature, a thermo-electric voltage V_{thermo} is built up between the leads and the room temperature electronic devices. $V_{thermo} \approx 6.7\,\text{mV}$ in our system. However, since all leads are held at the

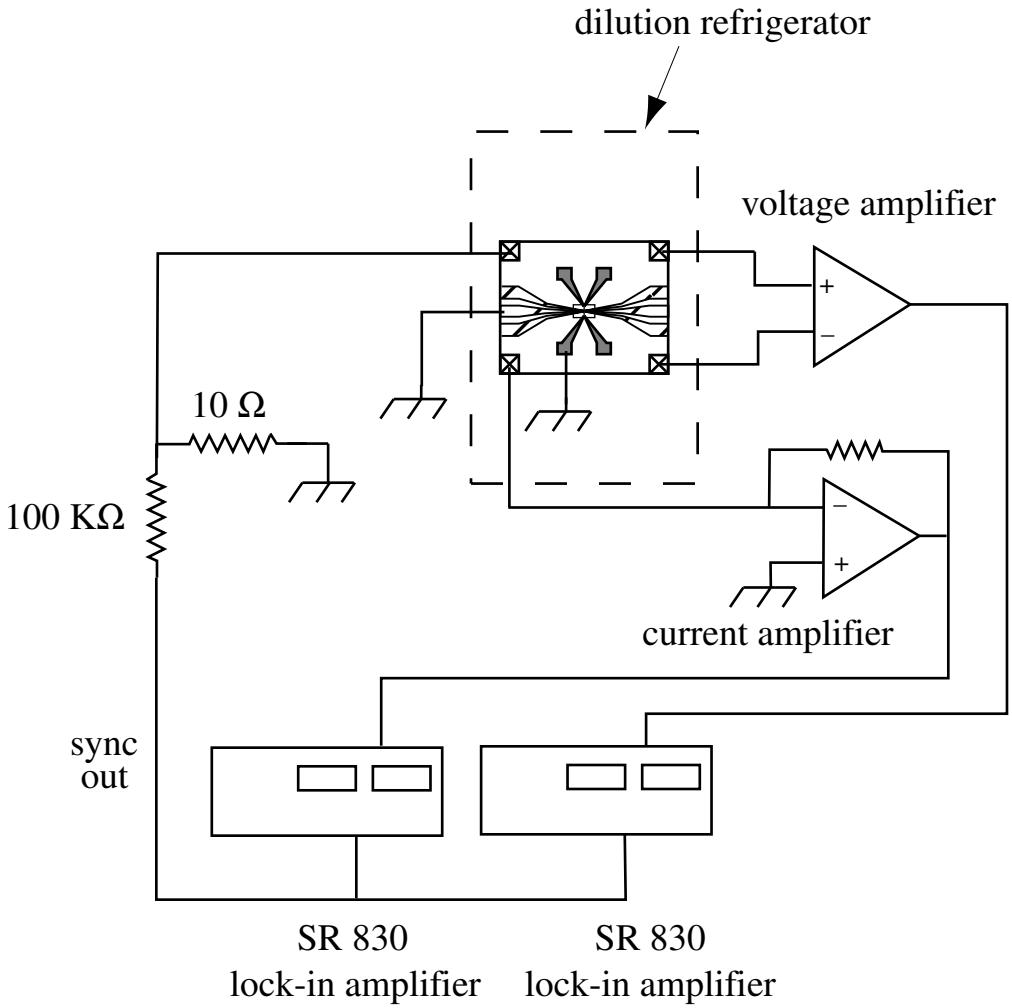

Figure 4.11: Schematic illustration of a differential conductance measurement on the point contacts. The 50 mV signal is scaled down to 5 μV by a 10 $\Omega + 100$ KΩ voltage divider.

Table 4.2: Parameters for samples S1 and S2. Capacitances are in aF, energies in μeV, and resistances in KΩ.

sample	C_1	C_2	C_g	C_{2D}	E_C	R_1+R_2	R_1/R_2	E_{J_1}	E_{J_2}
S1	181	120	20	356	118	305	0.59	5.9	3.5
S2	375	260	20	382	77	63.5	0.6	27.	16.

same temperature, contribution from V_{thermo} across a pair of leads can normally be neglected.

- There is typically an offset voltage at the input of the current amplifier, generated by the OP-amps (OPA128 in our amplifiers). This offset voltage, $V_o \approx 200\ \mu$V, will appear across the sample. Though it is possible to trim V_o, we find it is better to let it stabilize at some value and compensate for it with an external voltage source.

Two samples with the same geometry but different tunneling resistances have been measured. The parameters of those samples are given in Table 4.2:

All the measurements are performed in a sealed meatal enclosure with high frequency noise filtered out based on techniques discussed in Sec. 3.5.3. Unless specified otherwise, the measurements are performed at a mixing chamber temperature of 20 mK.

To make sure the formation of the point contacts are not affected by the presence of the SET, the point contacts are tested independently first, *i. e.*, the left point contact is first tested with the other gates grounded, and a similar test is then performed for the right point contact. The result is shown in Fig. 4.12(a) with the right QPC curve offset by $2e^2/h$ for clarity. Up to six plateaus are clearly distinguishable for

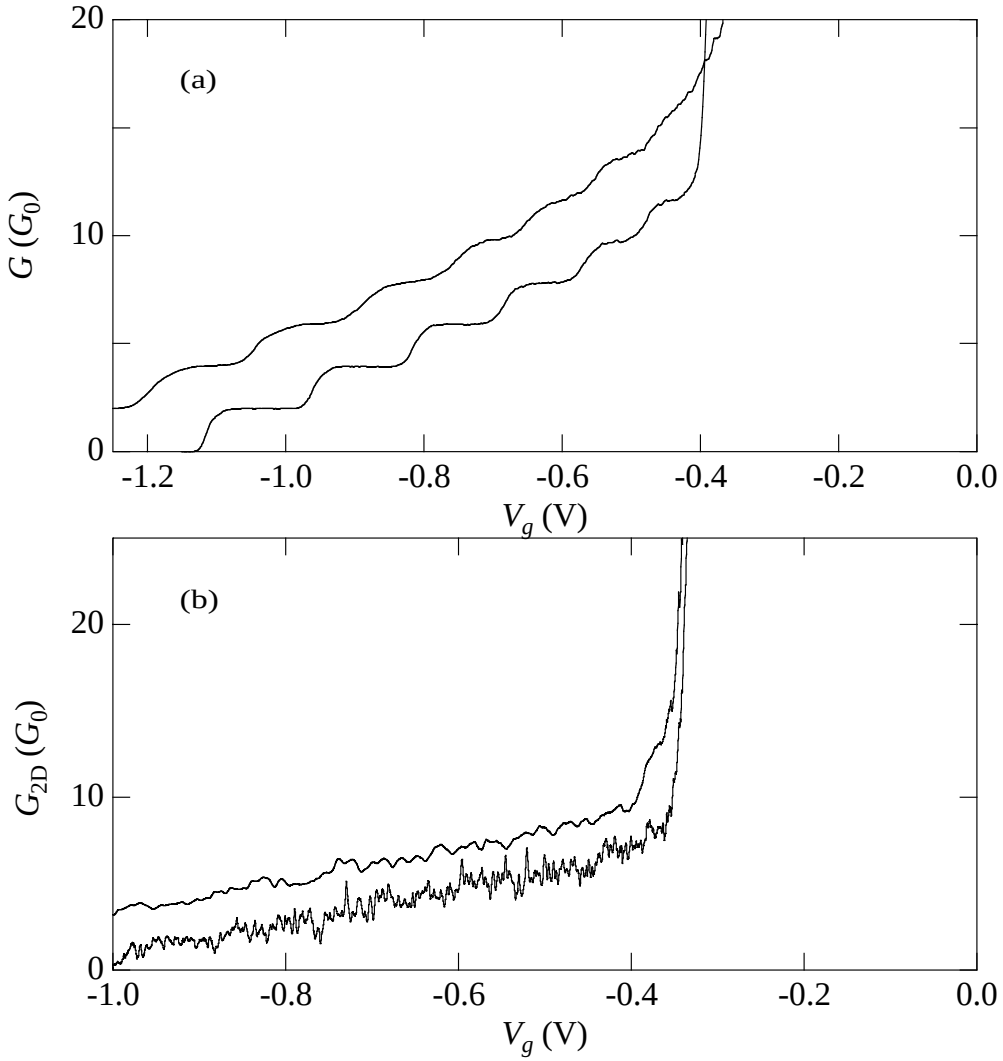

Figure 4.12: (a) Conductance of the quantum point contacts vs. gate voltage. (b) Conductance through the 2DEG for the pool (upper) geometry and stripe (lower) geometry. In both (a) and (b), the upper curve has been offset $2G_0$ for clarity.

each point contact, which is a typical result for similar split gate geometries in the absence of an SET.

In the pool geometry, a single voltage V_g is applied to all six Au gates. The series conductance G_{2D} through both point contacts is shown in Fig. 4.12(b) as the upper curve. After the initial drop, G_{2D} changes quite linearly with V_g until $V_g \approx 1\,\mathrm{V}$ where $G_{2D} = 0$.

In the stripe geometry, V_g is only applied to the outer four gates, with the central two gates held at ground. The result for $G_{2D}$is shown in Fig. 4.12(b) as the lower curve. Not surprisingly, the two curves in Fig. 4.12(b) are almost identical, since the conductance through the 2DEG at DC in both cases is limited by the linear combination of G_{QPC}.

Fig. 4.13 shows the I-V characteristics of the SET around zero-bias when the 2DEG is not confined. A relatively large ($\approx \pm 8\,\mu\mathrm{V}$) linear I-V region is observed, which differs from other systems where a very narrow ($\leq 1\,\mu\mathrm{V}$) linear I-V region is present [39, 76]. This result verifies the prediction of a broad $P(E)$ in Sec. 4.3.4 due to the presence of the multi-section transmission line uniquely present in our SET/2DEG system.

G_{SET} is measured with the lock-in technique described earlier with a smaller AC signal ($3\mu\mathrm{V}$). The results for G_{SET} as a function of V_g in the pool and stripe geometries are shown in Fig. 4.14.

In both cases, change in V_g varies the offset charge on the SET, and numerous Coulomb blockade oscillations are observed in G_{2D} as a result. On the other hand, although G_{2D} changes almost identically in the pool and stripe cases, the behavior of G_{SET} as a function of V_g differs markedly. Most noticeably, the maximum values of G_{SET} in the pool case drops rapidly with V_g after $V_g < -0.4\,\mathrm{V}$ but remain nearly the same in the stripe case even for the most negative V_g. This result agrees with the

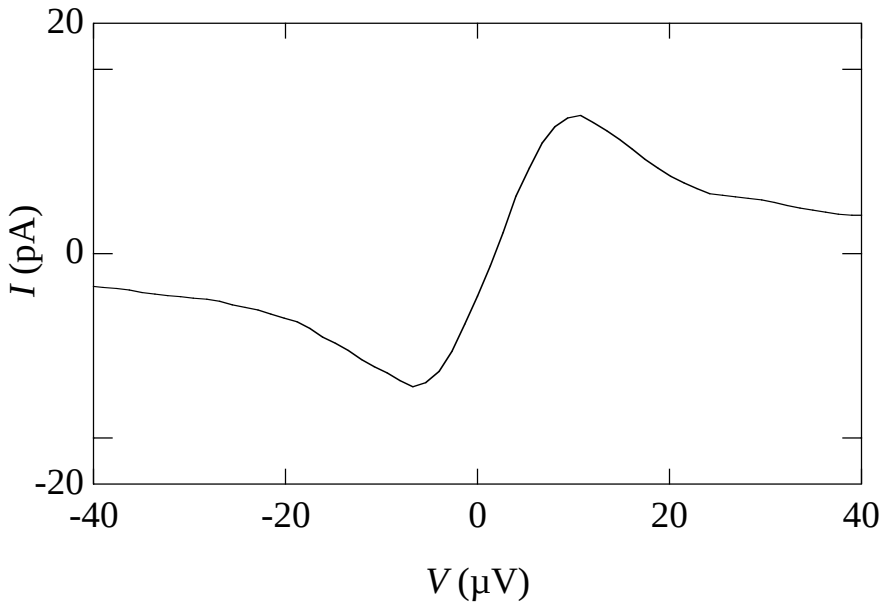

Figure 4.13: Representative I-V curve for Sample 2 around zero-bias with an unconfined 2DEG. The linear region is $\approx \pm 8\,\mu$V.

prediction in Sec. 4.3.4 very well, *i. e.*:

- In the pool case, $Z_{2D} = 1/(4G_{2D})$ and increases monotonically as V_g becomes more negative. $P(E)$ is in turn dominated by the Z_{2D} term and decreases monotonically with increasing Z_{2D}, as can be seen in Fig. 4.10.

- In the stripe case, $Z_{2D} \approx R_{str}/2 \approx 100\,\Omega$ at the relevent frequencies and is not affected by the decrease of G_{2D}.

Fig. 4.15 shows G_{SET} vs V_g at various temperatures, from 50 mK to 200 mK in the pool case. Although the absolute size of G_{SET} is different at those temperatures, similar behavior is observed.

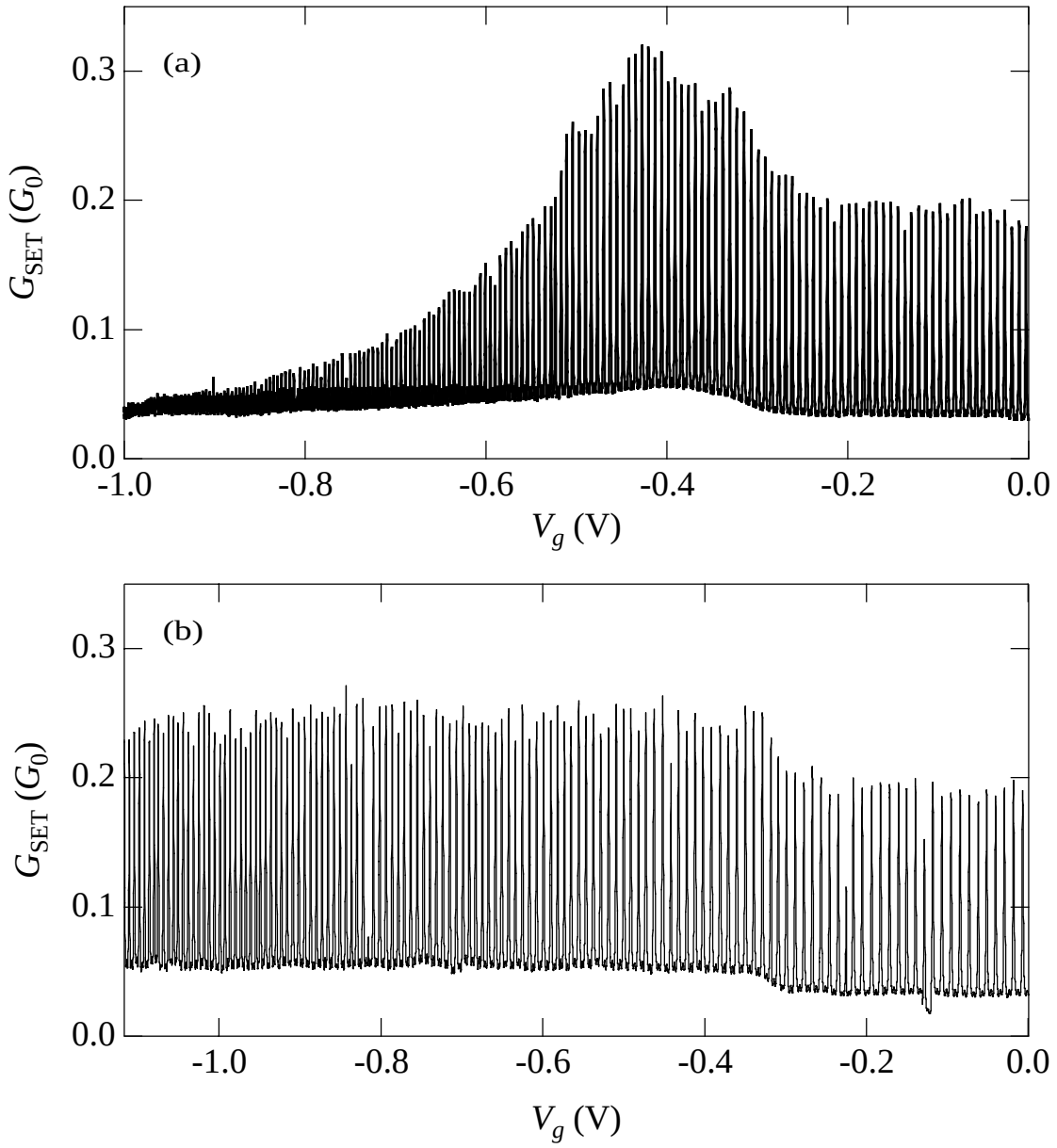

Figure 4.14: (a)Zero-bias conductance of the SET as a function of V_g in the "pool" geometry. (b)Zero-bias conductance of the SET as a function of V_g in the "stripe" geometry. Numerous Coulomb blockade oscillations are observed in both cases due to change in V_g. Markedly different behaviors of the maximum values $G_{\rm SET}$ are observed in the two cases.

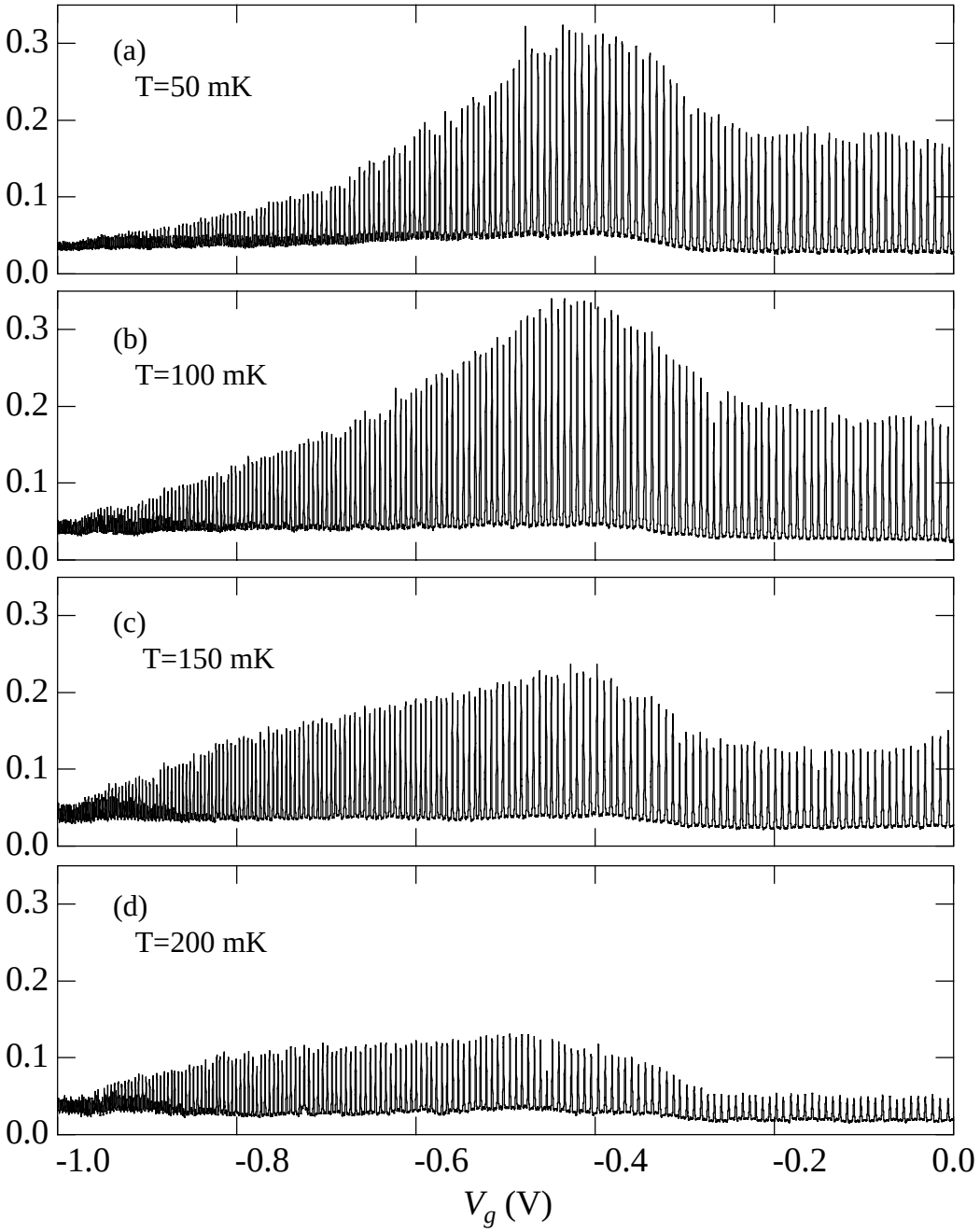

Figure 4.15: G_{SET} vs. V_g for S2 in the pool geometry for $T =$ (a) 50, (b) 100, (c) 150, and (d) 200 mK.

4.4.2 Comparison with Theory

Environmental Theory

In order to make quantitative comparison with the theory, we need to compare $G_{\rm SET}$ at certain offset charges as a function of $G_{\rm 2D}$ with theoretical predictions. To convert V_g to $G_{\rm 2D}$, we fit a smooth varying function to the measured $G_{\rm 2D}$ in Fig. 4.12. This fit is plotted in Fig. 4.16(b) and gives a very good approximation of $G_{\rm 2D}$ for $V_g \leq -0.31$ V ($G_{\rm 2D} \geq 200\,{\rm G}_0$).

The peaks of the oscillations in Fig. 4.14 and Fig. 4.15 correspond to $C_g V_g = Ne$ in Eq. 4.54. They best represent the change in $G_{\rm SET}$ and the theoretical values are easier to calculate at those positions as well. As a result, the peak values are compared with theory. We first record the positions (value of V_g) of those peaks and convert the V_g value to a $G_{\rm 2D}$ value with the fitting function. The result is shown in Fig. 4.16(a) for $T = 100\,{\rm mK}, 150\,{\rm mK}$ and $200\,{\rm mK}$.

The theoretical results $G^c_{\rm SET}$ are obtained from Eq. 4.55 using $P_{\rm tot}(E)$ calculated with the procedure described earlier. In general, the theoretical values overestimate the experimental results by a factor of 40–50. Such discrepancies are not uncommon in small tunnel junction systems [38, 76, 92], but nevertheless complicate comparison with theory. The best we can achieve is to compare the relative change in $G_{\rm SET}$ and $G^c_{\rm SET}$. We choose the reference point to be the maximum value of $G_{\rm SET}$ at $T = 200{\rm mK}$ and $G^{\rm max}_{\rm 2D} \approx 6.5\,{\rm G}_0$, and scale all $G^c_{\rm SET}$ by the same factor (≈ 44). $G^c_{\rm SET}$ after scaling is also plotted in Fig. 4.16 as the heavy solid lines.

The theory correctly predicted the decrease of $G_{\rm SET}$ for $G_{\rm 2D} < G^{\rm max}_{\rm 2D}$, and traces the data at $T = 150\,{\rm mK}$ and $200\,{\rm mK}$ almost exactly. In $G^c_{\rm SET}$, only the scaling factor is a fitting variable, all other parameters being derived from experimentally measured quantities. Considering the complexity of the system, and the approximations

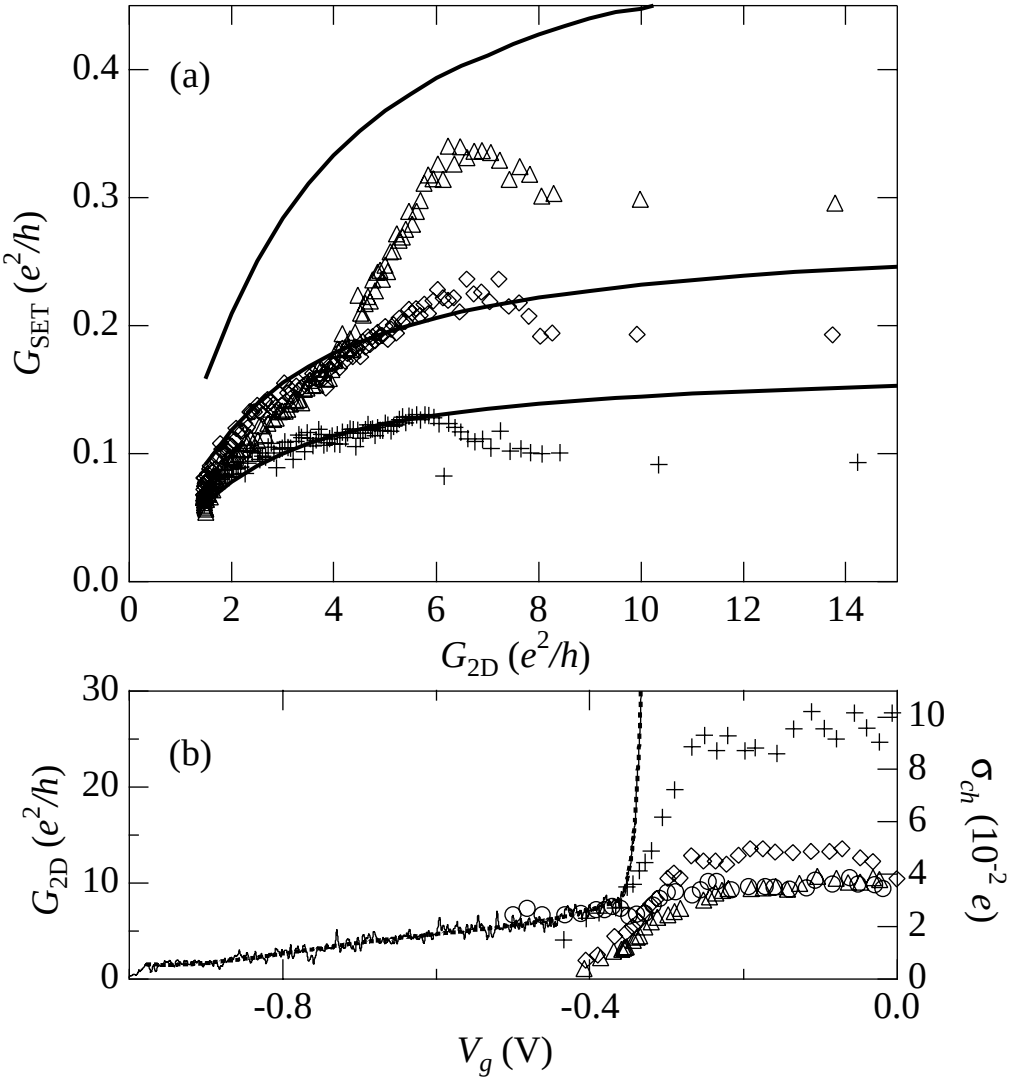

Figure 4.16: (a) Peak values of $G_{\rm SET}$ versus $G_{\rm 2D}$ for $T = 100\,{\rm mK}$ ($\triangle$), $150\,{\rm mK}$ ($\diamond$), and $200\,{\rm mK}$ ($+$). Calculated values $G^c_{\rm SET}$ scaled to equal $G_{\rm SET}$ at its maximum value at $G^{\rm max}_{\rm 2D}$ at $200\,{\rm mK}$ are shown as the heavy solid lines. (b) On the left axis we plot measured $G_{\rm 2D}$ versus V_g (solid line), and the smooth function fitted to $G_{\rm 2D}$ vs. V_g (heavy dashed line). On the right axis we plot values of σ_{ch} in the pool geometry for $T = 100\,{\rm mK}$ ($\triangle$), $150\,{\rm mK}$ ($\diamond$), and $200\,{\rm mK}$ ($+$). We also show σ_{ch} for the stripe geometry ($\circ$).

involved in the calculations, this level of agreement is quite remarkable.

For temperatures higher than $T = 200$ mK, the measured S-SET conductance begins to rise again while the theory predicts $G_{\rm SET}$ should continue to decrease with increasing temperature. However, we expect the environmental theory discussed here to be applicable only for temperatures satisfying the Coulomb blockade condition [86] $k_B T \ll E_C R_Q/(2\pi^2 {\rm Re}[Z_t(0)])$, which for S2 corresponds to $T \approx 240$ mK for typical values of ${\rm Re}[Z_t(0)]$. Failure of the theory between $T = 200$ and 250 mK is in good agreement with this condition.

At $T = 100$ mK and below, the theory also disagrees with the experimental results. Specifically, the measured $G_{\rm SET}$ does not rise as rapidly with decreasing T as predicted by theory. Furthermore, the dependence of $G_{\rm SET}$ on $G_{\rm 2D}$ changes from sublinear to superlinear, so that the S-SET conductance depends more strongly on the environmental impedance than theory predicts. This trend is accentuated at lower temperatures, as can be seen in Fig. 4.15(a) for $T = 50$ mK. In this case $G_{\rm SET}$ is an even stronger function of $G_{\rm 2D}$, and $G_{\rm SET}$ is generally speaking slightly smaller that at $T = 100$ mK (not larger as would be expected from the theory). One possible explanation for a saturation of $G_{\rm SET}$ would be that the electron temperature stops decreasing for some temperature below 100 mK. While it is likely that our electron temperature saturates (data at 20 mK differs only very slightly from the 50 mK data), such effects would not explain the change in dependence on $G_{\rm 2D}$, or a decrease in $G_{\rm SET}$ from 100 to 50 mK.

There is also a lower temperature bound for applicability of the environmental theory, set by the condition $P^{(i)}_{\rm max} E_{J_i} \ll 1$ where $P^{(i)}_{\rm max}$ is the maximum value of $P^{(i)}_{\rm tot}(E)$. This condition must be satisfied for the perturbative result for the tunneling rate in Eq. 4.20 to be satisfied. In our case, we find that for tunneling through junction 1 (for which both E_J and $P_{\rm max}$ are larger), $P^{(1)}_{\rm max} \approx 52$, 41 and 34 meV^{-1}, all

at $G_{2D} = 6.5G_0$ and at $T = 100$, 150 and 200 mK, respectively. In that case we find that $P^{(1)}_{max}E_{J_1} = 1.4$, 1.1, and 0.92 for the same temperatures. In none of the cases is the condition for agreement with Eq. 4.20 clearly satisfied, so that the agreement at 150 and 200 mK is perhaps better that might be expected. Still, if it were a failure of the perturbative expansion which is leading to the disagreement at 100 mK, we would expect the theory to agree for sufficiently low G_{2D} such that $P(E)$ drops below P_{max} at 150 mK. In our case, this occurs at $G_{2D} \approx 4.0G_0$. Based on this argument we would expect theory and experiment to agree at 100 mK over much of the range shown, and only deviate for $4.0G_0 < G_{2D} < 6.5G_0$. Clearly, this expectation does not hold for our data.

Charge Averaging

The data also differs from the environmental theory for $V_g \gtrsim -0.4$ V, *i. e.*, $G_{2D} \gtrsim 6.5$ G_0, as can be seen from Fig. 4.14 and Fig. 4.16(a). In the beginning, for $|V_g| < 0.3$ V, G_{SET} stays about the same until $V_g \approx 0.3$ V, at which point the 2DEG begins to be depleted. After that, G_{SET} rises as V_g becomes more negative (*i. e.*, G_{2D} becomes smaller), until $V_g \approx -0.4$ V where G_{SET} reaches G^{max}_{SET}. On the other hand, only monotonic decline of $P(E)$ is predicted by the theory in Sec. 4.3.4 as G_{2D} decreases in the linear I-V regime. The rise in G_{SET} must come from other sources.

This rise can be attributed to a simple charge averaging effect. It is well known that charge fluctuations in the substrate give rise to $1/f$ noise in SET-based electrometers [89, 90]. Such charge noise typically has a magnitude of $(S_Q)^{1/2} \sim 10^{-4}$ – $10^{-3}e/\sqrt{\text{Hz}}$ at 10Hz and a cutoff frequency (above which the intrinsic SET noise dominates) of about 100–1000 Hz. Due to the presence of the 2DEG, a lossy conductor, it is reasonable to assume that in our case the $1/f$ noise is somewhat larger than is

typical, say $(S_Q)^{1/2} \sim 1\times10^{-2}e/\sqrt{\text{Hz}}$ at 10Hz. If we write $S_Q = 1\times10^{-4}e^2/f \equiv S_0/f$, then the expected mean square charge variance [91] between frequencies f_1 and f_2 is given by $\langle\sigma_{ch}^2\rangle = S_0\ln(f_2/f_1)$. Taking $f_1 = 0.1$ Hz and $f_2 = 1000$ Hz we find $\langle\sigma_{ch}^2\rangle^{1/2} \sim 3\times10^{-2}e$, so that a typical variance of a few hundredths of an electronic charge is not unreasonable.

This charge fluctuation would have the effect of averaging the measured current over an ensemble of charge states centered around the gate charge n_g. Similar effects have been seen in measurements of other S-SET systems [92]. Since the S-SET current is sharply peaked around the charge degeneracy points, we expect that any such charge averaging would tend to reduce the measured peak current, and therefore the conductance G_{SET}. Due to the geometry of our sample, when the 2DEG is confined to a pool, we expect the charge fluctuations to be minimum since the pool is basically isolated from the rest of the 2DEG. Similarly, charge averaging effects in the stripe geometry will be smaller than the unconfined 2DEG case but larger than the pool case.

To test the plausibility of this hypothesis, we calculate the average conductance $\langle G_{\text{SET}}^c\rangle$ given by

$$\langle G_{\text{SET}}^c\rangle = \int_{-\infty}^{\infty} w(n')G_{\text{SET}}^c(V,n')dn' \tag{4.56}$$

where $G_{\text{SET}}^c(V,n)$ is the calculated SET conductance (including the scaling factor) calculated at bias V and gate charge n and $w(n) = \frac{1}{\sqrt{2\pi}\sigma_{ch}}\exp\left[-\frac{(n-n_g)^2}{2\sigma_{ch}^2}\right]$ is assumed to be the probability of finding the SET in charge state n when the gate charge is n_g. We assume $\sigma_{ch} = 0$ for $G_{\text{2D}} < G_{\text{2D}}^{\max}$ in the pool geometry and vary σ_{ch} to have the $\langle G_{\text{SET}}^c\rangle$ exactly match the measured conductance at a given V_g and plot the results in Fig. 4.16(b) for $T = 100$, 150, and 250 mK in the pool geometry, and for the stripe geometry at a mixing chamber temperature of 20mK (estimated electron temperature

roughly 50–70 mK). For the stripe geometry, the initial value of σ_{ch} is $\approx 4\times10^{-2}e$. It then decreases after $V_g \lesssim -0.27\,\mathrm{V}$, and saturates at about $2\times10^{-2}e$ for large negative V_g. This saturation of σ_{ch}, instead of decreasing to zero, corresponds to the fact that in the stripe geometry, the increase in G_{SET} is about half of that in the pool case. This result also agrees with the earlier argument that the charge fluctuation in the stripe is smaller than that of the unconfined 2DEG but larger than that of the pool. For the pool case, the initial values of σ_{ch} are also generally reasonable, being about $4\times10^{-2}e$ at 100 mK, and $5\times10^{-2}e$ and $9\times10^{-2}e$ at 150 and 200 mK. While the cause of the increase in σ_{ch} at 200 mK is unclear, there does not appear to be significant further rise in σ_{ch} for higher temperatures.

To provide further support for the environmental and charge averaging model, we examine I-V characteristics for S1 as shown in Fig. 4.17(a), which show the evolution of the I-V characteristics when the 2DEG is increasingly confined. As the confinement is increased, the current initially rises ($V_g = -0.3$ V) at all voltages, while the peak current remains at a fixed voltage. For $Z_{2\mathrm{D}} = 1613\,\Omega$, the current has increased again, but the peak current has begun to move to higher bias. For $Z_{2\mathrm{D}} = 2151\,\Omega$, the peak current has decreased and moved again to yet higher bias, while the current at higher voltages has generally begun to rise. Finally for $Z_{2\mathrm{D}} = 6453\,\Omega$ the I-V characteristic has become quite broad and the peak has moved outward yet again.

We can understand this evolution by examining the effects of variations in $Z_{2\mathrm{D}}$ and σ_{ch} on the I-V characteristics separately, as shown in Fig. 4.17(b) and (c) respectively. When $Z_{2\mathrm{D}}$ alone is increased, the peak current drops and the voltage at which the peak occurs increases; at the same time, current at higher biases increases. This reflects broadening of $P_{\mathrm{tot}}(E)$ as $Z_{2\mathrm{D}}$ is increased, and a higher probability of inelastic processes. In contrast, when σ_{ch} alone is increased, the current decreases at all bias voltages, and the voltage at which the maximum current appears is more or less fixed.

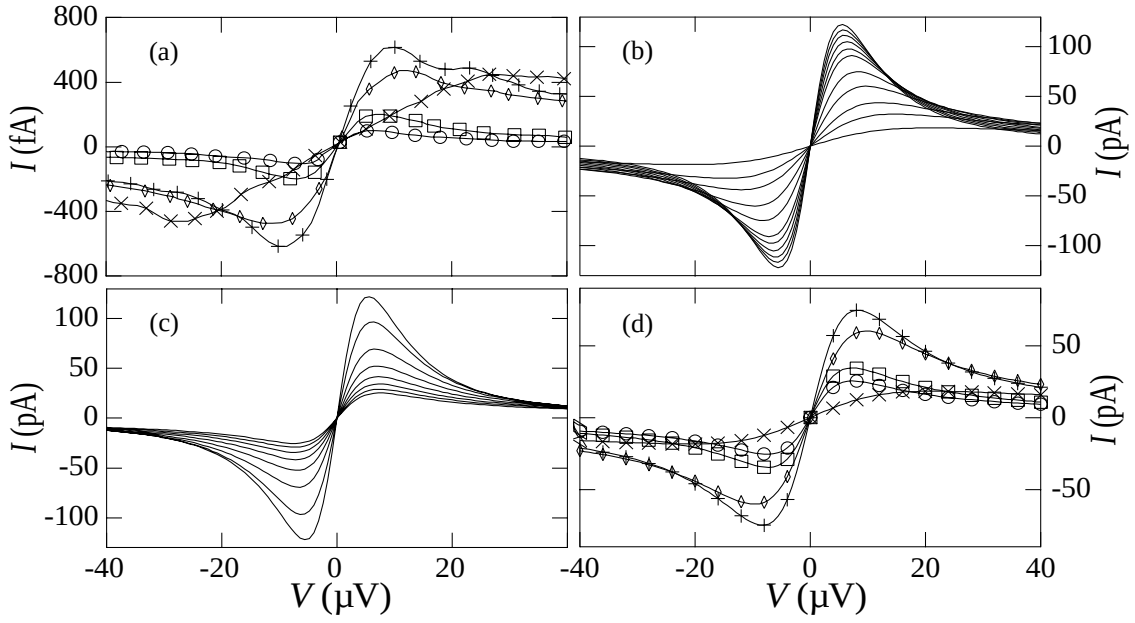

Figure 4.17: (a) I-V characteristics for S1 at an estimated electron temperature of 100 mK for an unconfined 2DEG ($\circ$), $V_g = -0.3$ V ($\Box$), and $Z_{2D} = 1613$ (+), 2151 ($\diamond$) and 6453 Ω ($\times$). (b) Calculated I-V characteristics (top to bottom at peak) for $Z_{2D} = 0$, 129, 258, 430, 645, 860, 1613, 2151, 3227, 4302 and 6453 Ω. Here $\sigma_{ch} = 0$ for all curves. (c) Calculated I-V characteristics for (top to bottom) $\sigma_{ch} = 0$, 1, 2, 3, 4, 5, 6 and $7 \times 10^{-2} e$. Here $Z_{2D} = 0$ for all curves. (d) Calculated I-V characteristics for the same 2DEG condition as in (a). To fit the data at $V_g = 0$ and -0.3 V, we use $\sigma_{ch} = 0.07$ and $0.05e$, respectively. For the remaining curves we take $\sigma_{ch} = 0$.

In order to obtain good agreement with experiment, we must include both variations in σ_{ch} and Z_{2D}, as shown in Fig. 4.17(d). Here, for $V_g = 0$ and -0.3 V, we take $Z_{2D} = 0$ and vary σ_{ch}, while for $Z_{2D} = 1613$, 2151, and 6453 Ω we take $\sigma_{ch} = 0$. Overall the theory agrees with the experimental results quite well (apart from an overall scaling factor), reproducing the initial rise in current with no shift in peak current position, followed by a reduction in current and an outward shift in peak position. The agreement is poor only for $Z_{2D} = 6453\,\Omega$, for which the experimental current is too large in relative terms. Even here, however, the shape of the I-V curve is reproduced nicely.

4.4.3 Discussion

Overall, the agreement between our experimental results and calculations seems quite good, particularly for $T = 150$ and 200 mK. The good agreement of $G^c_{\rm SET}$ and $G_{\rm SET}$ for those temperatures, combined with the accurate predictions of our model for the evolution of the I-V characteristics gives us confidence that our model, despite its complexity, accurately describes our experimental system. In particular, it is clear that both the lead impedance and any impedance which is coupled directly to the S-SET island must be included to give accurate results. In our particular case, charge averaging appears to play an important role when the confinement of the 2DEG is reduced, either for less negative V_g or when the stripe geometry is used. Overall, this improved understanding indicates that S-SET/2DEG systems can be used to test the accuracy of the standard environmental theory in a way which was not previously possible.

On the other hand, the fact the calculated current is much larger than the measured current complicates the comparison between the theory and experiment. The

other discrepancy is that the oscillations in $G_{\rm SET}$ is e-periodic, while in principle they should be $2e$-periodic, as discussed in Sec. 2.1.2. The lack of $2e$-periodicity has been a common problem in superconducting-leads/superconducting-island (SSS) systems [76]. This is generally believed to be caused by photons with energy higher than 2Δ creating excited quasiparticles (out of equilibrium quasiparticles) in the system. If normal metal is present, the quasiparticles can relax in it and the system will be at equilibrium. However, in an all-superconductor system, the excited quasiparicles cannot relax easily and may be trapped on the island for a long time (which is still very short compared to a typical measurement time). In this case, both even and odd charge state subsets will be evenly occupied on average. Since a DC measurement is only sensitive to the average charge on the island, even though tunneling still happens primarily between states within each subset and changes the island charge by $2e$, currents from both subsets will be measured and a e-periodicity, rather than $2e$ periodicity will be observed. The expected supercurrent around $Q = -e$ should be reduced by a factor of 2 since now it will have a 50% probability in the $n = -1$ state, which is in Coulomb blockade. The supercurrent could be supressed further since it has been believed that the presence of quasiparticles will "poison" the coherent tunneling of Cooper pairs [63, 102].

Since we have no control of the out of equilibrium qusaiparticles, the theory we use does not consider the tunneling between the two subsets, As a result, it predicts a monotonic decline in $G_{\rm SET}$ as the temperature is increased. Experimentally, however, a non-monotonic behavior is observed for $G_{\rm SET}$ as a function of the temperature, as illustrated in Fig. 4.18.

$2e$-periodicity has been previously observed on samples with a superconducting island and normal metal leads [93]. Recently, $2e$-periodicity, and supercurrent comparable to the theoretical predictions have also been achieved on all superconducting

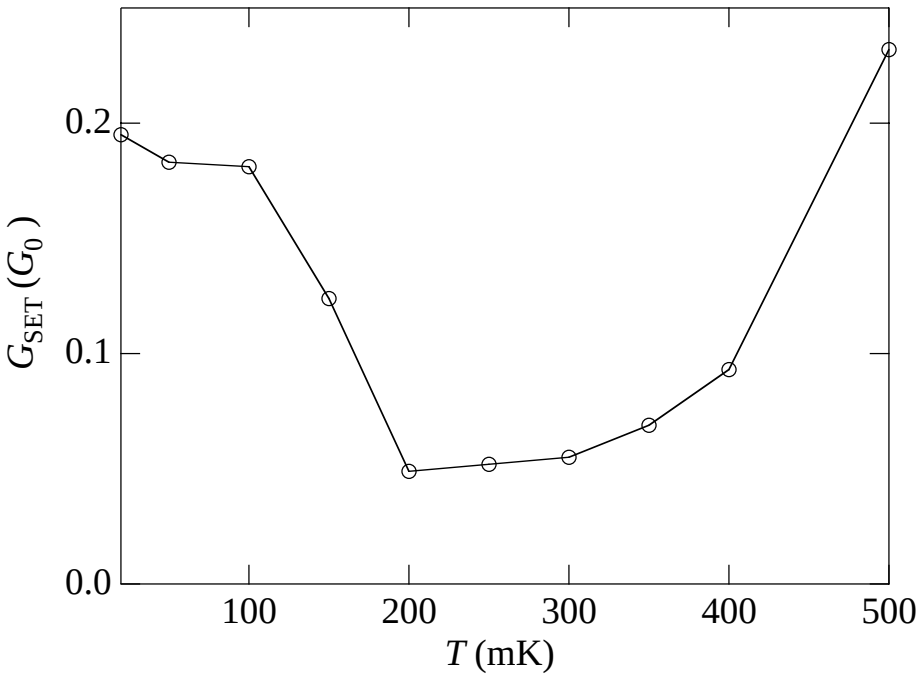

Figure 4.18: G_{SET} measured at $C_g V_g = Ne$ for an unconfined 2DEG as a function of temperature. A non-monotonic behavior is observed.

S-SETs [63, 103]. In those S-SET samples, normal metal leads (Cu with 3 wt. % Al) reach very close to the SET island and only the last section of the leads ($\lesssim 1\ \mu$m) is made of Al. The Cu leads close to the SET serve as "quasiparticle traps" to prevent excited quasiparticles from building up on the SET island. Furthermore, a non-monotonic temperature dependence of G_{SET} similar to that observed in our system has been observed and predicted by Joyez *et al.* [63] in a model for which the population of the two subsets obeys the Boltzmann distribution. Such a distribution could be included in our model as well and compared with the results once the out of equilibrium quasiparticle problem is solved experimentally.

Another means of achieving $2e$ periodicity has been proposed by researchers at NIST. In this approach, one of the Al evaporations is performed in an environment

with a small amount of oxygen present. It is known that oxygen doping will decrease the gap energy in a superconductor [101]. By selectively doping oxygen during the lead evaporation, the superconducting energy gap of the island can be made higher than that of the leads. As a result, excess quasiparticles will quickly tunnel out of the island instead of being trapped on it for a long time.

Employing these techniques, together with the improved microwave filtering techinque discussed in Sec. 3.5.3, will hopefully improve the size of the supercurrent, and make the comparison between theory and experimental results more straightforward.

To make this system better suited for systemical testing of the $P(E)$ theory, it can also be simplified by etching away the 2DEG beneath the SET leads. In this case, the leads would no longer act as transmission lines, and would present a low impedance to the junctions. As a result, the calculations can be simplified and the effects of G_{2D} will also be increased.

CHAPTER 5

OTHER DC RESULTS

The S-SET/2DEG system is quite a rich system for which numerous intriguing features have been observed, besides the $G_{\rm SET}$ measurements at low bias discussed in the last chapter. In Section 5.1.1 we will discuss features related to coupling to a resonant mode and photon-assisted tunneling, while in Section 5.2 we will discuss results when the 2DEG is confined into a quantum dot.

5.1 SET Coupled to a Resonant Mode

5.1.1 $I(V, Q_0)$ Surface Plot

The current through the SET is a function of both the vias voltage V and the offset charge on the island Q_0. To have a better understanding of the system, it usually helpful to construct the $I(V, Q_0)$ surface plot. The $I(V, Q_0)$ plot, in turn, is used to determine the various parameters of the sample.

In this measurement, for simplicity, only one of the six Au gates is used while the other five gates are held at ground. The 2DEG is simply a ground plane in this case. The gate, which has a capacitance C_g to the SET, is used to adjust the offset charge $Q_0 = C_g V_g$ where V_g is the voltage on the gate. A series of I-V measurements are then performed with different offset charges Q_0 on the island. For each I-V measurement, the bias voltage across the SET is swept and the current measured in a symmetric four-probe configuration, as illustrated in Fig. 5.1. The symmetric bias ensures that

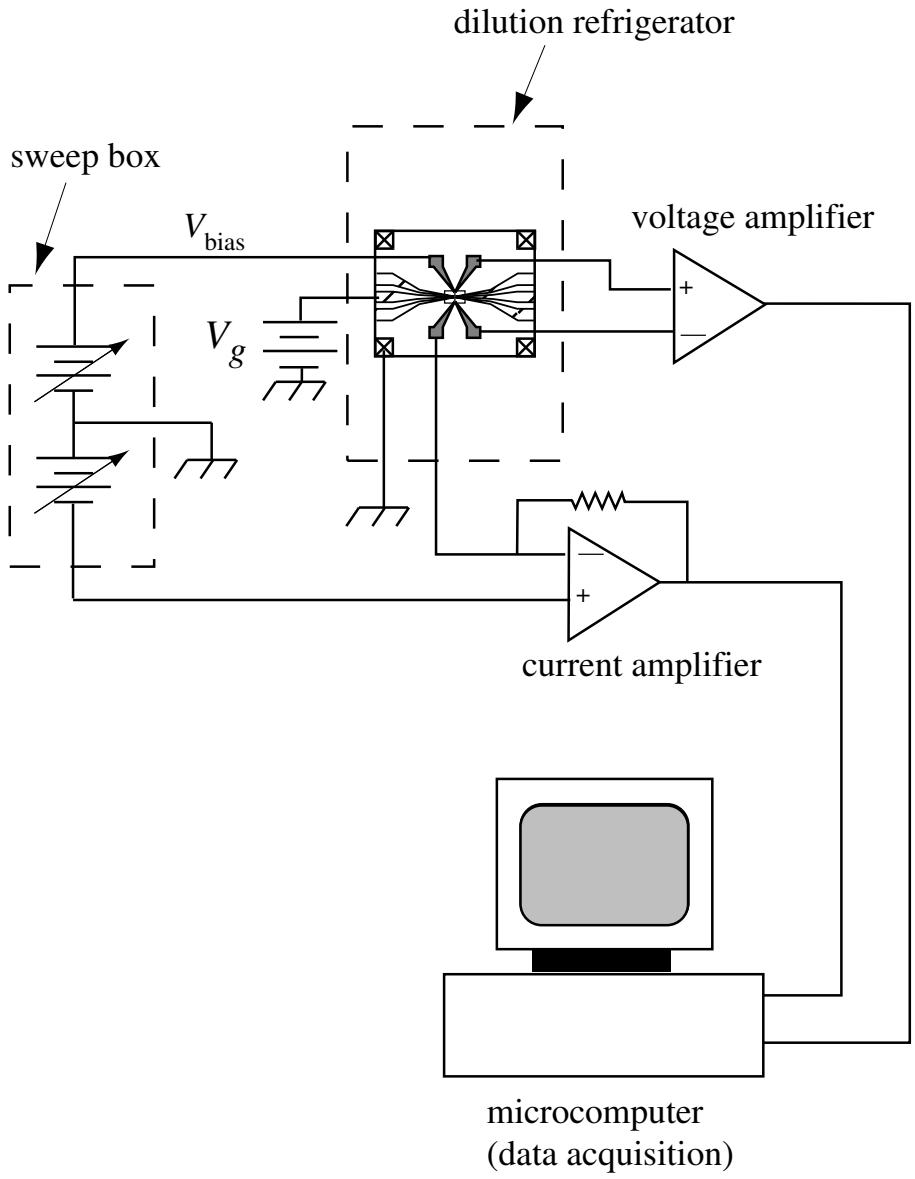

Figure 5.1: Schematic illustration of a dc measurement on the SET. The sweep box generates two symmetric ramping voltages across the SET. The 2DEG is grounded in this measurement.

the effective voltage of the SET island is close to zero. Once again, home-made current and voltage amplifiers are used. Typically, each sweep takes about 15 min. due to the low cut-off frequency (0.1 Hz) used in the current amplifier to minimize current noise. Fig. 5.2 shows a false color image of the $I(V, Q_0)$ surface on sample S1 as discussed in Table 4.2, produced by plotting the absolute value of the current on a logarithmic scale.

All the capacitances are determined beforehand from gate modulation measurements described in Section 2.1.1, except for the junction capacitances C_1 and C_2, which are determined by fitting the slopes of the lines given by Eq. 2.10 to that of the features in the image. Some important capacitances are $C_1 = 181$ aF, $C_2 = 120$ aF, and $C_{2D} = 335$ aF. E_C is then calculated from the capacitances to be 118 μeV. The superconducting energy gap Δ is determined by the minimum threshold for quasiparticle tunneling, which gives $\Delta = 207$ μeV. The junction resistances are determined from their normal state value $R_1 + R_2 \approx 305$ KΩ, and the ratio R_1/R_2 of 0.59 is determined from a best fit in the simulations [78] we will discuss later.

The original offset charge Q_0 is determined by fitting one of the lines to a corresponding known feature, such as the boundary of the Coulomb blockade for Cooper pair tunneling. The rest of the lines are then calculated using Eq. 2.10 and Q_0 determined above. The lines are labeled with the initial and final values of n associated with the corresponding transition. The lines with positive slope correspond to tunneling through junction 1, and those with negative slope correspond to tunneling through junction 2.

A contour plot has been added to the positive half of the plot to accentuate the features, with a step of 10 pA from 0 to 500 pA. The lines and features fit very well with each other, indicating the validity of the parameters calculated and the rules used. We can see clearly the two types of tunneling processes discussed in

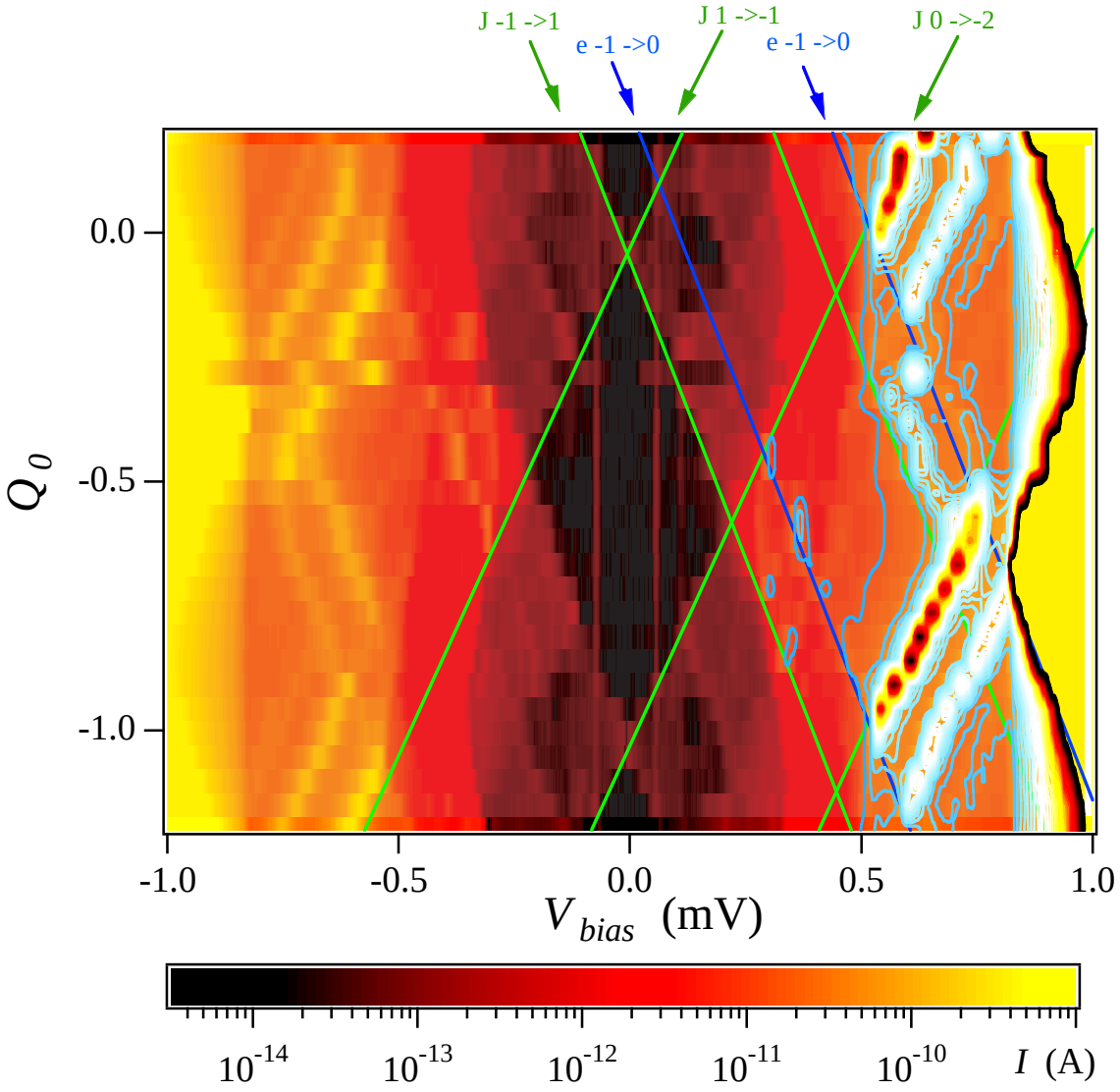

Figure 5.2: False color image of $I(V, Q_0)$ surface with 2DEG unconfined. A color table giving the current scale is shown at the bottom. Transition lines are calculated by the rules in Eq. 2.10. A contour plot is also added to the positive half of the image to accentuate the features.

Section 2.1.2:

- Josephson tunneling, (J-process, green lines).
- Quasiparticle tunneling (e-process, blue lines).

For current to flow through the SET, a cycle of tunneling processes which transfer charge through the two junctions must be completed and repeated many times. A well-known example is the Josephson-quasiparticle (JQP) cycle [35]. It consists of one Cooper pair tunneling through one junction followed by two quaiparticles tunneling through the other, as illustrated in Fig. 5.3. The cycle can not be completed unless all three of the processes involved are energetically allowed. Since Cooper pair tunneling is a resonant process while quasiparticle tunneling is not, the JQP cycle will form a "ridge" along the Cooper pair tunneling line, and it will not start until bias voltage is above the thresholds for the quasiparticle processes. As we can see from Fig. 5.2, there is clearly a JQP ridge along the J: $-1 \rightarrow -3$ line when the voltage is above the e: $-2 \rightarrow -1$ line.

5.1.2 Emission of Photons into a Resonant Mode

On the other hand, there are features that cannot be explained by the usual processes. For example, two more current ridges are visible for voltages between 500 and $800\,\mu$V, along with the usual J: $-1 \rightarrow -3$ line. The fact that they are resonances instead of thresholds make us believe that some kind of Cooper pair process is involved in these current cycles. From the previous chapter, we know that the leads and 2DEG form transmission lines. Since the contact pads have an area $\approx 250\,\mu\text{m} \times 250\,\mu\text{m}$ while the width of the leads is about $20\,\mu$m, it is reasonable to speculate that a resonant mode will be formed in this mismatched transmission line. It therefore seems possible

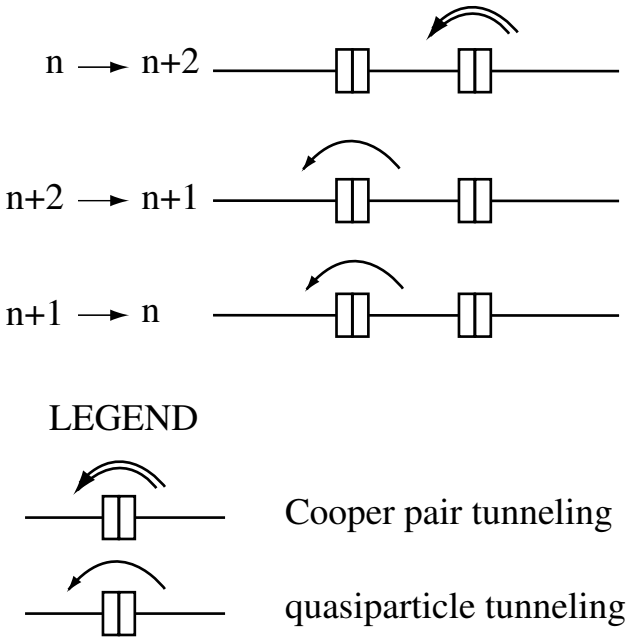

Figure 5.3: Formation of the JQP cycle involving one Cooper pair tunneling through one junction followed by two consecutive quasiparticle tunneling through the other. This charge cycle is repeated many times and on average, a current flows from right to left through the SET.

that the additional current peaks are analogs of the usual JQP peaks, but differ in that Cooper pairs emit one or more photons into the resonant mode. We refer to them as JQP-ph peaks..

To verify our interpretation, we modify the transition rules in Eq. 2.10 by adding a term allowing for emission of photons:

$$\begin{aligned} \sum_i \kappa_i m_i eV &= U(n+\delta m) - U(n) + q\Delta + k\hbar\omega_s \\ &= 2\delta m E_C[-(\frac{Q_0}{e} - n) + \frac{\delta m}{2}] + q\Delta + k\hbar\omega_s. \end{aligned} \tag{5.1}$$

Once again, $E_C = e^2/2C_\Sigma$ is the charging energy, with C_Σ now defined as

$$C_\Sigma = C_1 + C_2 + C_g + C_{2\mathrm{D}} + C_s \tag{5.2}$$

where C_s includes the capacitances of all the other gates held at ground. Here

$$\kappa_i = \tfrac{1}{2} + (-1)^i (C_1 - C_2)/2C_\Sigma \tag{5.3}$$

represents the fraction of voltage applied to junction i, m_i is the number of electrons transferred across junction i, $\delta m = m_2 - m_1$ the change in the island charge, q the number of quasiparticles created, and k the number of photons of energy $\hbar\omega_s$ emitted. Proper choice of m_1, m_2, q and k gives transition rules for quasiparticle, Cooper pair, Cooper pair with photon emission, and $3e$ tunneling processes. These processes are shown schematically in Fig. 5.4

For easy comparison with simulation, we show in Fig. 5.5(a) again the false color image of the $I(V, Q_0)$ plane as well as lines corresponding to JQP and JQP-ph processes. To address the JQP-ph peaks, we adjust $\hbar\omega_s$ so that a one-photon J-ph line coincids with the first JQP-ph resonant line between $Q_0/e = -1.2$ and -0.8. The best fit gives $\hbar\omega_s = 136\,\mu$eV. For the $k = 1$ J-ph process we obtain the condition $eV > (E_C + 2\Delta + \hbar\omega_s/2) \approx 601\,\mu$eV, in good agreement with the observed location of the resonance. The position of the $k = 2$ J-ph line does not match its resonance so well, perhaps due to its small size and the large background current.

As a reality check, we can calculate the parameters of the speculated resonant mode and compare them with the sample parameters. For typical lead widths $w \gtrsim 20\,\mu$m much greater than the 2DEG depth of 50 nm, the effective wavelength of the microstrip $\lambda_e \approx 2\pi c/\sqrt{\epsilon}\omega_s \approx 2.5$ mm [81], where $\epsilon \approx 13$ is the dielectric constant of GaAs. The fundamental resonance corresponds to a length $l = \lambda_e/2 \approx 1.25$ mm, in agreement with the known lead dimensions. Similar current peaks are observed in Sample 2, corresponding to a resonance at $\hbar\omega_s = 160\,\mu$eV. To further verify that the extra current peaks are caused by coupling to the resonant mode, a control sample on a bare GaAs substrate without 2DEG presence is also studied. The important

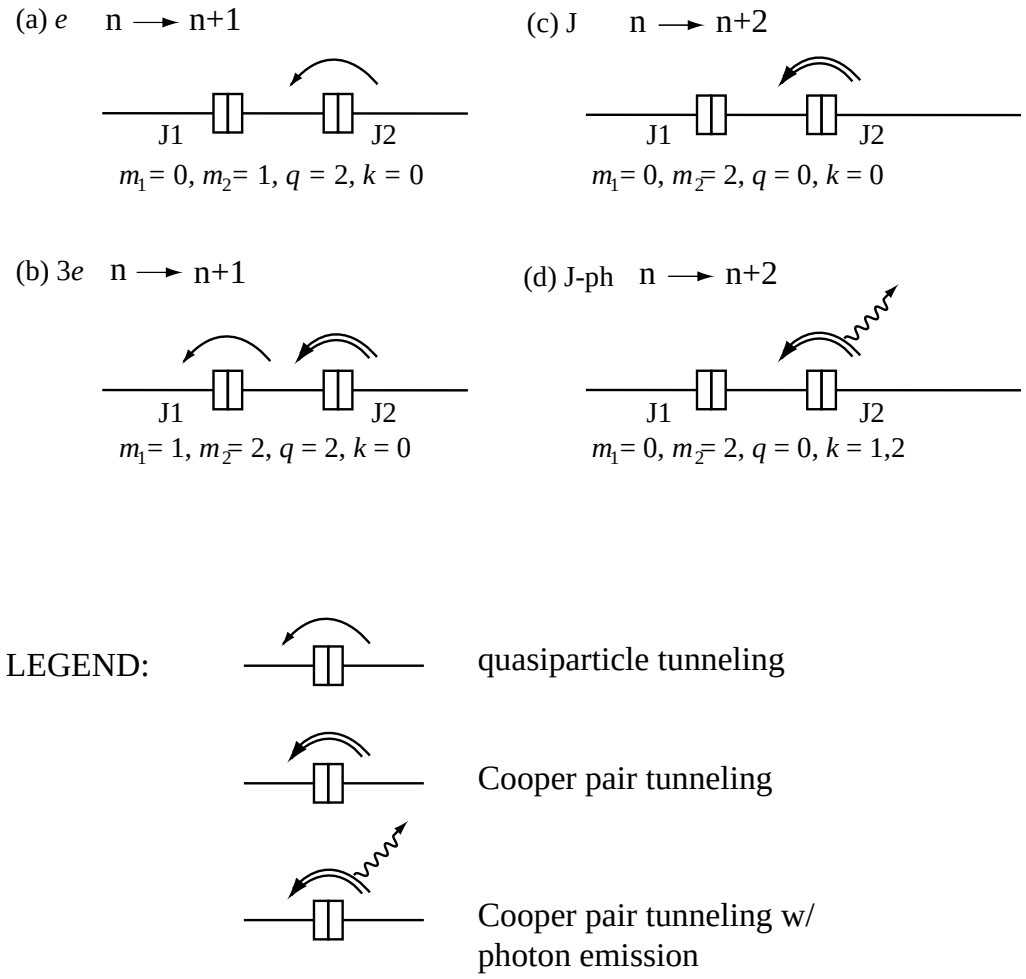

Figure 5.4: Tunneling processes discussed in the text, for positive bias voltage and increasing island charge.

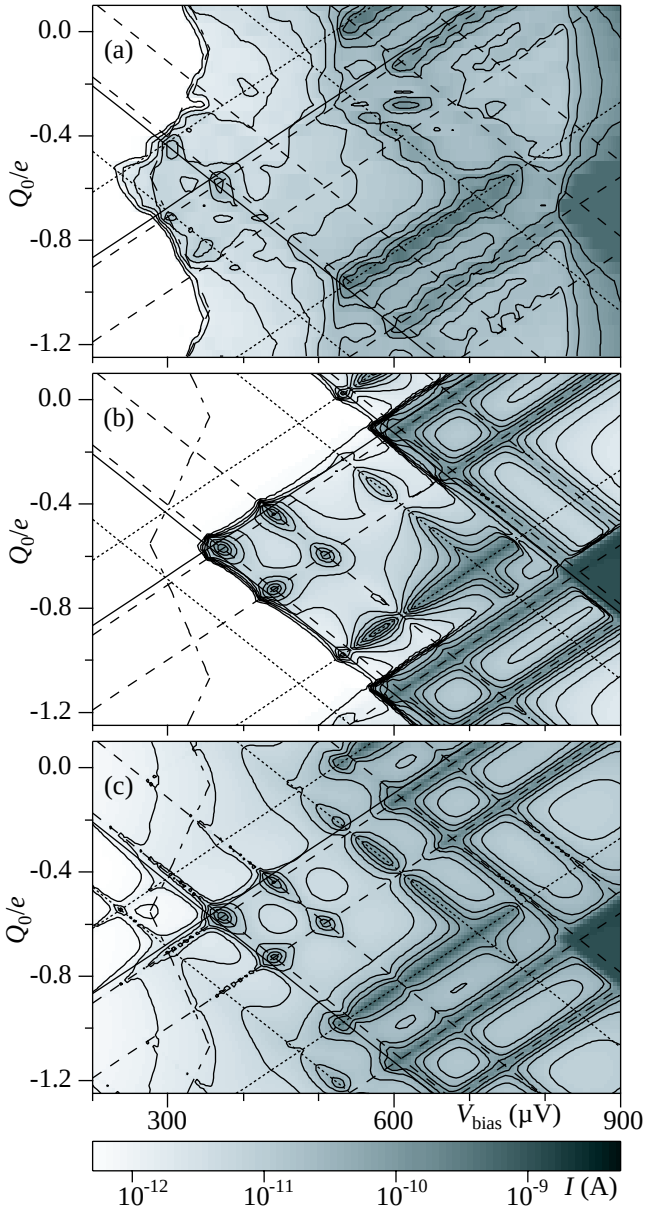

Figure 5.5: (a) Image plot of the I-V plane. Dotted line: J process. Dashed line: J-ph process. Solid line: e process. (b) Simulation results including JQP-ph processes. (c) Simulation results including both JQP-ph and PAT.

parameters for the control sample are $C_1 = 515\,\mathrm{aF}, C_2 = 322\,\mathrm{aF}, \Delta = 198\,\mu\mathrm{eV}, E_C = 91\,\mu\mathrm{eV}, R_1 + R_2 = 91\,\mathrm{k}\Omega$, and $R_1/R_2 = 0.7$. C_1 and C_2 are made larger in the control sample to give a comparable E_C even without a contribution from $C_{2\mathrm{D}}$. As expected, no JQP-ph current peaks are observed in the control sample.

To gain further insight into the features in Fig. 5.5(a), a quantitative comparison between simulation and experimental results is again necessary. In principle, the resonant mode can be modelled in the impedance seen by the junctions and $P(E)$ functions and $I(V)$ curves can be calculated with the methods discussed in the previous chapter. However, both JQP process and coupling to a resonant mode have been studied theoretically before, and here we take a phenomenological approach. We modify the theory of Aleshkin and Averin [95, 96] to write the Cooper pair tunneling rate as

$$\Gamma_{\mathrm{cp}} = \sum_{k=0}^{2} A_k(\Gamma_{\mathrm{qp}} E_J^2)/[4(\delta f - k\hbar\omega_s)^2 + (\hbar\Gamma_{\mathrm{qp}})^2]. \tag{5.4}$$

Here $\delta f = f_f - f_i$ is the change in free energy due to the tunneling of the Cooper pair and Γ_{qp} is the rate of the first subsequent quasiparticle tunneling. The A_k were chosen as $A_0 = 1$ (giving the usual Averin-Aleshkin term) and

$$A_k = \frac{1}{k}(E_C/\hbar\omega_s)^k \exp(-E_C/\hbar\omega_s) \tag{5.5}$$

which represents the weights for independent emission of photons into a single mode [17].

Results of a simulation including the effects of photon emission are shown in Fig. 5.5(b). The agreement is reasonable, especially at higher biases, where the $k = 1$ and 2 JQP-ph lines appear. Moreover, the simulation predicts the appearance of a feature at the intersection of the $k = 1$ J-ph lines for J1 and J2 near $Q_0/e = -0.58$ and $V \approx 374\,\mu\mathrm{V}$. A corresponding peak is observed in the data in Fig. 5.5(a). This feature is an analog of the $3e$ peak [97] but with Cooper pair tunneling replaced by J-ph processes, and we refer to it as the $3e$-ph peak. Sample S1 does not satisfy

the condition $E_C > \frac{2}{3}\Delta$ for the appearance of the usual $3e$ cycle. However, the corresponding condition for the $3e$-ph cycle for it is $E_C > \frac{2}{3}(\Delta - \hbar\omega_s/4) = 115.6\,\mu\text{V}$, which is just satisfied. A similar feature appears in the data (at $Q_0/e \approx -0.73$ and $V \approx 440\,\mu\text{V}$) near the intersection of a $k = 1$ J-ph line for J1 and a $k = 2$ line for J2. A corresponding peak appears at the same location in the simulation.

Despite this level of agreement, some discrepancies exist. The measured current remains substantial down to the $3e$ threshold line between 275–350 μV, while the calculated current in Fig. 5.5(b) nearly vanishes for all Q_0 below the $3e$-ph peak. Furthermore, in the simulation the primary ($k = 0$) JQP peak is strongly suppressed at the intersections with J-ph transition lines; an example occurs in Fig. 5.5(b) at $Q_0/e \approx -0.83$ and $V = 607\,\mu\text{V}$ where the primary JQP peak for J1 intersects a $k = 2$ line for J2. The standard JQP process would begin with the Cooper pair transition $-1 \rightarrow -3$. Our simulation indicates that at this intersection the J-ph transition $-1 \rightarrow 1$ is allowed, and is followed rapidly by a $1 \rightarrow 0$ quasiparticle transition. The transition $0 \rightarrow -1$ is allowed but slow, so that the occupational probability of the $n = -1$ state is quite small (our simulation gives $P_{-1} \sim 0.01$), and the JQP cycle is suppressed. There is however, no clear sign of suppression of the primary JQP cycle in our data.

5.1.3 Photon-Assisted Tunneling

We can account for these discrepancies to some extent by considering photon-assisted tunneling (PAT) due to the environment, here assumed to be the 2DEG in the immediate vicinity of the SET. Since the effective environment temperature T_e can be much larger than the SET electron temperature [58], PAT can be quite significant. Following Siewert and Schön [40], we incorporate it into our calculation

by adding the rate

$$\Gamma_e = \frac{\pi}{e^2 R_i} \frac{R_e}{2R_K} k_B T_e \frac{2\Delta}{2\Delta + \delta f} \exp[-(2\Delta + \delta f)/k_B T_e] \tag{5.6}$$

to all quasiparticle tunneling events for which $\delta f + 2\Delta > 0$, *i. e.*, we only consider PAT for originally energetically forbidden transitions. Fig. 5.5(c) shows the results of a simulation including PAT with much improved agreement. Appreciable current appears at voltages around the $3e$ threshold lines.

In addition, the suppression of the JQP peak at intersections with J-ph lines is largely lifted. This can be seen in greater detail in Fig. 5.6 which shows the calculated I vs Q_0 for $V = 607\,\mu$V, both with and without PAT. The inclusion of PAT increases the primary JQP peaks for both J1 and J2. In the inset, we make a comparison with data from sample S1 at $V = 577\,\mu$V, a voltage below the cutoff for the JQP-ph cycle, so that only the JQP peaks are visible. The JQP peaks for both J1 and J2 are near J-ph transition lines here, and in the absence of PAT the simulation underestimates the actual JQP current. Addition of PAT brings the simulation in much closer agreement with the data.

There are clear indications that there are many excess quasiparticles in our systme, including the lack of $2e$ periodicity at small biases and the quasiparticle-like blockade at small biases around $Q_0 = 0$ as discussed in the previous chapter. These phenomena can in principle all be explained by PAT. However, whether they are intrinsic to SET/2DEG systems or caused by the non-ideality of our experimental set-up is still not clear to us. Once again, improved filtering and improved sample design will help resolve this issue.

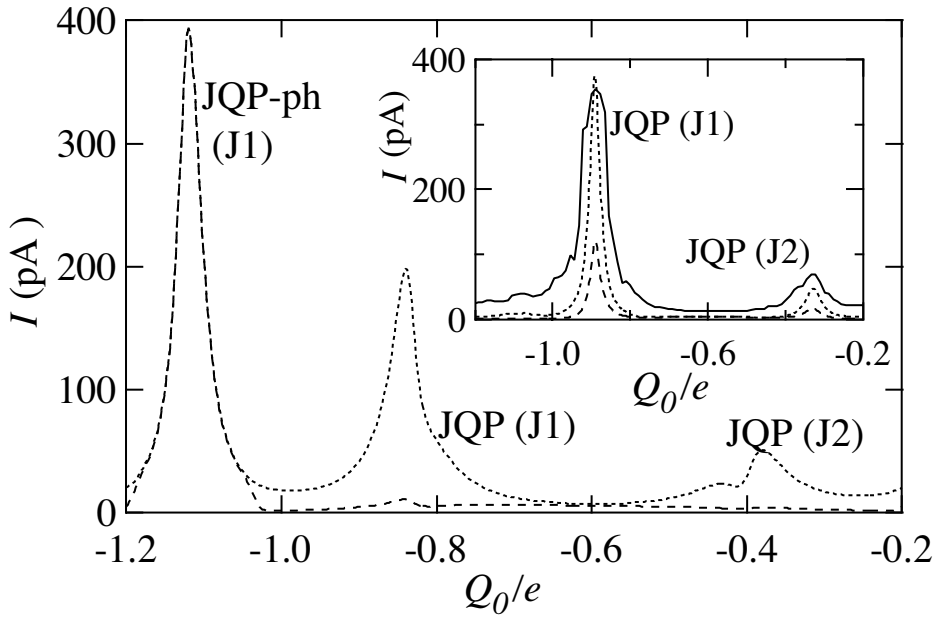

Figure 5.6: Main figure: simulated current with and without PAT. The inclusion of PAT increases the primary JPQ peaks for both J1 and J2. Insert: comparison of the simulation with and without PAT with the measured current. The inclusion of PAT brings the simulation in much closer agreement with the data.

5.2 SET Coupled to a Quantum Dot

Since the SET is very sensitive to offset charge, it has often been used as an electrometer to detect charge on another mesoscopic device such as a quantum dot. In our system, this set-up can be readily realized by applying proper voltages on the Au gates hence confining the 2DEG into a quantum dot. The system is then effectively a strongly coupled double dot system, as illustrated in Fig. 5.7, where C_s is the capacitance between the gate and the SET, C_d is the capacitance between the same gate and the dot, and C_C is the coupling capacitance between the SET and the dot.

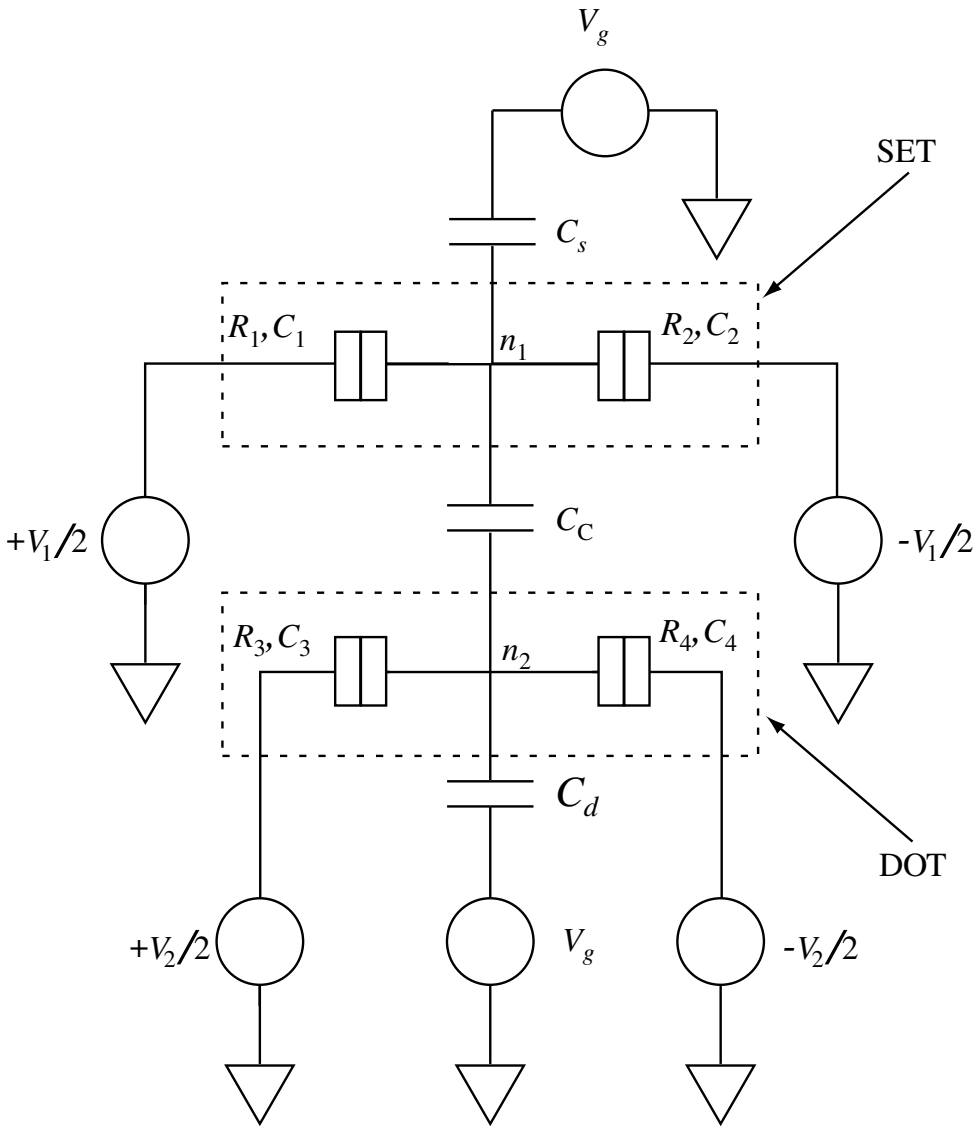

Figure 5.7: An SET coupled to a quantum dot through a capacitance C_C . The dot and SET are biased independently by voltages V_1 and V_2. The gate capacitances C_s and C_d can have significantly different values.

Changing the gate voltage V_g will change the effective offset charges on the islands of both the SET (Q_{0s}) and the dot (Q_{0d}). A calculation of Q_{0s} and Q_{0d} [77] gives:

$$Q_{0s} = C_s V_g + (C_d V_g - N_d e)\frac{C_C}{C_d + C_3 + C_4 + C_{2\mathrm{D}}} \tag{5.7}$$

$$Q_{0d} = C_d V_g + (C_s V_g - N_s e)\frac{C_C}{C_s + C_1 + C_2 + C_{2\mathrm{D}}} \tag{5.8}$$

where n_1 and n_2 are the number of electrons on the island of the SET and the dot, respectively.

Besides the induced offset charge $C_s V_g$ due to the direct coupling between the gate and the SET, Q_{0s} in Eq. 5.7 is also affected by N_d, which is in turn changing as $C_d V_g$ changes in Eq. 5.8. The effects of changes in N_d cannot be neglected in the strongly coupled case, *i. e.*, when C_C is large. Thus we will see a beating effect between the two offset charges in the current through the SET as we sweep V_g. If $C_s \sim C_d$, both N_s and N_d change at roughly the same rate, and little information about the properties of the SET can be determined from the measurements.

However, our sample design is intentionally asymmetric, so that for the bottom central gate $C_s \ll C_d$ (see Fig. 4.6). In this limit N_s changes much more slowly than N_d due to its weaker coupling to the gate. In Eq. 5.8, at the occasional times when N_s changes by one, it will cause a small sudden shift in Q_{0d}. Other than that, $Q_{0d} \approx C_d V_g$, and N_d which equals the integer closest to Q_{0d}/e changes periodically with V_g. *i. e.*, the dot is almost undisturbed by the SET.

On the other hand, the effects of the dot on Q_{0s} cannot be neglected. Since $C_d V_g$ changes continuously while N_d must be an integer, their difference shows a saw-tooth behavior and causes an oscillation in Q_{0s} in Eq. 5.7. If C_C is comparable to $C_d + C_3 + C_4$, this oscillatory term can have an amplitude of a significant fraction of e, with a frequency the same as the change in N_d. On the other hand, the first term in Eq. 5.7 causes a slow but linear change in Q_{0s}. Since $C_d \gg C_s$, the rapidly

oscillating term associated with N_d will complete many periods before N_s changes by one. The different behavior of N_s and N_d verifies that the SET is not only a sensitive electrometer for the dot, it also disturbs the dot in a minimal way.

Once again, similar results are obtained for samples S1 and S2, and we will concentrate results from sample S1. In these measurements, we linearly increase the voltage on the bottom central gate, while monitoring the current I_s through the SET and the dot conductance G_d. I_s is measured at a bias voltage slightly above 4Δ, while G_d is measured with a lock-in technique at zero DC bias. Since for S1 $C_C = 335\,\mathrm{aF}$ is comparable to a typical dot capacitance $\sim 200\,\mathrm{aF}$, a sizable oscillation in Q_{0s}, with peak-to-peak $\sim 0.45e$ is expected. Furthermore, since $C_d = 32$ aF $\gg C_s = 1.5$ aF, we expect N_d will change by roughly 20 before N_s changes by one.

Both predictions are verified by the data. Fig. 5.8(a),(b) show I_s and G_d versus gate voltage V_g, respectively. Singly periodic Coulomb blockade oscillations are observed in G_d, while two periods of oscillation are observed in I_s. From the inset of Fig. 5.8(b), we can see that the faster oscillations in I_s have the same period as the oscillations in G_d, indicating that they are indeed caused by changes in N_d. To verify the origin of the slower oscillation, we measure I_s vs. V_g when the dot charge is not quantized, as shown in Fig. 5.8(c). Singly periodic Coulomb blockade oscillations caused by direct coupling to the gate are observed in I_s in this case, with the same period as the slower oscillation in Fig. 5.8(a), indicating that the slower oscillation in I_s is indeed caused by direct coupling to the gate.

The sensitivity δq_d of the SET referred to the dot charge, which is calculated by comparing the measured current noise to the change in I_s caused by a change in N_d of one, is $\delta q_d \cong 1.2 \times 10^{-4} e/\sqrt{\mathrm{Hz}}$ at a frequency ~ 1 Hz, about an order of magnitude better than obtained previously [25, 98]. This achievement is primarily due to the improved SET-dot coupling in our vertical configuration. On the other

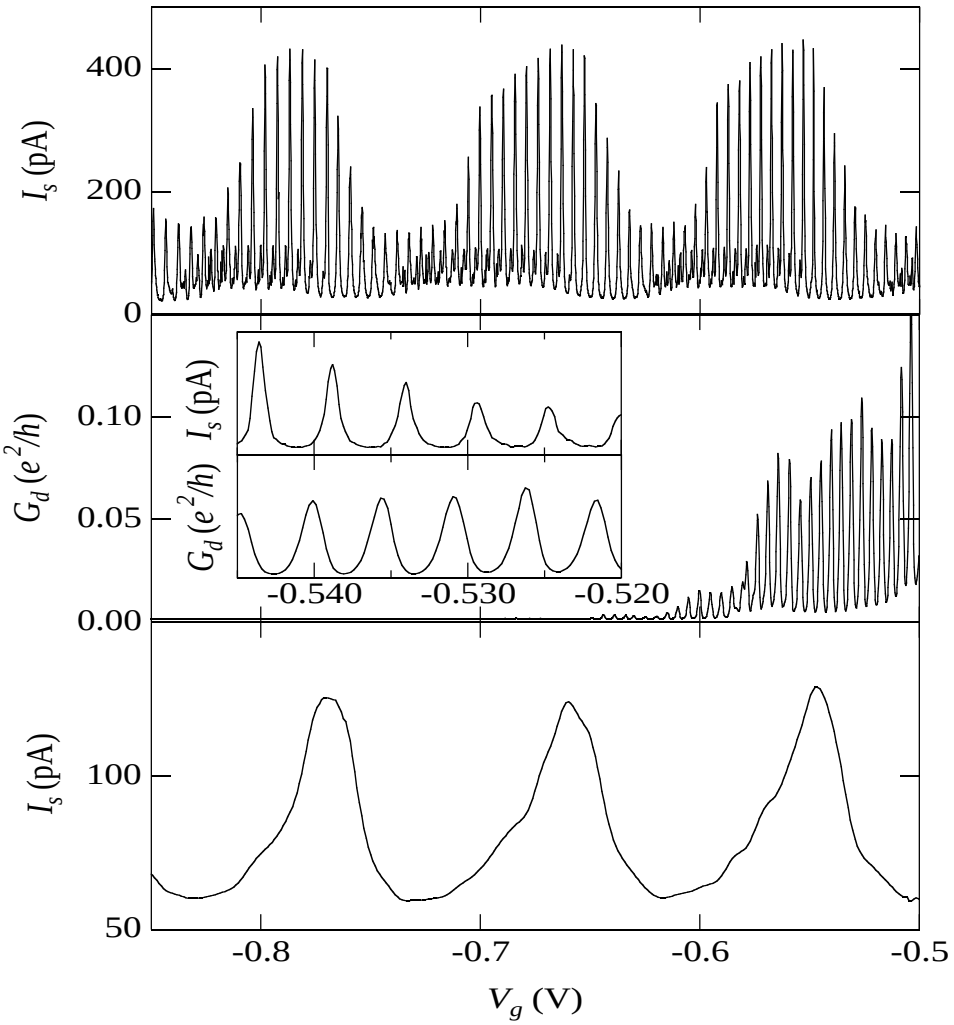

Figure 5.8: (a) Current through the SET at $V_{bias} = 810$ μV, illustrating two oscillation periods. (b) Zero-bias conductance through the dot, showing simple Coulomb oscillations. A phase shift is visible at $V_g \approx -0.58$ V, when N_s changes by one. The inset shows an expanded view of I_s and G_d around -0.53 V. (c) Current through the SET at the same bias voltage when the dot is not formed. The different scales in (a) and (c) are caused by a change in the charging energy of the SET with and without the dot.

hand, the theoretical limit for the intrinsic charge sensitivity of the SET is $\delta q = 1.2 \times 10^{-6}\ e/\sqrt{\text{Hz}}$, which corresponds to a sensitivity to the dot charge $\delta q_d \cong 2.7 \times 10^{-6}\ e/\sqrt{\text{Hz}}$. The reduced charge sensitivity in our system is mainly caused by the $1/f$ noise at the low frequencies at which the measurement is taken. Recently, a technique in which the SET is embedded in an RF resonant circuit (the RF-SET technique) was developed by Schoelkopf *et al.* [32]. Here the measurement is made at a frequency $f \sim 1\,\text{GHz}$ and the $1/f$ noise is negligible. Furthermore, high bandwidth ($\sim$ 100 MHz) has also been obtained on an RF-SET. Our system would be well suited for monitoring charge motion in the quantum dot in real time by using the RF-SET technique, a topic we will discuss in much more detail in the next chapter. As an example, for a fully optimized sample [32, 99], we would expect a sensitivity of $4 \times 10^{-6}\ e/\sqrt{\text{Hz}}$ referred to the dot charge, giving a charge noise of $0.05e$ in a 100 MHz bandwidth.

As V_g increases, the effective voltage V_{qpc} on the side gates used to form the QPCs also changes due to electrostatic coupling. The measured coupling between the gates gives $\Delta V_{qpc} \approx 0.05 \Delta V_g$. As a result, over a large voltage range, the QPCs will be more pinched off as V_g becomes more negative, resulting in the decrease in G_d, as shown in Fig. 3(b). In the end, the QPCs are completely pinched off ($G_{qpc} \ll e^2/h$), and G_d becomes too small to be measured. However, changes in N_d continue to capacitively cause shifts in Q_{0s}, which in turn causes oscillations in I_s, as shown in Fig. 3(a). This is a clear indication that an SET is more sensitive to N_d than direct transport measurements on the dot, as demonstrated by Duncan *et al.* [98]. A similar set-up has been used to study the line shape of the discrete charge levels in a quantum dot which is configured into a single-electron box, by studying the line shape of the oscillations induced by changes in the dot charge [25]. The persistence of the oscillations in I_s for very small G_d circumvents another obstacle for detection of individual tunneling

events: to observe such events, the lifetime τ associated with the energy levels of the dot must be greater than the inverse detector bandwidth. For a 100 MHz RF-SET a lifetime $\tau > 10^{-8}$ s is required, implying a level width $\Gamma = h/\tau < 0.4$ μeV. Such small level widths can be achieved only for very small G_d [100], for which direct transport measurements on the dot become very difficult, if not impossible.

CHAPTER 6

REAL-TIME DETECTION OF ELECTRON MOTION

In this chapter we discuss detection of electron motion in real time using the SET as a fast, ultra-sensitive electrometer with the radio-frequency single-electron transistor (RF-SET) technique. In Section 6.1, background of the RF-SET technique is introduced. Section 6.2 discusses experimental set-up and characterization of the system. In Section 6.3 we discuss detection and analysis of individual electron tunneling events in a quantum dot capacitively coupled to the RF-SET. Equilibrium properties of the dot are measured from the electron counting experiments including tunneling rate of the dot, power spectrum of the tunneling events, and occupational probabilities of charge states in the dot. Finally, in Section 6.4, we discuss non-equilibrium properties of the dot by driving a current through it and comparing the number of tunneling events directly with the measured DC current.

6.1 Radio-Frequency Single-Electron Transistor as a Fast Electrometer

6.1.1 Introduction

Since the invention of the SET in 1987 [33], much has been accomplished by incorporating an SET-based electrometer to detect charge on another mesoscopic

device [25, 98, 103]. However, much more can be learned if charge motion in such a device can be detected in real time, *i. e.*, if we can count electrons one by one as they tunnel on or off the device. Electron counting provides a more direct means of studying single-electron oscillations, electron-electron correlations and other dynamic phenomena. The internal bandwidth of an SET is limited by its RC time to be $\sim 200\,\mathrm{GHz}$, and its intrinsic charge sensitivity is limited by shot noise and is expected to be $\delta q \approx 1.2 \times 10^{-6}\ e/\sqrt{\mathrm{Hz}}$ [99]. As an example, if an effective offset charge of $0.2e$ is induced on the SET every time an electron tunnels on or off the device under test (DUT), individual tunneling events corresponding to a current through the device as high as 4 nA could be detected before the internal limit of the SET is reached. From the measurements in Sec. 5.2, a comparable coupling between the SET and the DUT (the quantum dot in our set-up) can be readily achieved in our system.

On the other hand, in a typical set-up, the wires connecting the sample to the room temperature circuit has a shunting capacitance C_w on the order of a few nF. As a result, the actual bandwidth of the system is limited to $1/RC \approx 4$ kHz for $R = 25\,\mathrm{K}\Omega$ and $C_w = 10\,\mathrm{nF}$. Another disadvantage of working at low frequencies is the increasing contribution from $1/f$ noise, which also decreases the SET charge sensitivity, as discussed in Section 5.2.

In 1998, Schoelkopf *et al.* [32] developed a new technique in which the SET is embedded in a resonant RF circuit, as illustrated in Fig. 6.1. In this set-up, one end of the SET is connected to an inductor with inductance L, which is in turn connected by a coaxial cable to the room temperature electronics. The other end of the SET is grounded directly to the cable shield. The inductor, the SET differential resistance R_d, and the stray capacitance C from the SET pad to ground form an LCR resonant circuit with a resonance frequency about 1 GHz in our system. A carrier wave at the resonance frequency is applied to the resonant circuit and the reflected RF signal is

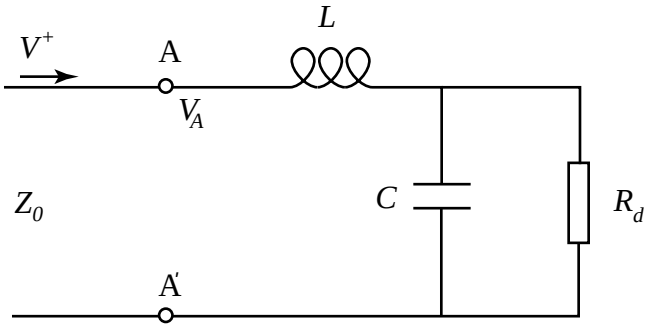

Figure 6.1: Schematic of the resonant circuit. The SET is represented by its differential resistance R_d. Z_0 is the characteristic impedance of the cable. V^+ and V_A are the incoming voltage and total voltage at points AA', respectively.

monitored. The capacitance of the cable is now part of its characteristic impedance (normally 50 Ω) and no longer limits the SET bandwidth. Changes in the SET offset charge will cause its differential resistance R_d to change, thereby changing the damping in the RF circuit. As a result, the reflection coefficient of the RF circuit and the amplitude of the reflected signal change accordingly with the SET offset charge. This change, after being amplified, is detected and used to monitor the SET charge.

6.1.2 Principles

LCR Resonant Circuit

Consider the LCR circuit in Fig. 6.1. The input impedance for the resonator looking into AA′ is

$$\begin{aligned} Z &= i\omega L + \frac{1}{i\omega C + R_d^{-1}} \\ &= \frac{R_d}{1+\omega^2 C^2 R_d^2} + i\frac{\omega L - \omega C R_d (1-\omega^2 LC) R_d}{1+\omega^2 C^2 R_d^2} \end{aligned} \tag{6.1}$$

By definition, resonance occurs when the average stored magnetic and electric

energies are equal. In other words, the imaginary part of Z equals zero at the resonant frequency ω_0:

$$\frac{\omega_0 L - \omega_0 C R_d (1 - \omega_0^2 LC) R_d}{1 + \omega_0^2 C^2 R_d^2} = 0 \tag{6.2}$$

which gives

$$\omega_0 = \sqrt{\frac{1}{LC}} \sqrt{1 - \frac{L/C}{R_d^2}} \tag{6.3}$$

Substituting ω_0 in Eq. 6.3 into Eq. 6.1, we find that the input impedance of the resonator at resonant frequency is given by

$$Z = \frac{L}{CR_d} \tag{6.4}$$

with no approximation involved.

In practice, for values of relevant L,C, and ω, $L/C \ll R_d^2$. Later we will see that this inequality is valid even in the ideal case of perfect matching. Eq. 6.3 can then be simplified to

$$\omega_0 = \sqrt{\frac{1}{LC}} \tag{6.5}$$

which we will use to calculate ω_0 from here on.

It is also convenient to define

$$Q_0 = \frac{\omega_0 L}{Z_0} = \sqrt{\frac{L}{C}} / Z_0 \tag{6.6}$$

where $Z_0 = 50\Omega$ is the characteristic impedance of the coaxial cable. Q_0 has the same form as the "external Q" [81] of a loaded series circuit, but later we will see that it is Q_0, rather than the total quality factor of the resonant circuit, that determines the performance of the RF-SET.

The reflection coefficient at AA$'$ is now

$$\Gamma \equiv \frac{V^-}{V^+} = \frac{Z - Z_0}{Z + Z_0} = -1 + \frac{2Z}{Z + Z_0} \tag{6.7}$$

Substituting Eq. 6.4 into Eq. 6.7, we get

$$\Gamma = -1 + \frac{2}{1 + Q_0^2 \frac{Z_0}{R_d}} Q_0^2 \frac{Z_0}{R_d} \tag{6.8}$$

where Q_0 is defined in Eq. 6.6.

From Eq. 6.8, it is clear that when

$$Q_0^2 \frac{Z_0}{R_d} = 1, \tag{6.9}$$

$\Gamma = 0$, *i. e.*, perfect matching is achieved. In this case, from the definition of Q_0 and ω_0, we get $L/C = Z_0 R_d$, which is still small compared to R_d^2 since $Z_0 = 50$ Omega while $R_d \sim 50\,\mathrm{K}\Omega$.

At resonance, the voltage on the SET V_d is

$$V_d = \left(\frac{1}{i\omega_0 C + 1/R_d} / \frac{L}{CR_d} \right) V_A \tag{6.10}$$

Using the inequality $L/C \ll R_d^2$, we get

$$|V_d| = (1/Q_0) \frac{R_d}{Z_0} V_A \tag{6.11}$$

Since $V_A = V^+ + V^- = V^+(1 + \Gamma)$, using the result of Eq. 6.8, we get

$$V_d = \frac{2}{1 + Q_0^2 \frac{Z_0}{R_d}} Q_0 V^+ \tag{6.12}$$

and

$$V^+ = \frac{1 + Q_0^2 \frac{Z_0}{R_d}}{2} Q_0^{-1} V_d \tag{6.13}$$

In general, the maximum voltage V_C that can be applied across the SET is limited by its internal properties and is roughly E_C/e. Eq. 6.13 demonstrates that the maximum input voltage for the resonant circuit is reduced by a factor close to Q_0.

Now suppose the sample is optimally biased, $V_d = V_C$. From Eq. 6.8 and Eq. 6.13, the voltage of the reflected wave is:

$$\begin{aligned} V^- &= V^+ \Gamma \\ &= Q_0 \frac{Z_0}{R_d} V_C + \text{constant} \end{aligned} \tag{6.14}$$

The amplitude of V^- is directly related to the resistance of the SET R_d and hence its offset charge Q. Changes in the SET offset charge thus modulates the amplitude of V^-. As a result, information about the offset charge of the SET can be determined after demodulation of the reflected wave.

Consider now the case in which there is no resonant circuit. The cable is then terminated directly by the SET, so that

$$\Gamma \equiv \frac{V^-}{V^+} = \frac{R_d - Z_0}{R_d + Z_0} \approx 1 - \frac{2Z_0}{R_d} \tag{6.15}$$

and

$$V_d = V^+ + V^- = V^+(1 + \Gamma) \approx 2V^+ \tag{6.16}$$

Again considering the optimally biased condition $V_d = V_C$, we obtain

$$V^- = V^+\Gamma_1 = -\frac{Z_0}{R_d}V_C + \text{constant} \tag{6.17}$$

Comparing Eq. 6.14 and Eq. 6.17, the presence of the LCR circuit increases the voltage of the reflected signal by a factor Q_0. From Eq. 6.9, at perfect matching, $Q_0 = \sqrt{R_d/Z_0} \approx 33$ for $Z_0 = 50\,\Omega$ and $R_d = 50\,\text{K}\Omega$. This gain is one of the most important reasons that make the RF-SET so fascinating.

The current of the reflected signal is $I^- = V^-/Z_0$. From Eq. 6.14, in the optimally-biased case,

$$I^- = Q_0 I_{\text{SET}} + \text{constant} \tag{6.18}$$

where $I_{\text{SET}} = V_C/R_d$ is the current through the SET. As a result, the shot noise power $P_I = 2eI_{\text{SET}}$ will also be amplified by a factor Q_0 in the reflected signal in the LCR resonant circuit.

Finally, the internal quality factor Q_i for the LCR resonator can be calculated to be

$$Q_i = \frac{R_d}{\omega_0 L} \tag{6.19}$$

and the so called "loaded Q" is

$$Q_L^{-1} = Q_i^{-1} + Q_0^{-1} \tag{6.20}$$

Neither Q_i nor Q_L is the gain Q_0 in Eq. 6.14, and simulations also show that the bandwidth of the resonance is roughly $\omega_0/2\pi Q_0$, instead of $\omega_0/2\pi Q_L$. It therefore seems misleading to think about the "quality factor" of the circuit when considering the properties of the RF-SET.

Effects of Loss in The RF-SET

In the previous discussion, all components are treated as ideal. In a real system, however, there are always losses in the system, including losses in the inductor, the contact resistance to the sample pad, and shunting resistance in the capacitor. Since the sample resistance R_d is about 50 kΩ, the contact resistance to the sample pad can normally be neglected. The measurement is performed at low temperature and in vacuum, so that the shunting of the capacitor can also be neglected. However, from Eq. 6.4, at resonance, the impedance of an RF-SET at resonance is typically only a few Ohms, which makes any loss between the inductor and the coaxial cable extremely important. For example, a commercial inductor (*e. g.*, by Coilcraft) may have a low resistance $\sim 1\,\Omega$ at DC, however, that resistance might become $10\,\Omega$ at 1 GHz due to the skin effect. The same is true for the solder joint between the coaxial cable and the inductor. Eddy currents in the inductor and metal close to it will also add loss to the system, which might be important if we try to match the resonator to the cable.

All of the relevant loss terms can by modelled by adding a resistor in between the inductor and the cable in Fig. 6.1, as illustrated in Fig. 6.2.

As a result, the impedance looking into AA$'$ can be easily calculated by adding

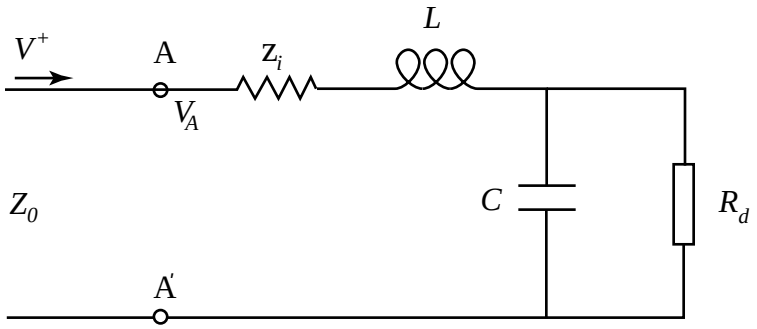

Figure 6.2: Schematic of the resonant circuit with the loss modelled by a resistance Z_i.

Z_i to Eq. 6.1. The resonant condition is not changed by the addition of Z_i, and ω_0 is still defined by Eq. 6.3 and Eq. 6.5. At resonance we get

$$Z = Z_i + \frac{L}{CR_d} \tag{6.21}$$

and

$$\Gamma = -1 + \frac{2\frac{Z_i}{Z_0} + 2Q_0^2\frac{Z_0}{R_d}}{\frac{Z_i}{Z_0} + Q_0^2\frac{Z_0}{R_d} + 1} \tag{6.22}$$

where Q_0 is defined in Eq. 6.6.

From Eq. 6.22, a dip will appear in Γ even when the SET is in the Coulomb blockade and $R_d \sim \infty$. When

$$\frac{Z_i}{Z_0} + Q_0^2\frac{Z_0}{R_d} = 1 \tag{6.23}$$

$\Gamma = 0$ and the system appears perfectly matched. However, the signal gain will be reduced compared with the ideal case.

The "loaded Q" of this resonant circuit is

$$Q_L^{-1} = Q_i^{-1} + Q_z^{-1} + Q_0^{-1} \tag{6.24}$$

where $Q_z = \omega_0 L/Z_i$ corresponds the reduction of the quality factor due to additional loss from Z_i.

On the other hand, our simulations show that the bandwidth of the resonance does not change due to the addition of Z_i as long as $Z_i < 50\,\Omega$. This once again demonstrates that the loaded Q is not a good measure of RF-SET performance. When $Z_i > 50\,\Omega$, a perfect match is no longer possible and the resonant dip will be broadened.

Fig. 6.3 shows simulated $|\Gamma|$ as a function of frequency for the ideal case and with an extra loss, for both $R_d \sim \infty$ and $R_d = 50\,\mathrm{k}\Omega$. In the simulation, we have used $C = 0.3\,\mathrm{pF}, L = 100\,\mathrm{nH}$ and $Z_0 = 50\,\Omega$.

Demodulation of the Signal

When properly biased, offset charge changes in the SET will change the SET resistance R_d, which in turn modulates the amplitude of the reflected signal. Following Pozar [81], the modulated signal can be written in the form

$$v(t) = v_0(1 + m\cos\omega_m t)\cos\omega_0 t \tag{6.25}$$

where ω_m is the modulation frequency, ω_0 is the RF carrier frequency ($\omega_0 \gg \omega_m$), and m is defined as the modulation index ($0 \leq m \leq 1$). In the RF-SET, comparing Eq. 6.25 with Eq. 6.14, we get $m = Q_0 A$, where A relates the change in offset charge to changes in R_d, and ω_m is the frequency of the signal of interest which causes the offset charge oscillation.

The useful information at ω_m can be obtained by using a mixer to demodulate $v(t)$. A mixer has a local oscillator (LO) port, an RF port, and it produces an output proportional to the product of the LO and RF signals. If we connect the modulated signal to the RF port, and a signal at the carrier frequency $v_l(t) = v_1\cos(\omega_0 t + \phi)$ to the LO port, from trigonometric relations, we easily obtain for the output signal

$$v_{\mathrm{out}} \;=\; v(t) \times v_l(t)$$

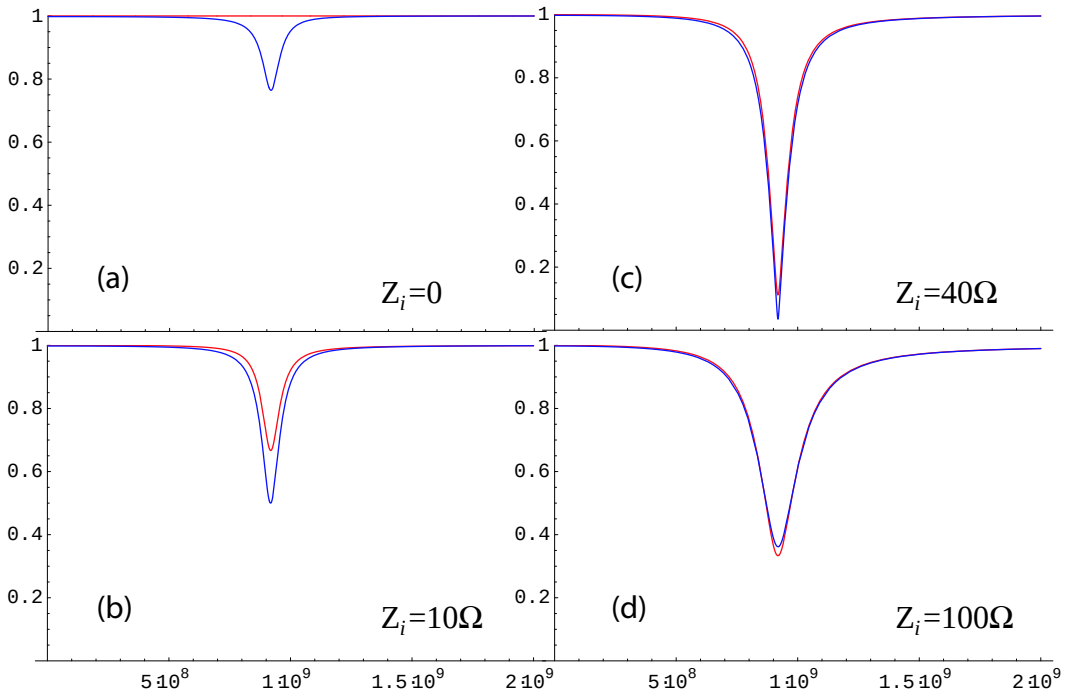

Figure 6.3: Simulation of $|\Gamma|$ as a function of frequency for (a) no extra loss (b) $Z_i = 10\,\Omega$ (c) $Z_i = 40\,\Omega$ and (d) $Z_i = 100\,\Omega$. The red lines represent the SET in blockade case, *i. e.*, the SET resistance $R_d \sim \infty$, and blue lines represent $R_d = 50\,\mathrm{k}\Omega$. The resonant frequency is not changed by the addition of Z_i. The bandwidth of the resonance does not change until $Z_i > 50\,\Omega$, in which case a crossover between the red and blue lines also occurs.

$$= \frac{v_0 v_l}{2}\cos(2\omega_0 t+\phi)(1+m\cos(\omega_m t)) + \frac{v_0 v_l}{2}\cos\phi + \frac{v_0 v_l}{2} m\cos\phi\cos\omega_m t \quad (6.26)$$

Normally, a low-pass filter is used to remove the components at frequencies around $2\omega_0$. The resulting output, usually termed the "intermediate frequency" (IF) signal, then consists of a term at the signal frequency ω_m with an amplitude proportional to m, and a DC term. In order to achieve maximum signal size, it is usually necessary to tune the phase of the LO so that $\phi = n\pi$ in Eq. 6.26, where n is an integer.

6.2 Experimental Setup

6.2.1 Sample Design

The first sample was measured using the same design as illustrated in Fig. 4.6. However, in such a design, the RF signal must travel through the two QPC regions before it is reflected. The SET leads and 2DEG form transmission lines, and when the two QPCs are formed the size of the reflected signal is reduced by more than a factor of 2. Another disadvantage of such a design is that to prevent effects of the "third junction" in the middle of the SET from appearing, its area must be much larger than that of the tunnel junctions. This requirement in turn prevents the formation of smaller dots in which more interesting phenomena such as discrete energy levels and the Kondo effect can modify tunneling rates.

An improved design illustrated in Fig. 6.4 is used instead in later measurements. The junctions of the SET are again formed by the overlap of the two shadows. However, since now the RF path does not run through the QPCs, the size of the reflected signal is less affected by the formation of the dot. Furthermore, the "third junction" on the right only affects the coupling between the SET and the dot, so that there is

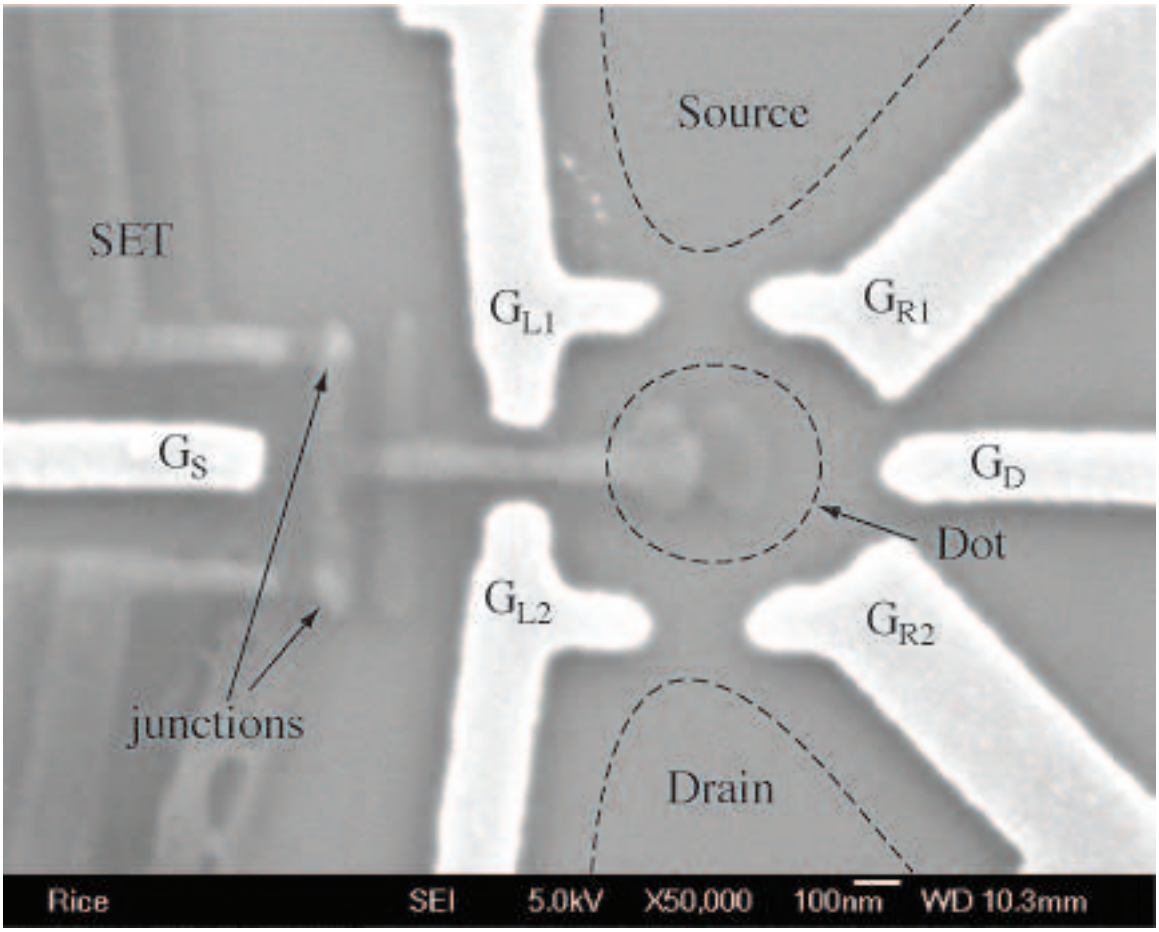

Figure 6.4: Electron micrograph of a sample based on the new design, with the dot schematically illustrated. Gates G_{L1}, G_{R1} form one point contact while G_{L2} and G_{R2} form the other. Gate G_d is used to control the dot offset charge.

no limit on the size of the dot as long as the SET-dot coupling is strong enough.

Our tests have shown that the SET response saturates for offset charge changes $\Delta q \approx 0.2e$. From Eq. 5.7, when an electron tunnels into or out of the dot, it will effectively change the SET charge by

$$\Delta q = (C_c/C_{\rm dot})e \tag{6.27}$$

where C_c is the coupling capacitance between the SET and the dot, and $C_{\rm dot}$ is the total dot capacitance including the tunneling capacitances, the gate capacitances and C_c. For a typical value $C_{\rm dot} = 300\,{\rm aF}$, $\Delta q = 0.2e$ requires $C_c = 60\,{\rm aF}$, which can still be achieved with the new design.

The sample fabrication procedures are:

1. Exposure of the etched pattern.

2. Chemical etching.

3. Alloying Ohmic contacts to the 2DEG.

4. Fabrication of the Au gates and leads, together with a set of alignment marks. These alignment marks will be used to align the SET to the Au gates.

5. Fabrication of the SET.

The initial alignment in all these steps is performed by the "scratch mark" technique.

As shown in Fig. 6.4, Gates G_{L1}, G_{R1} form one point contact while G_{L2} and G_{R2} form the other. Gate G_d is used to control the dot offset charge and gate G_s can be used to adjust the SET offset charge to achieve optimal gain. For the dot to form well, the channel between gates G_{L1} and G_{L2} must be closed. To achieve this goal, the gap between these two gates is narrower and longer than the ones forming the point

Table 6.1: Properties of samples S3–S6, where R_n and E_C are the normal-state resistance and charging energy of the SET, respectively. f_C is the frequency at which maximum gain is achieved on the RF-SET. δq is measured charge sensitivity with a $0.05e$ offset charge excitation for an unconfined 2DEG. 2DEG substrate for sampless S3 and S4 was provided by Dr. Gossard at UC Santa Barbara with 2DEG located 50 nm below surface, while the substrate for samples S5 and S6 was provided by Dr. Pfeiffer at Bell Labs with 2DEG located 190 nm below surface.

sample	f_C (MHz)	R_n (KΩ)	E_C	δq ($e/\sqrt{\text{Hz}}$)	DC dot behavior
S3	1003	47	152 μeV	2×10^{-5}	good
S4	1006	39	143 μeV	4×10^{-5}	good
S5	1097	25	162 μeV	1.3×10^{-5}	poor
S6	1091	15	160 μeV	2×10^{-5}	good

contacts. On the other hand, since these gates are very close to the SET, adding a large voltage will cause the SET to "arc" to the gates. In practice, a reduced voltage V_L is applied to gates G_{L1} and G_{L2}, while voltages V_1 on G_{R1} and V_2 on G_{R2} are adjusted to pinch the point contacts to a desired level.

Four samples based on the design as shown in Fig. 6.4 have been measured. The properties of them are listed in Table 6.1.

6.2.2 RF Set-Up

Fig. 6.5 schematically illustrates the set-up of the RF-SET circuit. The SET, the inductor, and the stray capacitance of the SET pad to ground form the LCR resonant circuit discussed in the last section. From Eq. 6.6 and Eq. 6.5, in order to increase the system gain Q_0 at a fixed resonant frequency ω_0, C should be kept minimal while

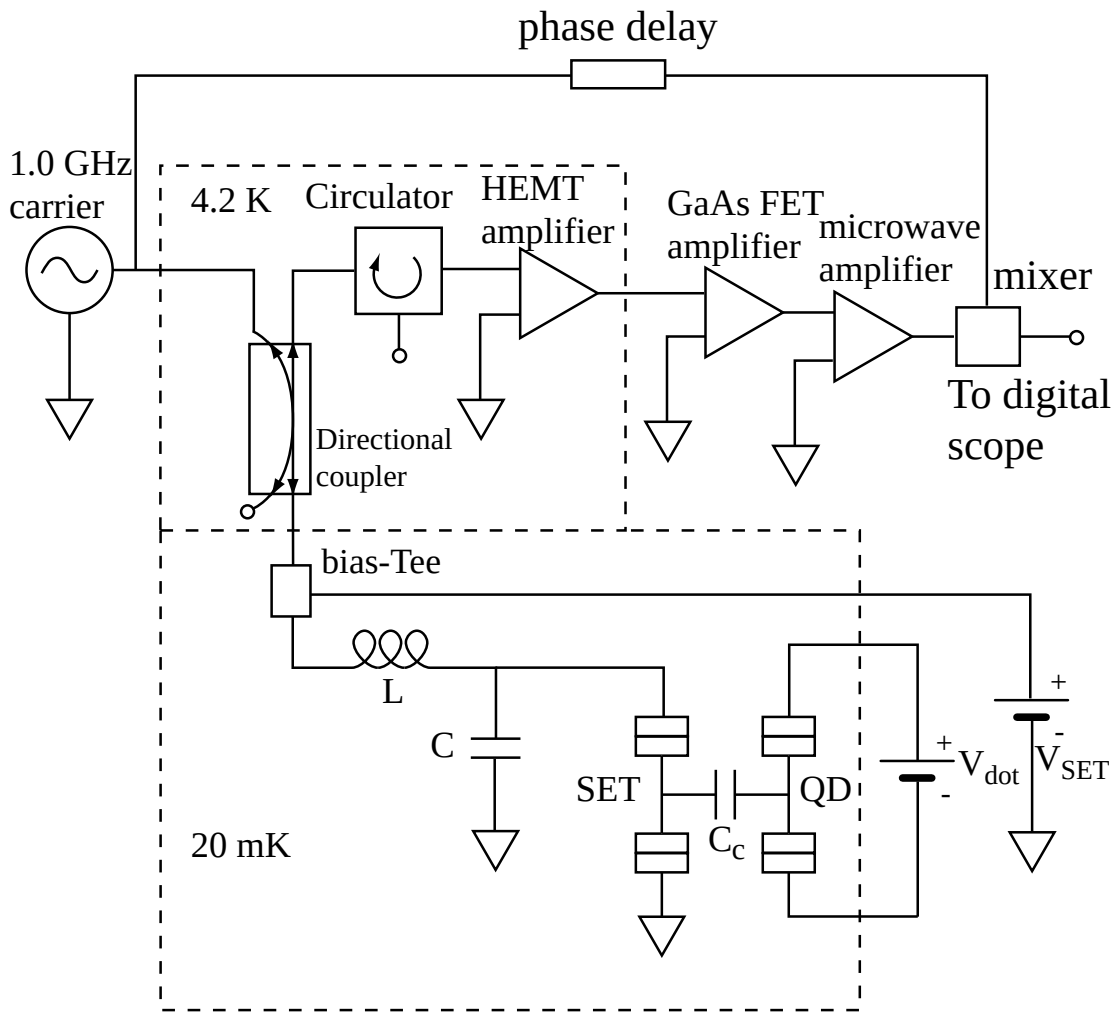

Figure 6.5: Schematic of the RF-SET circuit. Showing the various devices used at different temperatures.

L should be increased accordingly.

In practice C is the stray capacitance from the inductor and sample pads to ground. In order to keep stray capacitance from the inductor to ground small, the inductor is secured on a piece of sapphire so that the distance between the inductor and the metallic walls of the sample holder is several times larger than the inductor itself. As discussed in Sec. 3.4, the 2DEG under the SET pads and large leads is etched away to reduce capacitance caused by coupling to the 2DEG. On the other hand, defects in the 2DEG will tend to leave stray electrons close to the surface resulting in either a large stray capacitance or a loss in the RF circuit. In either case, the resonance will be completely washed away. We have found out that 2DEG material fabricated shortly after the MBE machine is closed are likely to have more defects and not suitable for the RF-SET measurements. To reduce such risks, the central leads left over the 2DEG should also be made as narrow as possible. After all these measures, a C on the order of 0.2 pF has been achieved in our system, which is limited by the self capacitance of the finite size of the pads and wires.

Two kinds of 0603 (1608) type commercial inductors with nominal inductance about 87nH made by Panasonic (Non-winding design) and Coilcraft (Winding design) have been used and similar results have been achieved on both. The self-resonant frequency of those inductors is not much higher than the carrier wave frequency ≈ 1 GHz, so that the actual inductance is always somewhat higher than the nominal value. The main problem with those inductors is that they are lossy. Although the DC resistance is normally around 1 Ω, the effective resistance at 1 GHz is much larger due to the skin effect, which in turn affects the performance of the matching network as discussed in Sec. 6.1.2.

We have also tried to reduce the loss by winding a length of fine multifilament superconducting wire (Supercon Wire, 54S43, 0.045" dia, Cu:SC=1.3:1) on a piece

of fused quartz core (Goodfellow, S1617910, 1.0 mm dia). Typically, 8 windings correspond to about 100 nH. This type of wire is also widely used to make superconducting magnets since pure niobium is hard to solder to. Good inductor like behavior is achieved on these home-made coils. However, the inductor loss is still not eliminated. Although the wire is superconduting at DC, the alternating RF signal likely causes eddy current in the Cu part of the wire. The eddy current loss is again made worse due to the skin effect at the relevant frequency. The best solution to this problem is to use a superconducting Nb on-chip inductor while avoiding normal metal completely.

Another possible source of loss comes from that fact that the central part of the SET is still coupled to the 2DEG, and the impedance seen by the circuit is the combination of R_d and the SET leads/2DEG transmission line impedance. As a result, the signal may not be completely reflected even when $R_d \sim \infty$. However, no improvement in the reflected signal was observed on samples for which the 2DEG under the SET was completely etched away. Such a result suggests that the loss was not caused by the 2DEG.

The reflected signal, passing through the directional coupler, is then amplified at $T \approx 4$K by a cryogenic amplifier (Berkshire Technologies, Model L-1.0-20H) anchored inside the IVC of the fridge. The signal is further amplified by a GaAs FET amplifier (Mitek, Model AFS3) and another microwave amplifier (Minicircuits, Model ZEL-0812LN) at room temperature. The signal is then de-modulated by the mixer and recorded by a fast digital oscilloscope (Techtronix, Model TDS7054). Table 6.2 lists the gain, input bandwidth, and estimated noise temperature T_n of these amplifiers.

Due to its large gain, the system noise is dominated by the input noise of the cold amplifier. To determine the noise temperature of the cold amplifier, the total noise after it and the FET amplifier is measured first on a spectrum analyzer (Agilent

Table 6.2: Parameters for the various amplifiers used in the RF-SET measurement. The noise temperature T_n for the cold amplifier is estimated as described in the text. T_n for the other amplifiers are obtained from manufacture specifications.

Amplifier	input frequency range (MHz)	gain (dB)	T_n (Kelvin)
cryogenic HEMT	800–1200	28.3	2.5
GaAs FET	800–1200	44.4	60
microwave	800–1200	30	120

Technologies, E4408B) at the relevant frequency without any input. For example, the noise power at 1 GHz is ≈ -61.8 dBm with a 3 MHz resolution bandwidth. According to the spectrum analyzer manual, the noise power of an actual 3 MHz bandwidth is roughly 2 dB higher due to the type of filtering used. After taking into account the gains of the amplifiers, the noise of the FET amplifier, and the loss ($\approx$ 3 dB) in the semi-rigid coaxial cable, the estimated noise temperature of the cold amplifier is calculated to 2.5 K. This value is lower than the specified value (4 K), which is obtained at $T = 16$ K, due to the fact that the cold amplifier is thermally anchored to a colder ($T \approx 4$ K) reservoir in our system. The effective total system noise seen at the input of the cold amplifier, including the FET amplifier noise, is about 2.7 K.

Fig. 6.6 shows a photo of the fridge insert, highlighting the various components used in the RF-SET measurement.

6.2.3 Characterization of the RF-SET

In order to find out the resonance frequency of the system, the input carrier wave is 100% amplitude-modulated at 1 KHz, and the frequency is swept across a broad frequency range. A diode is used instead of the mixer to demodulate the

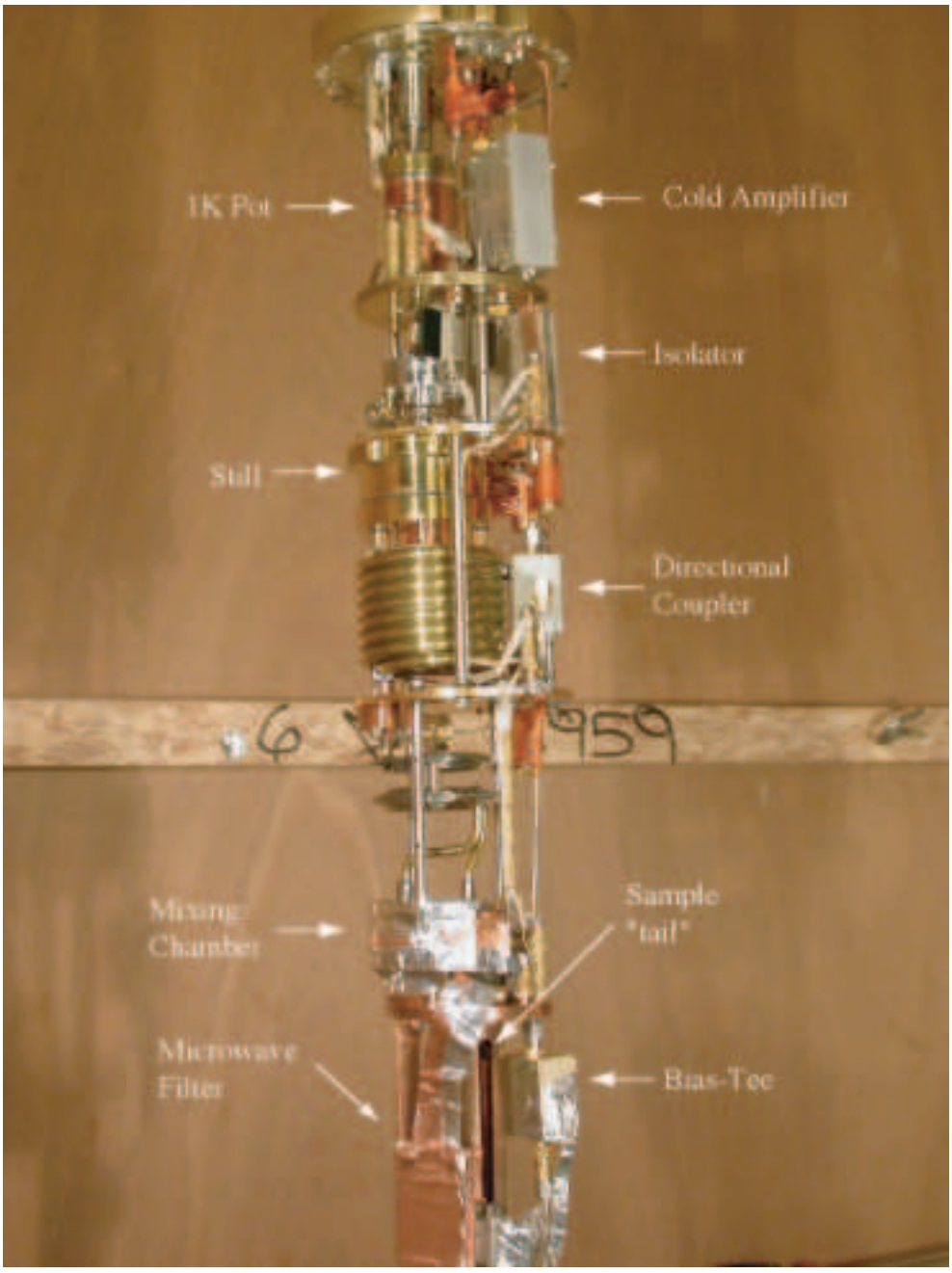

Figure 6.6: Photo of the insert, showing the various components used in the RF-SET measurement.

reflected signal, so that no phase compensation is required. The output signal at the modulation frequency is proportional to the power of the modulation signal [81], in this case, the power of the reflected signal. This signal can then be easily recorded by a lock-in amplifier. Two frequency sweeps corresponding to the two limiting cases of the SET resistance R_d are performed and the results are compared. In one frequency sweep, the SET is biased in the center of the superconducting gap, *i. e.* $R_d \sim \infty$; in the other sweep, the SET is biased by a large voltage $\sim 6.7\,\mathrm{mV}$ such that $R_d = R_n$ where R_n on the order of $50\,\mathrm{K}\Omega$ is the normal state resistance of the SET.

Fig. 6.7(a) shows the results for sample S4 listed in Table 6.1. A dip appears around the resonant frequency even in the case $R_d \sim \infty$, indicating there are losses in the system, as discussed in Sec. 6.2.2. The maximum change in reflected power occurs at $f = 1003\,\mathrm{MHz}$, corresponding to a gain $G \approx 11$, away from the resonant frequency $f_0 = 1025\,\mathrm{MHz}$. In Fig. 6.7(b), we show the power of the shot noise of the reflected signal and a fit based on a Gaussian function. The fit gives $f_0 = 1025\,\mathrm{MHz}$, and FWHM $\Delta f = 66.6\,\mathrm{MHz}$. Together with the simulation discussed in Sec. 6.1.2, we get $L \approx 140\,\mathrm{nH}$, $C \approx 0.17\,\mathrm{pF}$, and $Q_0 \approx 18$. By removing the losses and operating at the resonant frequency, the signal-to-noise ratio will be enhanced by almost by a factor of two.

The next step is to find the optimal DC bias V_{dc} and the optimal amplitude of the RF signal V_{rf} that can be applied on the SET. If the SET is in the normal state, the answer is straightforward $V_{\mathrm{dc}} = 0$ and $V_{\mathrm{rf}} = E_C/e$. When the SET is in the superconducting state, we have found out that when $R_n \approx 25\,\mathrm{K}\Omega$, there is a large linear response region formed by the $3e$ peak and the JQP peak, as illustrated in Fig. 6.8 for sample S5. As a result, V_{dc} is set to be in between the $3e$ peak and the JQP peak, and $V_{\mathrm{rf}} \approx 220\ \mu\mathrm{V} = 1.4\ E_C/e$ for S5. In practice, V_{dc} and V_{rf} are determined empirically by gradually increasing the RF signal until the modulation signal starts

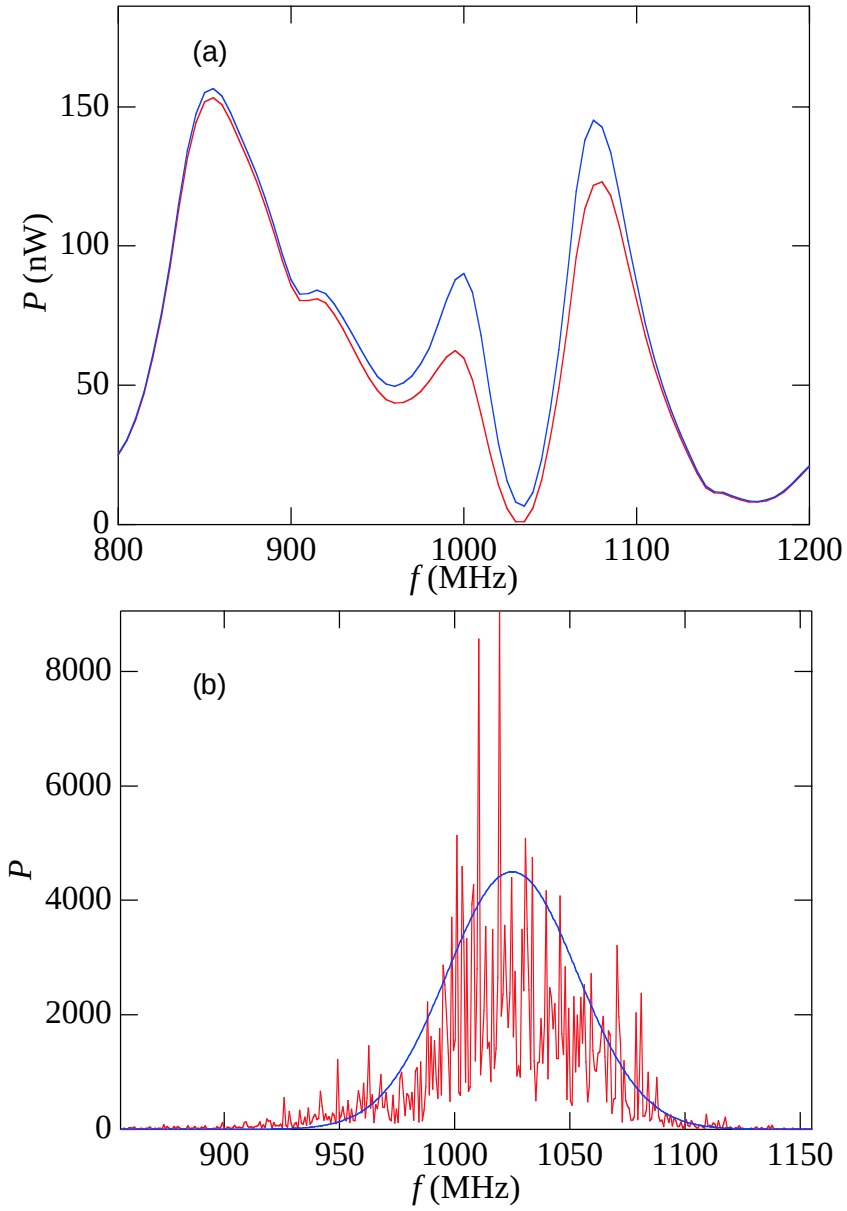

Figure 6.7: (a) Power of the reflected signal for sample S4 as a function of frequency for $R_d \sim \infty$ (blue) and $R_d = 39\,\mathrm{K}\Omega$ (red). (b) Shot noise power in the reflected signal. The red curve is taken as the difference of the shot noise power measured at $I_{\mathrm{SET}} = 8\,\mu\mathrm{A}$ and $I_{\mathrm{SET}} = 1\,\mu\mathrm{A}$, and the blue curve is a fit which gives $\omega_0 = 1025\,\mathrm{MHz}$.

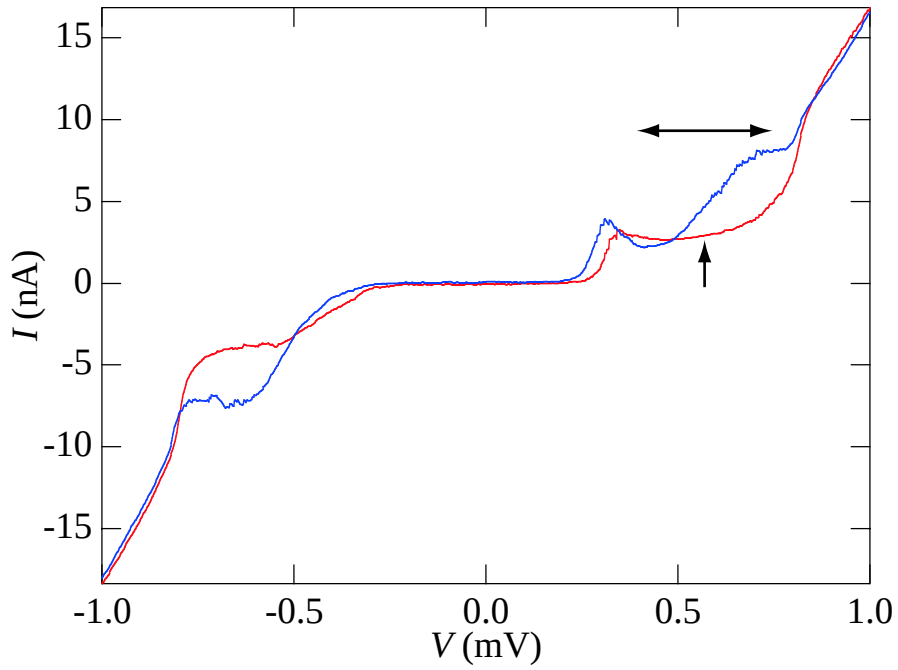

Figure 6.8: Representative I-V curves for sample S5 with $R_n = 25\,\mathrm{K}\Omega$. The optimal working point is between the $3e$ peak and the JQP peak as indicated by the arrow. The optimal size of the carrier wave is also illustrated.

to get washed out, and they do not seem to show a really sharp response once within certain range of the the optimal values. For S5, we found that the maximum charge sensitivity is achieved when the input power is $-66\,\mathrm{dBm}$. After taking into account the 3 dB loss in the cable, the 20 dB attenuation in the directional coupler, and the gain G of 11, it corresponds to an RF voltage $V_{\mathrm{rf}} \approx 110\ \mu$Vrms ($310\,\mu$V peak-to-peak) on the SET, in good agreement with estimates based on the size of the linear response region in Fig. 6.8.

Once the optimal values of f, V_{dc} and V_{rf} are determined, we can calculate the charge sensitivity of the RF-SET by applying a small AC wiggle to one of the SET gates to create an oscillating offset charge on the SET. As discussed in Sec. 6.1.2,

this offset charge oscillation will modulate the reflected RF signal and appear as side peaks on the power spectrum around the main carrier wave peak. Fig. 6.9(a) shows such a spectral measurement performed sample S6 when the 2DEG is unconfined with a 100 KHz sine wave excition on one of the SET gates corresponding to an offset charge oscillation of $0.05e$ rms. From the signal-to-noise ratio (SNR) of the peaks, the acquisition bandwidth B, and the size of the offset charge oscillation Δq, we can calculate the charge sensitivity

$$\delta q = \frac{\Delta q}{\sqrt{B} 10^{\mathrm{SNR}/20}}. \tag{6.28}$$

Data in Fig. 6.9(a) gives $\delta q \approx 2.0 \times 10^{-5} e/\sqrt{\mathrm{Hz}}$. A charge sensitivity $\delta q \approx 8 \times 10^{-6} e/\sqrt{\mathrm{Hz}}$ has been achieved on sample S3 with a $0.01e$ offset charge wiggle.

Fig. 6.9(b) shows the signal after demodulation by the mixer for the same offset charge excitation. A 1 MHz low-pass filter is used before the scope and no averaging is performed. The signal is clearly captured by the RF-SET, demonstrating that our system has sufficient charge sensitivity to capture small, fast offset charge changes. The charge sensitivity will be decreased by about a factor of 2 when the dot is formed, which is still sufficient to capture the signal of $\sim 0.2e$ caused by an electron tunneling on or off of the dot.

Proper grounding is very important in RF-SET measurements. Since one end of the SET, the gates, and the 2DEG are normally grounded, fluctuations in the "ground" potential will then cause the SET offset charge to fluctuate which in turn generates a noise as a modulation on the reflected signal. This noise thus cannot be eliminated by filtering afterwards. As a result, the amplifiers in the measurement circuit should have their own ground directly connected to a reservoir for which the potential is fixed so that the noise in the amplifiers will be dissipated directly to the reservoir, instead of affecting the SET ground. In our system, the bridge amplifier of

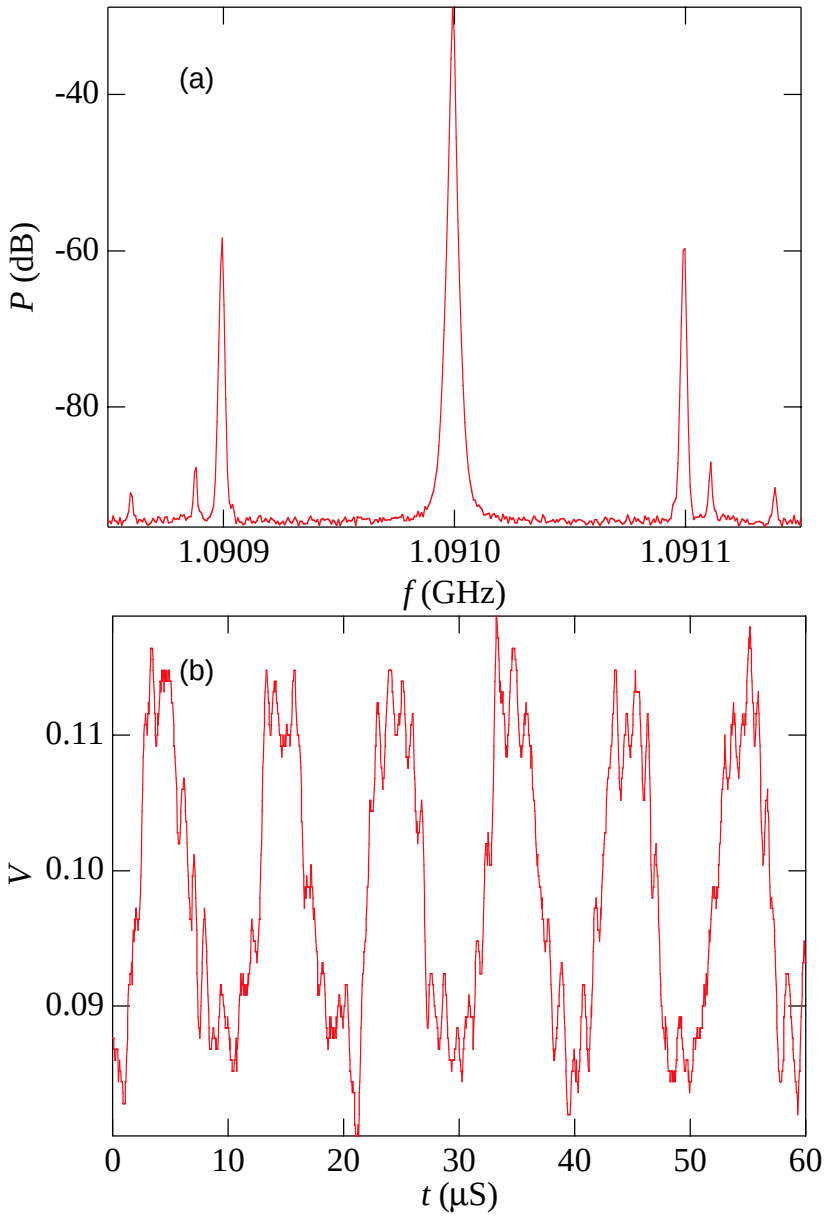

Figure 6.9: (a) Modulation of the reflected signal corresponding to a 100 KHz, 0.05e rms offset charge excitation on the SET of S6. (b) The offset charge excitation is clearly captured by the digital scope after the mixer. No averaging is performed.

the fridge used to measure the temperatures has a non-negligible noise at 28 KHz and its harmonics, which severely reducing the signal-to-noise ratio when the amplifier ground is connected to the SET ground.

6.2.4 Characterization of the Dot

DC characterization of the dot is performed again with the methods described in Sec. 5.2. In Fig. 6.10(a),(b), we plot the current of the SET and the conductance of the dot as a function of the voltage V_g on gate G_d for sample S4. Here the SET is biased in the JQP region. Once again, doubly periodic oscillations in the SET current are observed, for which the faster oscillations correspond to changes in the dot charge and the slower oscillations are caused by direct coupling from the gate. Due to static coupling between the gates, the point contacts of the dot become more and more closed as V_g is increased. As a result, the dot conductance quickly decays to zero, as illustrated in Fig. 6.10(b). On the other hand, the capacitances of the QPCs also decrease [100], resulting in a larger induced offset charge from the dot to the SET according to Eq. 6.27. As a result, the size of oscillations in the SET current caused by the induced charge increases with V_g, as can be seen from Fig. 6.10(a). In Fig. 6.10(c), we show the SET current when the dot is very closed, so that oscillations caused by the induced charge are much larger than those in Fig. 6.10(a).

Samples (S5, S6) fabricated on 200 nm deep 2DEG material manufactured by Dr. Pfiffer's group at Bell Labs have also been measured. The main concern with the 200 nm material is that the coupling between the SET and the dot may not be high enough to perform real time measurements. On the other hand, a deeper 2DEG will reduce the total capacitance of the SET and hence increase its charging energy, which in turn results in an increased charge sensitivity. In Fig. 6.10(d), we

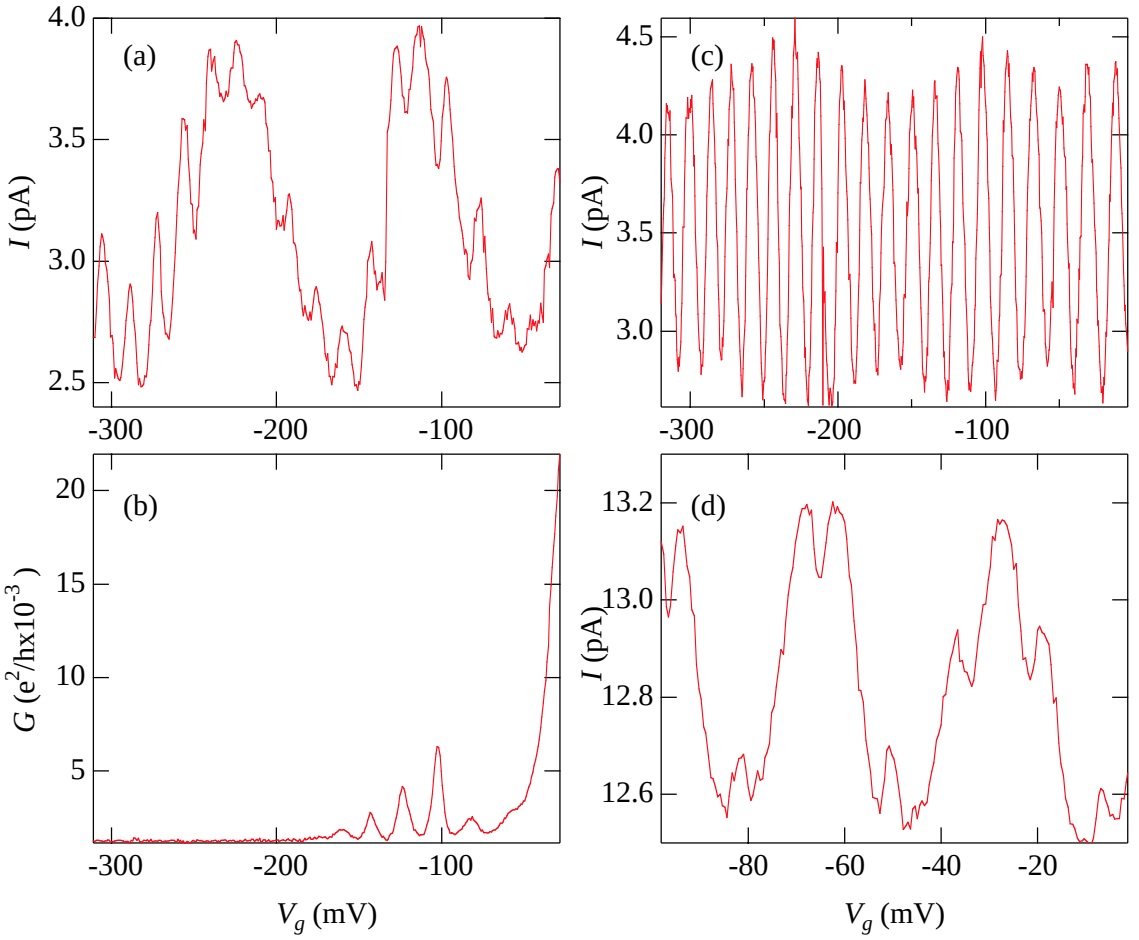

Figure 6.10: (a) Current through the SET as a function of gate voltage V_g for sample S4. The size of the oscillation caused by dot charge change increases gradually as the total capacitance of the dot decreases. (b) Conductance of the dot taken simultaneously. (c) Current through the SET when the dot is more closed. The size of oscillations caused by changes in the dot charge is much larger than that in (a). (d) Current through the SET vs. V_g for sample S6 when the dot is sufficiently closed. Oscillations caused by dot charge change are again visible.

plot the current through the SET when the dot is sufficiently closed for sample S6. Once again, oscillations corresponding to changes in the dot charge are clearly visible. From the size of the oscillations, we estimate that when an electron tunnels on or off of the dot, it changes the SET offset charge by $\Delta e \sim 0.1e$.

6.3 Real-time Results

Of the four samples listed in Table 6.1, sample S4 did not have sufficient charge sensitivity (we also had the amplifier noise problem at that time), and sample S5 did not show reasonable dot behavior since the effective dot area was smaller on the deeper 2DEG material. Sample S3 and sample S6 have shown both sufficient charge sensitivity and good dot behavior. As a result, random telegraph signal (RTS) have been observed after demodulation of the reflected RF signal on both samples when the dot is formed.

In the case of sample S3, excess electrons were unfortunately pumped from the 2DEG to traps close to the substrate surface after application of too large a negative voltage to one of the gatest. As a result, both DC Columb-blockade oscillations and RF resonance were damped out. Such a problem could normally be solved by unloading the fridge from the He bath and warming the sample to room temperature, then cooling it down again (so called "thermal cycling"). However this sample did not survive thermal cycling, due to a few problems we had in our fridge. Though many data were taken on it, a systematic study was not performed and conclusive results could not be achieved. We will therefore concentrate on results obtained from sample S6 hereafter.

6.3.1 "Change" Routine

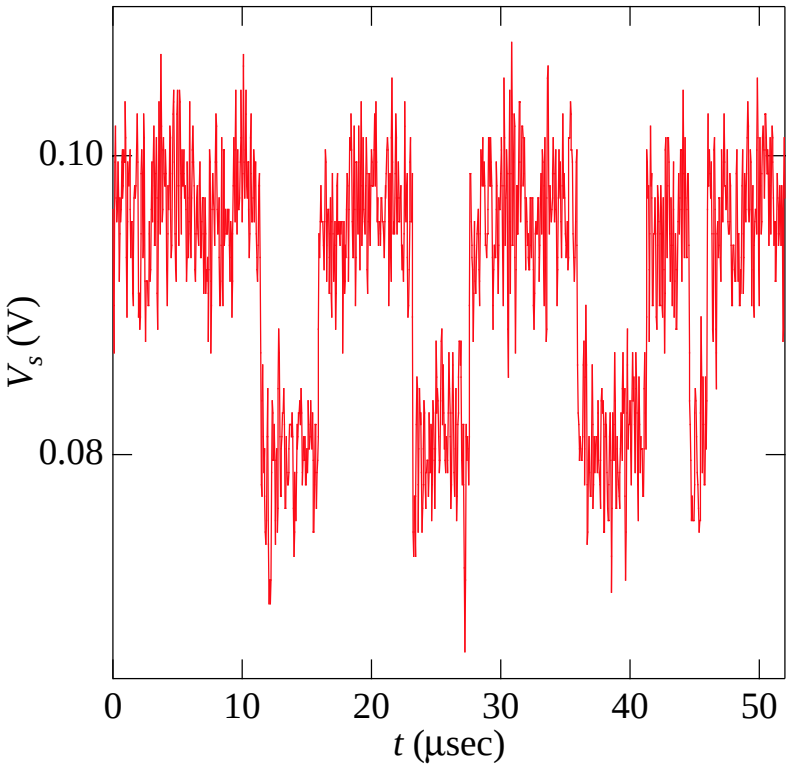

Figure 6.11: Representative switching events captured by the scope.

The best charge sensitivity for sample S6 is achieved at a DC SET bias $V_{\mathrm{SET}} \approx 500\,\mu$V, *i. e.*, between the $3e$ peak and the JQP peak. The optimal RF input power is -66 dBm, which corresponds to a voltage on SET $V_C = 87\,\mu$V rms ($247\,\mu$V peak-to-peak). Fig. 6.11 shows a typical data recorded on the Tektronics TDS7056 digital scope when the dot is formed in the 2DEG. It clearly illustrates the switchings between two states on the dot, and contains information such as the occupational time on each state and the correlation between successive switching events. Such information has significant importance in understanding the behavior of electrons in nanoscale devices, and can only be estimated indirectly previously from DC measurements. In order to

extract such information, however, we first need to correctly identify each switching event.

Similar tasks (the "change" problem) have been widely studied in digital signal processing [104] and an algorithm was developed for our problem with the help of Dr. Don. H. Johnson at Department of Electrical & Computer Engineering of Rice University.

The problem can be simplified as determining whether or not a switching event has occurred within a record $\mathbf{X}$ of N points. In another word, we want to determine which of the two hypothesis best describes the data:

$$H_0: \quad \mathbf{X} \sim p\mathbf{x}(\mathbf{x}; \theta | H_0) \tag{6.29}$$

$$H_1: \quad \mathbf{X} \sim p\mathbf{x}(\mathbf{x}; \theta | H_1) \tag{6.30}$$

Here, H_0 is the hypothesis that no change happens in $\mathbf{X}$, and H_1 is the hypothesis that a single switching event happens in $\mathbf{X}$. $p\mathbf{x}(\mathbf{x}; \theta | H_i)$ denotes the joint probability function of $\mathbf{X}$ when hypothesis i is true, and θ is a parameter vector which varies with hypothesis. Assuming the data is taken in the presence of white Gaussian noise and that the variance σ^2 is the same for both states, for hypothesis 0, (no change)

$$p\mathbf{x}(\mathbf{x}; \theta | H_0) = \prod_{n=1}^{N} \frac{1}{\sqrt{2\pi\sigma^2}} \exp\left\{ -\frac{(x_n - \mu)^2}{2\sigma^2} \right\}. \tag{6.31}$$

The parameter vector θ here just consists of the mean μ. For hypothesis 1, we assume that somewhere within the interval at point n_C, the mean of the data switches from μ_0 to μ_1.

$$p\mathbf{x}(\mathbf{x}; \theta | H_1) = \prod_{n=1}^{n_C} \frac{1}{\sqrt{2\pi\sigma^2}} \exp\left\{ -\frac{(x_n - \mu_0)^2}{2\sigma^2} \right\} \prod_{n=n_C+1}^{N} \frac{1}{\sqrt{2\pi\sigma^2}} \exp\left\{ -\frac{(x_n - \mu_1)^2}{2\sigma^2} \right\}. \tag{6.32}$$

Now the parameter vector θ consists of the two means and the change time: $\theta = (\mu_0, \mu_1, n_C)$. Note that we do not assume that the mean before the change is greater

than the mean after or vice versa.

We then perform the generalized likelihood ratio test by finding the maximum of each probability function with respect to the parameter vector, and comparing the ratio of the two maxima with a threshold to determine which hypothesis best describes the data

$$\frac{\max_\theta p\mathbf{x}(\mathbf{x};\theta|H_1)}{\max_\theta p\mathbf{x}(\mathbf{x};\theta|H_0)} \underset{H_0}{\overset{H_1}{\gtrless}} \eta. \tag{6.33}$$

Eq. 6.33 can be simplified by taking the logarithm and moving the logarithm inside the maximization operator without affecting the detector's performance.

$$\max_\theta \ln p\mathbf{x}(\mathbf{x};\theta|H_1) - \max_\theta \ln p\mathbf{x}(\mathbf{x};\theta|H_0) \underset{H_0}{\overset{H_1}{\gtrless}} \ln\eta \equiv \gamma. \tag{6.34}$$

It is straightforward to show from Eq. 6.31 and 6.32 that the maxima in Eq. 6.34 are achieved for

$$\begin{aligned} \hat{\mu} &= \frac{1}{N}\sum_{n=1}^{N} x_n \\ \hat{\mu}_0 &= \frac{1}{n_C}\sum_{n=1}^{n_C} x_n \\ \hat{\mu}_1 &= \frac{1}{N-n_C}\sum_{n=n_C+1}^{N} x_n. \end{aligned} \tag{6.35}$$

Substituting Eq. 6.35 into Eq. 6.31 and Eq. 6.32, the criterion in Eq. 6.34 now becomes

$$\max_{n_C}[n_C\hat{\mu}_0^2 + (N-n_C)\hat{\mu}_1^2 - N\hat{\mu}^2] \underset{H_0}{\overset{H_1}{\gtrless}} 2\sigma^2\gamma = \gamma'. \tag{6.36}$$

Eq. 6.36 implies that in order to find out whether or not a change occurs in $\mathbf{X}$, we need to calculate the value of the expression inside the bracket for all possible n_C from 1 to N, then compare its maximum value to a threshold. If the maximum in Eq. 6.36 is larger than the threshold, we say a change occurs and the point which gives the maximum is the position at which the change takes place. In practice, the threshold

is chosen empirically so that the prediction agrees with the known switching events on selected test data.

The choice of N, *i. e.*, the length of $\mathbf{X}$, is also critical. Since averaging is involved in calculating $\hat{\mu}$, larger N tends to increase the signal-to-noise ratio in the calculation and reduce the number of false alarms. On the other hand, we assume only one change can occur during the interval, and N should not exceed the shortest separation between two changes.

The calculation is then repeated by advancing $\mathbf{X}$ with a step Δ. Obviously, Δ should also be smaller than the shortest separation between two changes so that no change is missed. In practice, Δ is usually chosen to be $N/2$.

Once a change is detected, we can then determine whether it is a "upward" change or "downward" change by comparing the values of $\hat{\mu}_0$ and $\hat{\mu}_1$. The dwell time spent on each state can then be calculated as the duration between two consecutive, opposite change events.

6.3.2 Gate Dependence

Switching behavior similar to that shown in Fig. 6.11 has been observed at low frequencies when an SET is coupled to either a multi-junction trap [24], or defects behaving as bistable traps in the metal oxide or the substrate [108]. Similar behavior at higher frequencies has also been observed recently when an RF-SET is accidentally coupled to a defect-type trap [109]. Such a trap is normally modelled by having two sites with different coupling to the SET. When the potential near the trap is below a certain threshold, it is energetically favorable for the charge to stay in one of the sites, and vise versa. As a consequence, electrons can hop between the two sites back and force when the potential is around the threshold, hence introducing different offset

charges on the SET and causing switching behavior. As a result, switchings only occur near one gate voltage for a given trap. In contrast, for a real Coulomb-blockade device such as a quantum dot, electrons will tunnel on and off the dot whenever the energy of the N electron state is degenerate with that of the $N-1$ electron state. As a result, if the RF-SET is coupled to a quantum dot, switching behavior will appear periodically as the number of electrons in the dot is decreased one by one. Such divergent behavior (periodic vs. threshold) will allow us to determine whether the switchings we see in our system is caused by the dot or "junk effects" caused by charge traps.

To perform such a test, the voltage V_g on the dot gate G_d is incremented in 0.5 mV steps and a 16 millisecond record is captured by TDS7056 after the mixer at each voltage point. The number of switching events is then calculated using the "change" algorithm. Fig. 6.12(a) shows a typical result of the number of switching events as a function of V_g. Periodic behavior is clearly demonstrated with a period $\approx$ 15mV, in good agreement with the dot periodicity obtained from DC measurements in Fig. 6.10(d). Such periodic behavior unambiguously demonstrates that the observed switching events are indeed caused by the dot.

Another important feature in Fig. 6.12(a) is that the number of switching events shows large fluctuations. For example, representative records corresponding to data at points A and B are shown in Fig. 6.12(b) and (c). Not only are there more switching events at point A, but the dwell time the extra electron spends inside the dot is also much shorter. Such fluctuations have been predicted can arise from quantum interference inside the quantum dot. A detailed analysis of such behavior calls for further investigation. As V_g is increased, it indirectly closes the tunneling channels of the dot due to cross talk between the gate voltages. As a result, the peak height in Fig. 6.12(a) eventually diminishes.

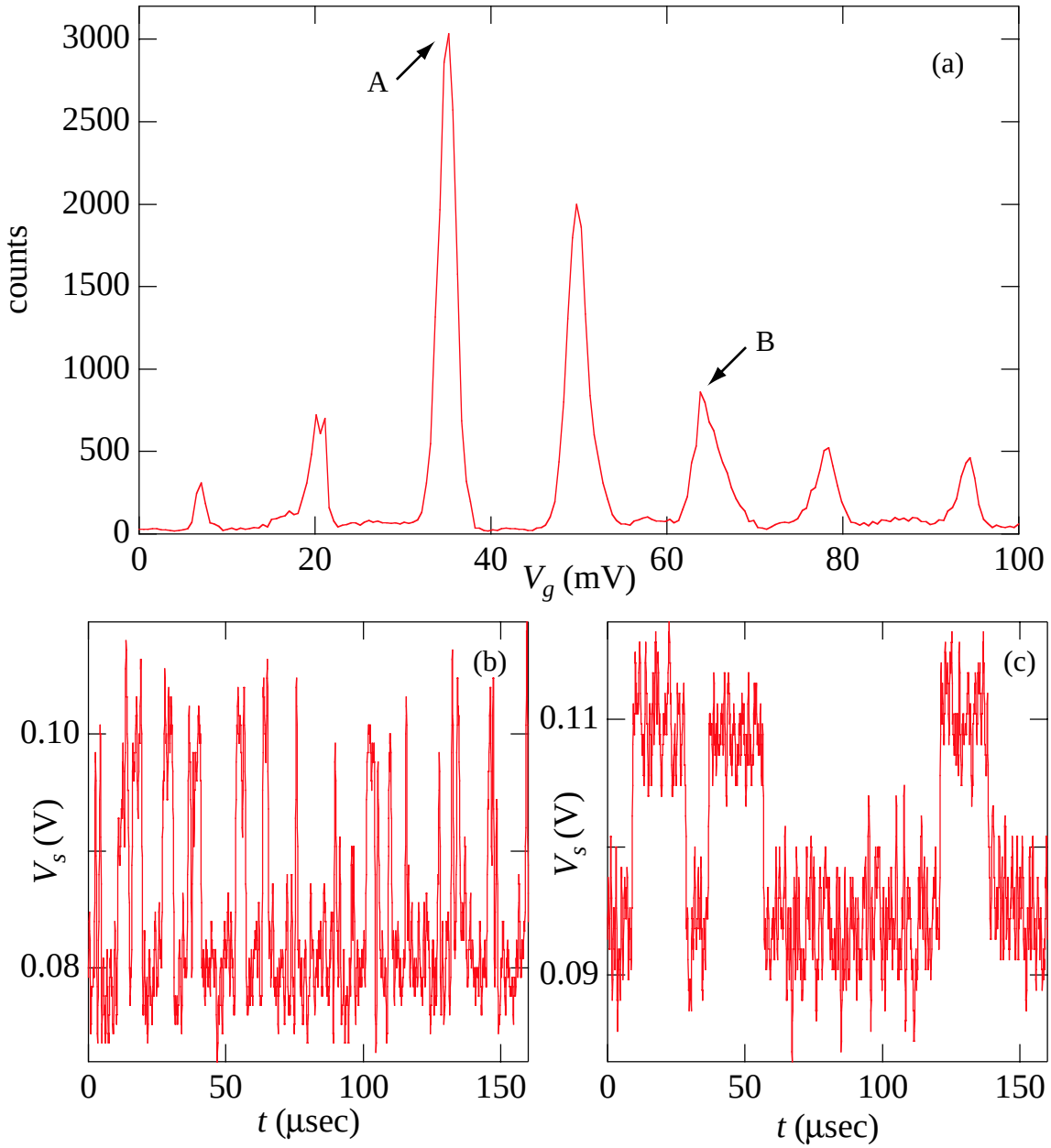

Figure 6.12: (a) Number of switching events as a function of V_g. (b),(c), representative data in real time record captured by the scope at points A and B in (a), respectively. There are fewer switching events at point B, with a longer dwell time.

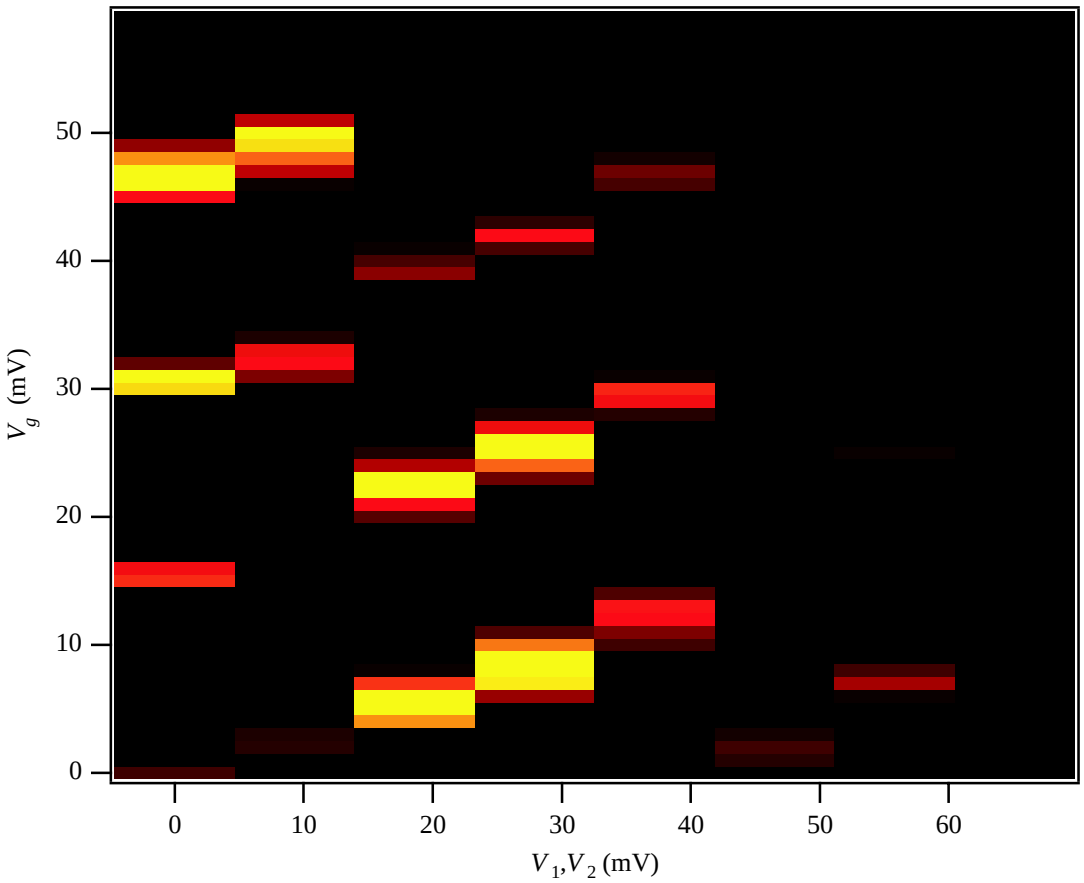

Figure 6.13: Evolution of the count peaks as a function of the gate voltages. V_1 and V_2 are increased by 9.3 mV after each V_g sweep.

Fig. 6.13 shows the result when the voltages V_1 and V_2 on the point contacts gates G_{R1} and G_{R1} are gradually increased. In this measurement, V_g is first swept by 50 mV so that at least 3 peaks are covered. V_1 and V_2 are then increased by 9.3 mV and the measurement is repeated. Since the point contact gates are also coupled to the dot, the dot offset charge, hence positions of the count peaks will be shifted from the previous sweeps. In fact, 3 extra electrons will be depleted from the dot as a result of the increase in V_1 and V_2, *i. e.*, the first peak in the second sweep corresponds to the fourth peak in the first sweep. Even so, the peaks in Fig. 6.13 demonstrate

well formed regularity. Such well organized behavior can only be caused by charge quantization in a quantum dot, instead of trapping effects. Once again, correlation between the peaks calls for further investigation.

6.3.3 "Bias" Dependence

The next step is to map out the Coulomb diamonds for the quantum dot in the V_{bias}, V_g plane, and to study the dwell time as a function of the current through the dot. We will concentrate on the region near the charge degeneracy point. Switching events should occur when the Coulomb blockade is lifted, *i. e.*, in the region outside the Coulomb diamonds in Fig. 2.3. In this measurement, we keep one side of the dot grounded, and sweep the voltage on the other side from -1 mV to $+1$ mV. After each sweep, V_g is incremented by 0.5 mV and the measurement is repeated. To our surprise, switching events were detected only along a single resonant line, as illustrated in Fig. 6.14(a), instead of in an area enclosed by two lines with opposite slopes. Furthermore, the sign of the slope does not change when the bias is applied on the opposite side of the dot, as illustrated in Fig. 6.14(b). The slope of the line is also insensitive to the conditions of the two point contacts. For example, Fig. 6.14(c) shows the result when V_1 is decreased by 50mV while V_2 increased by 30mV compared with conditions corresponding to Fig. 6.14(a). It shows roughly the same slope as in Fig. 6.14(a),(b). On the other hand, if the bias voltage is applied symmetrically on both the source and drain side of the dot, the switchings events do not show a bias dependence, as illustrated in Fig. 6.14(d). A line with the opposite slope was never observed.

Such discrepancies indicate that although the switching events occur at the charge degeneracy points of the dot, they do not correspond to tunneling through the dot.

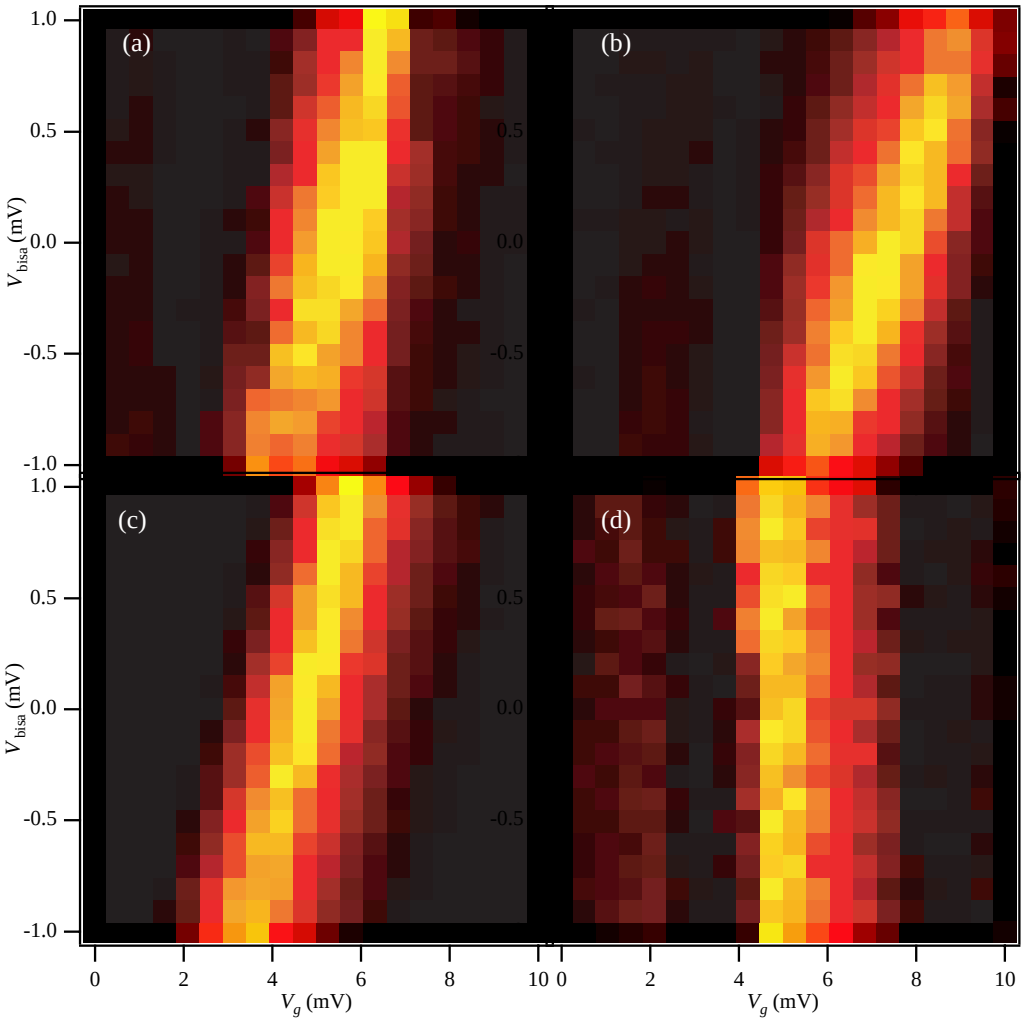

Figure 6.14: (a),(c) Counts (n) of switching events as a function of V_{bias} and V_g when the bias voltage is applied on the "source" side in Fig. 6.4, with different QPC formations in (a) and (c). (b) $n(V_{\text{bias}}, V_g)$ image when the bias voltage is applied on the "drain" side of the dot. (d) $n(V_{\text{bias}}, V_g)$ image when the bias voltage is applied symmetrically.

Rather, a single-electron box configuration was formed, in which electrons could only tunnel on and off the dot through the same barrier. This hypothesis is verified by the DC current measurements of the dot. On one hand, the a few thousand switching events near point A in Fig. 6.12(a) in a 16 ms time span should correspond to a DC current of a few tens of femtoamps, if the switching events are caused by electrons tunneling through the dot. Such a current should be just detectable by our current amplifier, which has a current sensitivity of ~ 7 fA. The measured DC current through the dot, however, decreases very fast as the point contacts are closed, and becomes undetectable well before the switching events appear. For example, the current through the dot becomes too small to detect when $V_1 = -.67$ V and $V_2 = -.76$ V, whereas switching events appear around $V_1 = -.97$ V and $V_2 = -1.07$ V, at which point the DC current through the dot is completely undetectable.

When such large gate voltages are applied, the two point contacts are so pinched-off that the QPCs are completely closed. The "bias" voltage applied on the source and drain of the dot then acts as an effective gate voltage. This hypothesis explains the fact that the slope of the resonant line does not change whether the voltage is applied on the source or drain. The capacitance of the "tunnel junctions" becomes insensitive to gate voltages for such large voltages as well [100], which explains the fact the slope of the line does not change much with V_1 and V_2. When opposite voltages are applied on the two sides of the dot, the induced offset charges cancel each other and changes in V_1 and V_2 have no effect on the switchings in the dot.

From the slope of the line and the capacitance to the dot from gate G_d, we can estimate the capacitance of the barriers to be ~ 20 aF, which is reasonable for such strongly closed barriers.

Tests on V_1 and V_2 indicate that they affect the switching counts equally, which suggests the actual tunneling barrier is on the left side of the dot in Fig. 6.4. Since the

voltage V_L on gates G_{L1} and G_{L2} was only -0.75 V to prevent the SET from arcing, we believe the actual tunnel barrier is formed between those gates, even though the channel was made longer to prevent such leaks from happening. If we estimate the capacitance of the barrier to be 100 aF, a typical count of 4000 switching events per 16 ms (*i. e.* dwell time $\tau = 8\,\mu$s,) indicates a tunneling resistance of 80 GΩ.

Nearly isolated dots have been of great interest lately [110, 111], due to predictions that quantum mechanical decoherence within them will be strongly affected by their internal single particle level spacing Δ [112]. For S6, the 2DEG sheet density is 1.3×10^{11} cm^{-2} and its mobility is 4.1×10^6 cm^{2}V^{-1}s^{-1} measured at 4 K. The dot has an estimated area $A \approx 200$ nm $\times$ 300 nm and contains roughly 80 electrons with an average level spacing $\Delta \approx 1/Ag_{2D} \approx 60\,\mu$eV; here $g_{2D} = m^*/\pi\hbar^2$ is the two dimensional density of states and m^* the effective mass of GaAs. Based on such estimations, the dot in S6 is in the quantum regime for which individual dot levels are important: $k_BT < \Delta < E_{Cd}$, where E_{Cd} is the charging energy of the dot. This is consistent with the data in Fig. 6.12, since the tunneling rate Γ between the dot and 2DEG is then expected to vary from peak to peak.

6.3.4 Line Shape Analysis

For such a single-electron box configuration, electron can only tunnel on or off the dot near a charge degeneracy point, and equilibrium properties of the dot is probed. By calculating the dwell time the excess electron spends on the dot from the real-time measurements, we can calculate directly charge occupational probabilities near a degeneracy point. Since the tunneling resistance is much larger than the resistance quantum R_K, lifetime broadening effects are negligible [17, 100], and the line shape of the occupational probabilities is expected to be a thermally broadened

Fermi function [25].

Here we follow the "master equation" approach developed by Beenakker [113]. In the limit $k_BT < E_C, \Delta$, where E_C is the charging energy of the dot and Δ is the discrete energy level spacing in the dot, we only need to consider whether or not an energy level E_p is occupied by an excess electron hence changing the total number of electrons on the dot from N to $N+1$. Here E_p is the ground level for the $N+1$ state. Steady state condition then requires the detailed balance equation

$$P_0\Gamma_p f(\Delta E) = P_1\Gamma_p(1 - f(\Delta E)) \tag{6.37}$$

to be satisfied. Here P_0 and P_1 are the probabilities that E_p is unoccupied and occupied, respectively, Γ_p is the attempt rate for an electron to tunnel on or off E_p through the junction and is determined by the internal properties of the dot,

$$f(\Delta E) = (1 + \exp(\Delta E/k_BT_{\text{eff}}))^{-1} \tag{6.38}$$

is the Fermi-Dirac distribution function, where

$$\Delta E = E_p + U(N+1) - U(N) - E_f \tag{6.39}$$

is the difference in free energy, E_f is the Fermi energy in the dot lead and T_{eff} is the effective electron temperature in the dot lead.

Since $P_0 f(\Delta E)$ is the probability that E_p is empty while a state in the lead that satisfies conservation of energy is occupied, the left term in Eq. 6.37 is simply the rate at which an electron tunnels onto the dot and changes the number of electrons to $N+1$. Similarly, the right term in Eq. 6.37 is the rate at which an electron tunnels off the dot and changes the number of electrons back to N. Eq. 6.37 thus has the straightforward physical meaning that the rate at which an electron tunnels onto the dot is the same as the rate an electron tunnels off the dot, which is required by the steady state condition.

P_0 and P_1 also need to satisfy the condition:

$$P_0 + P_1 = 1 \tag{6.40}$$

From Eq. 6.37 and Eq. 6.40, we easily obtain

$$\begin{aligned} P_0 &= 1 - f(\Delta E) \\ P_1 &= f(\Delta E) \end{aligned} \tag{6.41}$$

The average charge on the dot is then

$$ne = \frac{NeP_0 + (N+1)eP_1}{P_0 + P_1} = Ne + f(\Delta E)e \tag{6.42}$$

i. e., the line shape of the average charge follows a Fermi distribution, as observed earlier [25]. For simplicity, we choose zero of the potentials so that $E_p - E_f = 0$, and consider charge state $N = 0$,

$$\Delta E = E_p + U(N+1) - U(N) - E_f = (\frac{e}{2} - Q_0)\frac{e}{C_\Sigma} \tag{6.43}$$

where we have used the definition $U(N) = (Ne + Q_0)^2/2C_\Sigma$ and $Q_0 = C_g V_g$. The Fermi distribution in Eq. 6.42 is then

$$f(Q_0) = (1 + \exp((\frac{e}{2} - Q_0)\frac{e}{C_\Sigma}/k_B T_{\text{eff}}))^{-1} \tag{6.44}$$

Using the "change" routine, we are able to calculate the dwell time τ_1 for each excess electron, *i. e.*, the time during which the dot is in the $n = 1$ state; and the time τ_0 during which the dot is in the $n = 0$ state. The charge occupational probabilities are then:

$$\begin{aligned} P_0 &= \frac{<\tau_0>}{<\tau_0> + <\tau_1>} \\ P_1 &= \frac{<\tau_1>}{<\tau_0> + <\tau_1>} \end{aligned} \tag{6.45}$$

where $< \tau_0 >$ and $< \tau_1 >$ are the averages of the dwell times during one real time record (typically 16 ms).

Fig. 6.15(a) shows the evolution of P_0 and P_1 calculated according to Eq. 6.45 from the real time data as a function of the offset charge Q_0 near a charge degeneracy point. The insets of Fig. 6.15(a) show the real time record taken at $Q_0 = 0.39e$ and $Q_0 = 0.59e$, respectively. The insets demonstrate the fact that when $Q_0 < 0.5e$, the dot is more likely in the $n = 0$ state; while when $Q_0 > 0.5e$, the dot is more likely in the $n = 1$ state.

A fit based on Eq. 6.41 and Eq. 6.44 is also shown in Fig. 6.15(a) as the solid lines. The good agreement between the measured values and the fit verifies that the line shape of the charge occupational probabilities follows the thermally broadened Fermi distribution model. If we estimate the total capacitance of the dot $C_\Sigma \approx 200$ aF and use the measured value of $C_g = 10.7$ aF, the best fit then gives $T_{\text{eff}} \approx 430$ mK. Since the RF-SET is in close proximity to the dot lead, the rapidly varying RF signal in the SET will heat the lead. This effect is more pronounced if we believe the channel is on the left side of the dot, which lies just beneath the SET, and such an electron temperature is not unreasonable.

The detailed balance equation can be also be written as

$$\Gamma_c P_0 = \Gamma_e P_1 \tag{6.46}$$

where $\Gamma_c \equiv \tau_0^{-1}$, $\Gamma_e \equiv \tau_1^{-1}$ are the "capture" and "escape" transition rates for the excess electron, respectively. Comparing Eq. 6.46 with Eq. 6.37, we get

$$\begin{aligned} \tau_0^{-1} &= \tau^{-1} f(\Delta E) \\ \tau_1^{-1} &= \tau^{-1}(1 - f(\Delta E)) \end{aligned} \tag{6.47}$$

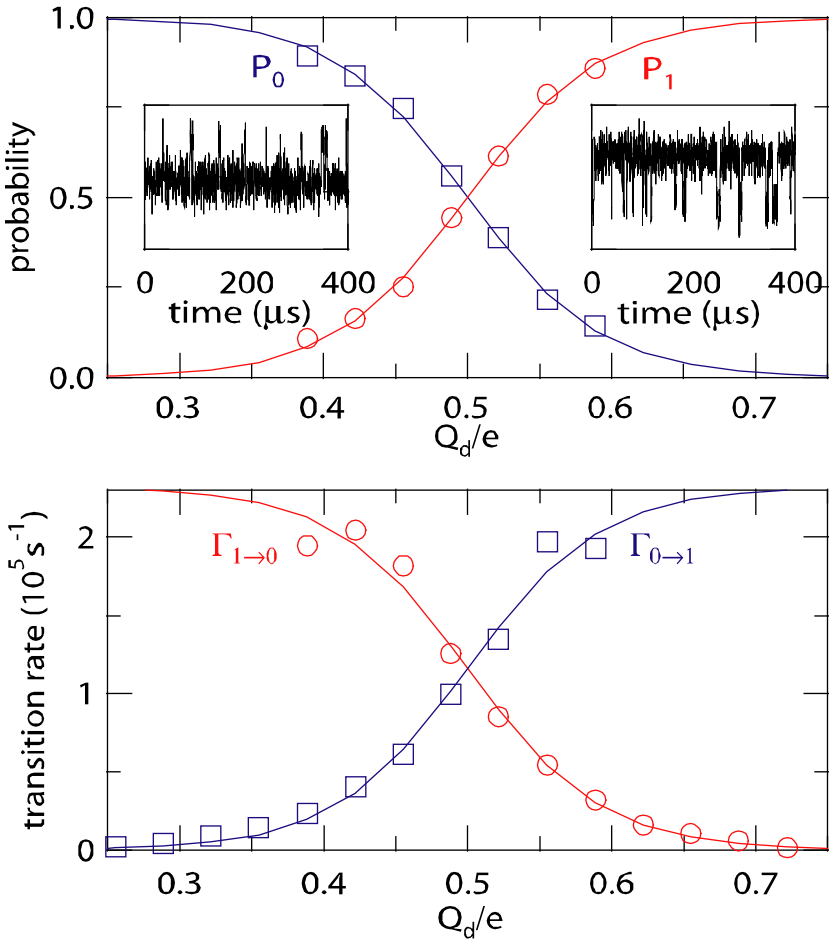

Figure 6.15: (a) Calculated occupational probabilities (blue squares: P_0, red circles: P_1) from the real time measurements as a function of Q_0 near a degeneracy point. The solid lines are a fit based on Fermi distribution. Left inset: real time data for $Q_0 = 0.39e$; right inset: real time data for $Q_0 = 0.59e$. (b) Evolution of the"capture" rate (blue squares) and "escape" rate (red circles) as a function of Q_0. The solid lines are calculated from Eq. 6.47, with no adjustable parameters used.

where $\tau \equiv \Gamma^{-1}$ is the effective dwell time. From Eq. 6.47

$$\Gamma = \tau^{-1} = \tau_0^{-1} + \tau_1^{-1} \tag{6.48}$$

i. e., the tunneling rate Γ can be calculated directly from the measured dwell times. Γ should remain constant around a degeneracy point, which we have also verified from the real time measurements. The average among the points in Fig. 6.15(a) gives $\Gamma = 2.32 \times 10^5\,\mathrm{s}^{-1}$.

Fig. 6.15(b) shows the rates $\Gamma_{1\to0} =< \tau_1 >^{-1}$ and $\Gamma_{0\to1} =< \tau_0 >^{-1}$ as a function of Q_0, together with calculations based on Eq. 6.47, using $\Gamma = 2.32 \times 10^5\,\mathrm{s}^{-1}$ and the same parameters determined in Fig. 6.15(a). Good agreement is once again achieved.

6.3.5 Spectrum Analysis

Near the charge degeneracy point, each "emission" and "capture" process is an independent event for the two-level system, and the switchings are characterized by a Poisson process [105, 106].

The spectral density of the measured signal S_V follows a Lorentzian form

$$S_V(\omega) = \frac{A^2\bar{\tau}}{4\pi[1 + (\omega\bar{\tau})^2]} \tag{6.49}$$

Fig. 6.16(a) shows the power spectrum of the RTS signal at representative peaks at different gate voltages. For frequencies below 1 KHz, the spectra show $1/f$ noise [32, 83, 107], most pronounced in the green curve. Above that frequency, the spectra are fit very well by Eq. 6.49, with the time constant $\bar{\tau}$ ranging from 171.5 μs to 1.2 μs.

The dwell times can also be studied in the time domain. Due to the random nature of the tunneling events, the dwell times spread over a broad range. In Fig. 6.16(b), we show the histogram of the dwell time on the $n = 1$ state τ_1 for the time domain data corresponding to the red curve in Fig. (a). The average of the dwell time

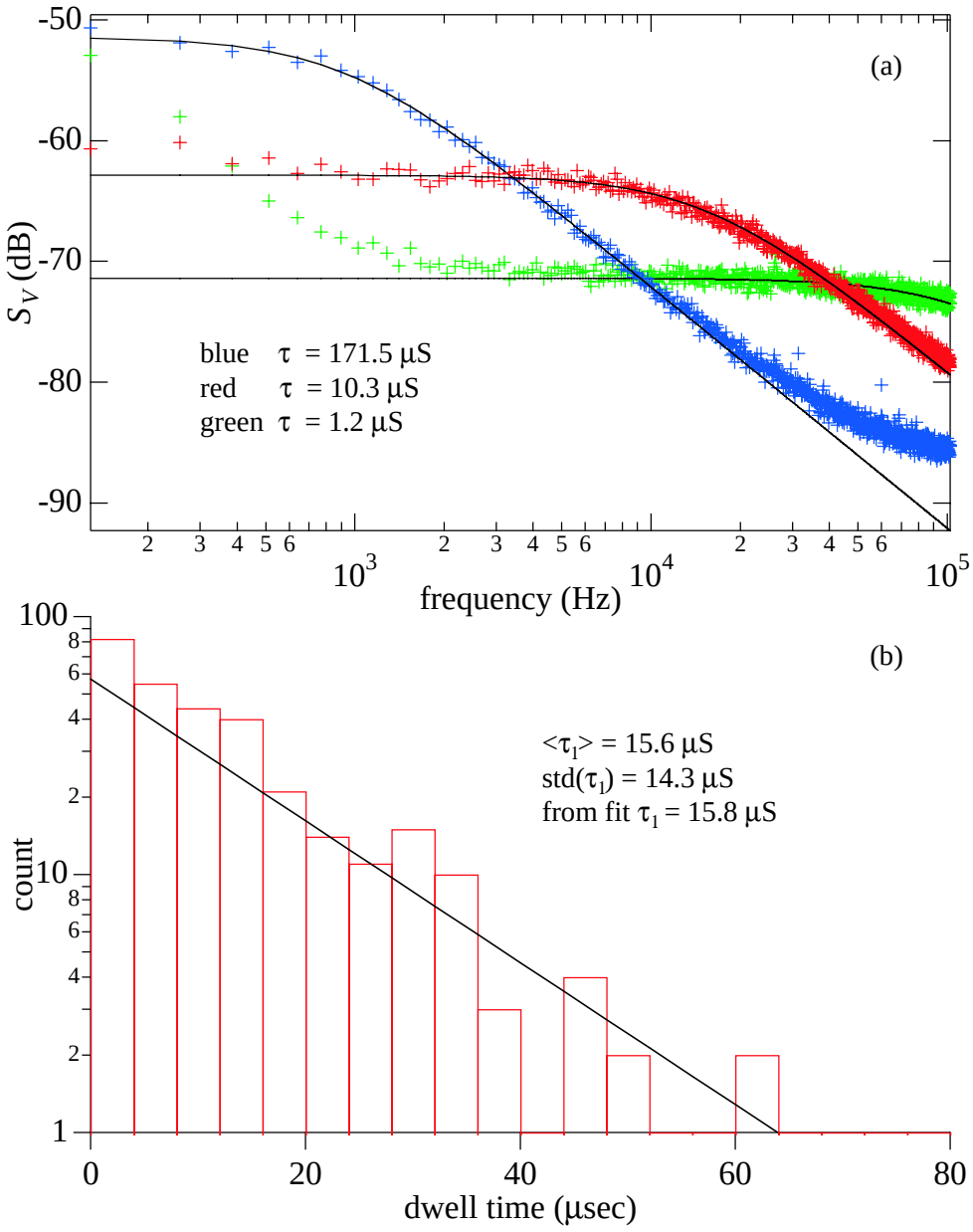

Figure 6.16: (a) Spectra (markers) of the signal at three representative peaks as the gate voltage is increased. The solid lines are least square fits using Eq. 6.49. (b) Histogram of the dwell time on the "1" state for switching events corresponding to the red curve in (a). The solid line is a fit based on an exponential decay.

$< \tau_1 >= 15.6\,\mu$s is practically the same as its deviation $\sigma(\tau_1) = 14.3\,\mu$s, characteristic of a Poisson process. The distribution of the counts can be fit with an exponential decay

$$\text{counts}(t) = C\exp(-t/\tau_{1f}) \tag{6.50}$$

which gives $\tau_{1f} = 15.8\,\mu$s, also nearly identical to $< \tau_1 >$. Similar results are achieved for the dwell time on the $n = 0$ state as well, with $\tau_{0f} \approx \sigma(\tau_0) \approx< \tau_0 >= 30.1\,\mu$s.

From Eq. 6.47, the effective dwell time

$$\tau = \frac{\tau_1\tau_0}{\tau_1 + \tau_0}. \tag{6.51}$$

Using the averaged τ_1 and τ_0 above, we obtain $\tau = 10.3\,\mu$s, which agrees very well with the time constant obtained from the spectrum analysis shown in Fig. 6.16.

6.4 Comparison of Tunneling Counts with Current

6.4.1 Improved Sample Design

The side channel between gates G_{L1} and G_{L2} in Fig. 6.4 prevents a direct comparison between the number of tunneling events and the DC current through the dot. A straightforward way to completely close this channel is to etch away the 2DEG completely on the left side of the dot. Fig. 6.17 shows an electron micrograph of a sample based on this improved design. Now the etched region must also be aligned well with the Au gates and an extra alignment process is involved in sample fabrication. The procedures are:

1. Fabrication of a set of Au alignment marks using e-beam lithography. These alignment marks will be used to align the Au gates to the etched region.

2. Alignment and exposure of the etch pattern.

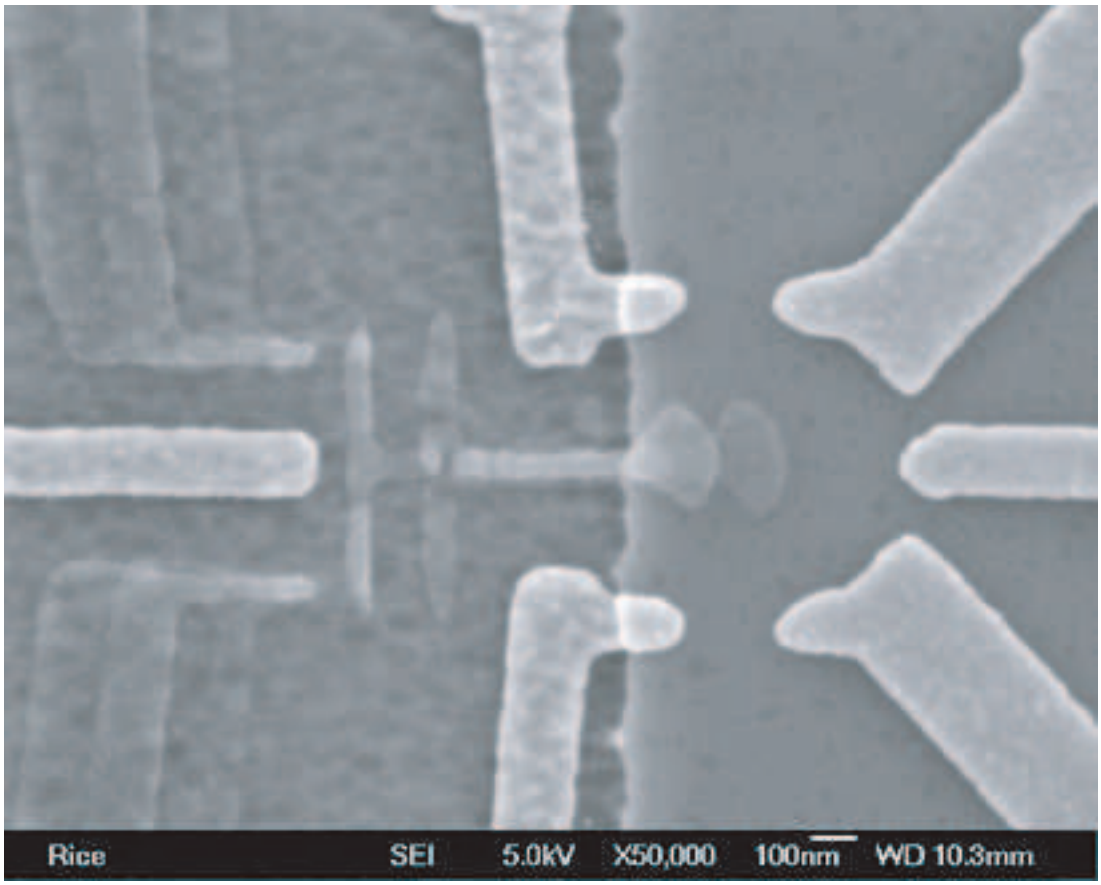

Figure 6.17: Electron micrograph for the improved sample design. The edge of the etched region is clearly visible. By completely etching the 2DEG away on the left side of the dot, the side channel is closely naturally.

3. Chemical etching.

4. Alloying Ohmic contacts to the 2DEG.

5. Fabrication of the Au gates and leads, together with another set of alignment marks. These alignment marks will be used to align the SET to the Au gates.

6. Fabrication of the SET.

The initial alignment in all these steps is performed by the "scratch mark" technique.

6.4.2 Characterization of the Sample

Fig. 6.18 shows the zero-bias conductance of the dot and the current through the SET measured simultaneously for a working sample (sample S7) with the new design. Very good dot behavior has been observed on this sample. Once again, doubly periodic behavior is observed on the current through the SET, indicating strong coupling between the SET and the dot.

The SET of sample S7 has a total normal-state resistance of $64\,\mathrm{K}\Omega$ and a charging energy $E_C = 237\,\mu\mathrm{eV}$. An unfortunate result of the higher junction resistance is that linear region similar to the one shown in Fig. 6.8 was not observed. The best charge sensitivity was achieved at the JQP region with $V_{\mathrm{SET}} \approx 600\,\mu\mathrm{V}$, and the optimal carrier wave frequency is $1113\,\mathrm{MHz}$, with an input amplitude $V_{\mathrm{rf}} = -71\,\mathrm{dBm}$, about $5\,\mathrm{dB}$ lower than that for sample S6.

Fig. 6.19(a) shows the spectrum around the carrier wave frequency with a $0.05e$ rms offset charge excitation, corresponding to a charge sensitivity $\delta q \approx 2.2 \times 10^{-5} e/\sqrt{\mathrm{Hz}}$. Although this charge sensitivity is comparable to the one obtained on sample S6, it is achieved only within a narrow region of the SET offset charge as illustrated in Fig. 6.19(b), and starts to decrease for charge modulation larger than $0.05e$ rms.

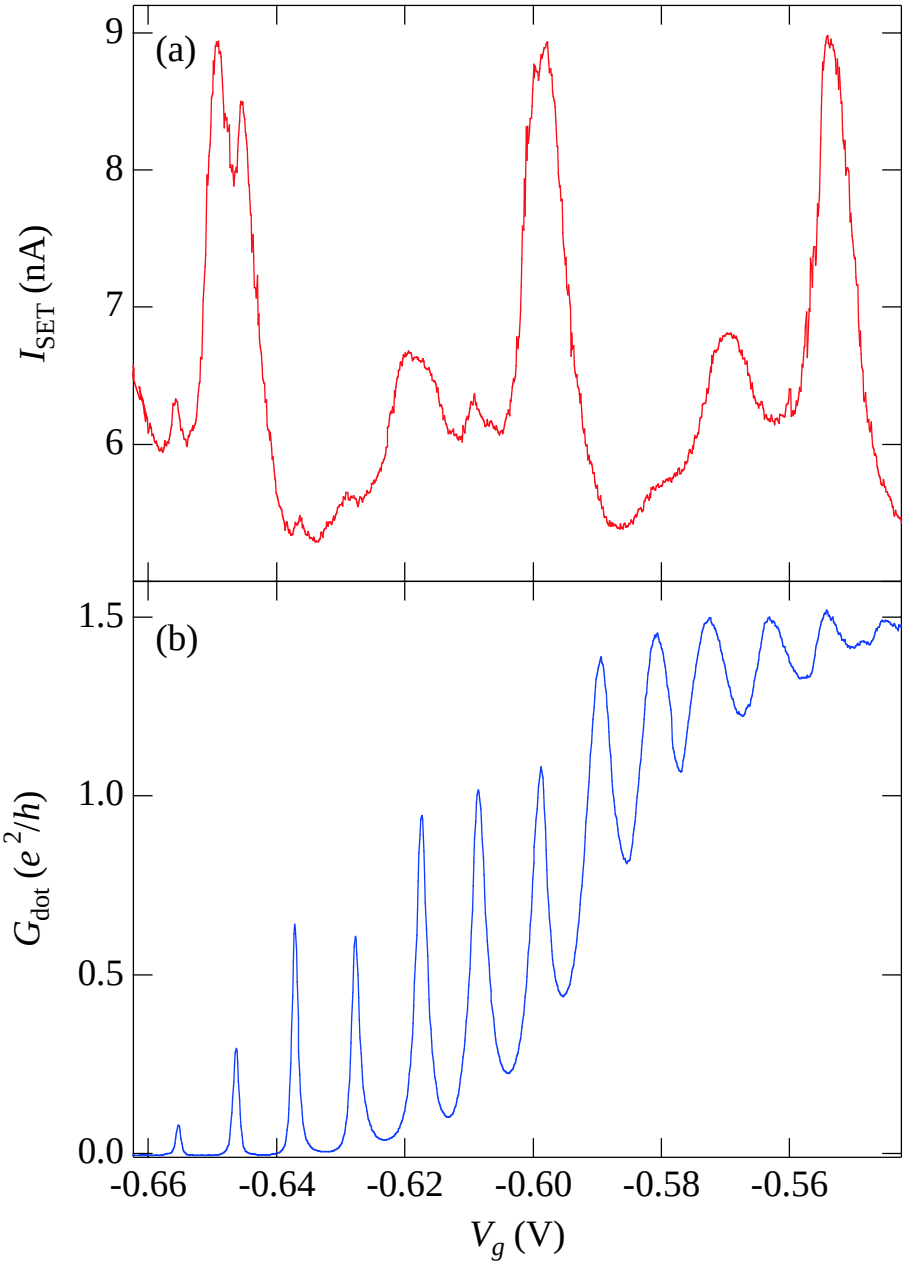

Figure 6.18: (a) Current through the SET as a function of gate voltage V_g. The small "bumps" at higher V_g are caused to changes in dot charge. The size of the bumps increases gradually as the total capacitance of the dot decreases. (b) Conductance of the dot taken simultaneously.

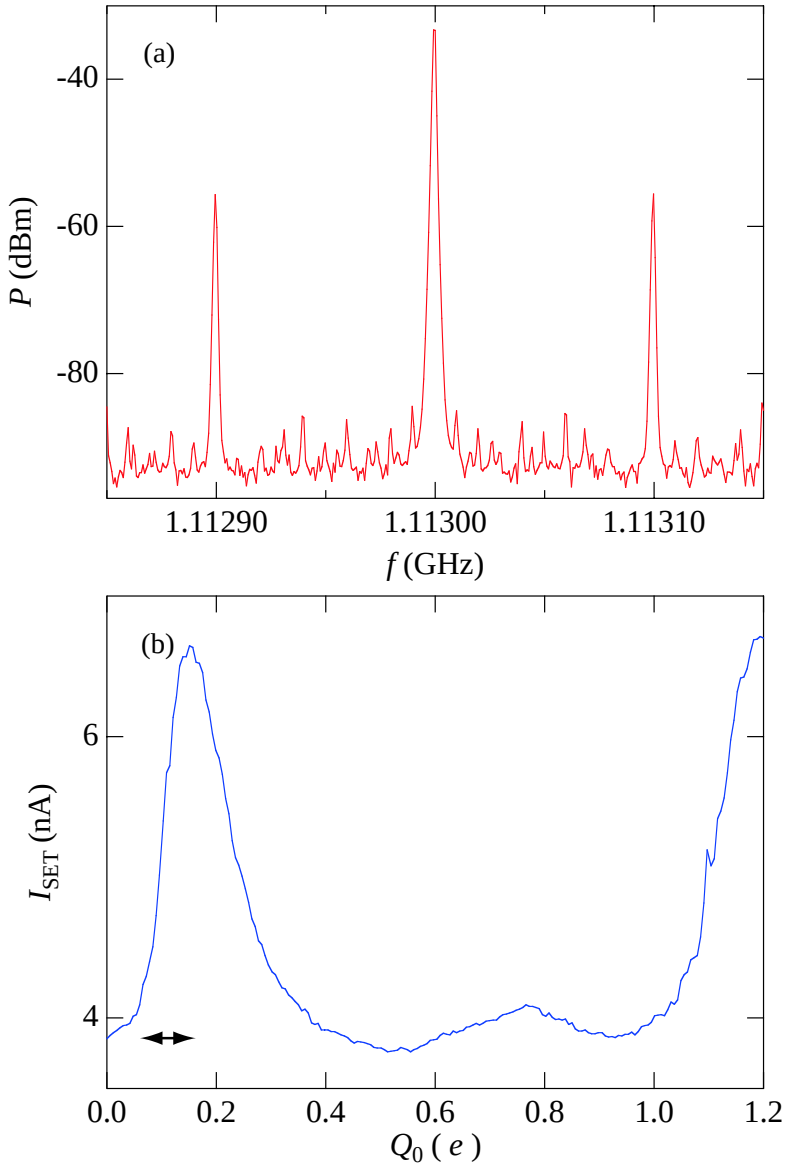

Figure 6.19: (a) Spectrum of the reflected RF signal around the carrier wave frequency for S7. The side peaks correspond to a $0.05e$ rms offset charge excitation. (b) Current through the SET vs. Q_0. High sensitivity can only be obtained within a limited region for S7 as indicated by the arrows.

This non-ideal behavior makes it hard to perform measurements for which the gate voltage is swept for a large range, or longthy measurements during which the SET offset charge may drift.

6.4.3 Real-Time Results

Switching events were again observed on S7. This time, unlike the case for S6, switching events were observed soon after the QPCs were closed, for which the voltages on the QPC gates were about 30 mV higher than the voltages corresponding to the measurement in Fig. 6.18. In contrast, for S6 the voltages on gates G_{R1} and G_{R2} were more than 200 mV higher. This verified our speculation that the side channel in S6 was open until the voltages were sufficiently high, and by completely etching the 2DEG away the problem is solved in S7.

The switching events now show a clear bias dependence, as illustrated in Fig. 6.20. In this measurement, the dot is symmetrically biased and a derived "current" I_C is calculated from the counts n of the switching events

$$I_C = ne/2\Delta t \tag{6.52}$$

and plotted as a function of V_{bias}. Here $\Delta t = 16$ ms is the time during which the record is taken. The factor 2 corresponds to the fact that when an electron tunnels through the dot, it first changes the charge state from N to $N+1$, then changes it back from $N+1$ to N, hence two switching events will be counted.

The absolute value of the current through the dot I_d measured at the same time is also plotted in Fig. 6.20 for comparison. Both I_C and I_d show a well defined gap, and the counts of switching events clearly capture the onset of the dot current, for both positive and negative biases. These agreements once again demonstrate that the switching events detected by the RF-SET is caused by electrons tunneling on/off

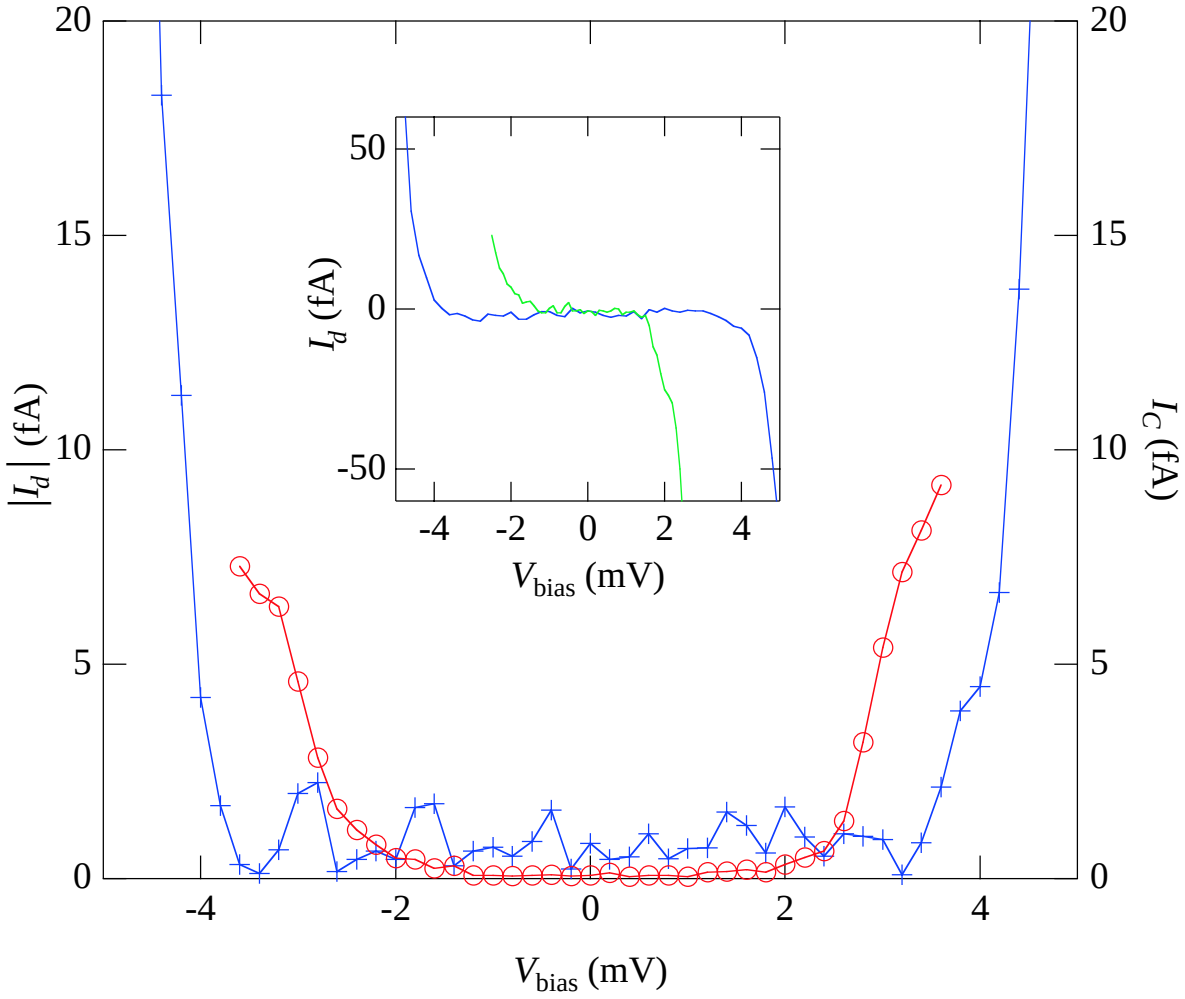

Figure 6.20: Induced current I_C (red curve) from the counts of the switching events as a function of the dot bias voltage. No adjustable parameters are used. The blue curve is the absolute value of the measured DC current I_d for comparison. Inset: blue curve, same I_d data as in the main figure; green curve, I_d measured at a different gate voltage for which the gap is narrower.

the dot.

The size of I_C also roughly agrees with the current measured by DC means, with no adjustable parameters involved. The fact the current induced by the counts is higher than that measured directly can be explained by the fact that electrons may tunnel backward through the same junction near a charge degeneracy point, as will be discussed in more detail below. Such backward tunneling events will not contribute to the current through the dot, but will be counted by the RF-SET.

We once again follow the master equation approach. The detailed balance equation is now:

$$P_0[\Gamma^\ell f(\Delta E^\ell) + \Gamma^r f(\Delta E^r)] = P_1[\Gamma^\ell(1 - f(\Delta E^\ell)) + \Gamma^r(1 - f(\Delta E^r))]. \tag{6.53}$$

Here P_0 and P_1 are once again the probabilities of the N electron and $N+1$ electron states of the dot, and Γ^ℓ and Γ^r are the attempt rates through the left and right junctions, respectively. ΔE^ℓ and ΔE^r differ from ΔE in Eq. 6.39 due to the added bias voltage:

$$\begin{aligned} \Delta E^\ell &= E_p + U(N+1) - U(N) - E_f + \kappa_1 eV \\ \Delta E^r &= E_p + U(N+1) - U(N) - E_f - \kappa_2 eV \end{aligned} \tag{6.54}$$

where $\kappa_i V$ is the effective voltage on junction i, as defined in Eq. 5.3.

From Eq. 6.53 and the normalization condition $P_0 + P_1 = 1$, we get:

$$\begin{aligned} P_0 &= \frac{\Gamma^\ell}{\Gamma^\ell + \Gamma^r}[1 - f(\Delta E^\ell)] + \frac{\Gamma^r}{\Gamma^\ell + \Gamma^r}[1 - f(\Delta E^r)] \\ P_1 &= \frac{\Gamma^\ell}{\Gamma^\ell + \Gamma^r} f(\Delta E^\ell) + \frac{\Gamma^r}{\Gamma^\ell + \Gamma^r} f(\Delta E^r) \end{aligned} \tag{6.55}$$

Note that if $\Gamma^r = 0$, *i. e.*, if one junction is completely closed, the dot becomes a single-electron box. Eq. 6.55 then reduces to Eq. 6.41, as expected.

The current through the dot is proportional to the forward tunneling rate minus the backward tunneling rate:

$$\begin{aligned} I &= e\Gamma^\ell P_0 f(\Delta E^\ell) - e\Gamma^\ell P_1[1 - f(\Delta E^\ell)] \\ &= e\frac{\Gamma^\ell\Gamma^r}{\Gamma^\ell + \Gamma^r}[f(\Delta E^\ell) - f(\Delta E^r)] \end{aligned} \tag{6.56}$$

where we have used the results of Eq. 6.55.

Consider the case in which the bias voltage is slightly smaller than the threshold for tunneling through the left junction, as illustrated in Fig. 6.21. In this case, $\Delta E^r \gg 0$ and $f(\Delta E^r)$ can be neglected. $\Delta E^\ell > 0$ and $f(\Delta E^\ell) < 1$, but $f(\Delta E^\ell)$ may not be neglected due to thermal activation. Eq. 6.56 now becomes

$$I \approx e\frac{\Gamma^\ell\Gamma^r}{\Gamma^\ell + \Gamma^r} f(\Delta E^\ell) = e\frac{\Gamma^\ell f(\Delta E^\ell)}{\Gamma^\ell + \Gamma^r}\Gamma^r \tag{6.57}$$

i. e., even though the dot is still inside the stable region for the N electron state, a thermally activated current can still flow through it.

The expected number of switching events due to the current can then be calculated from Eq. 6.52 to be:

$$n_I = 2\frac{\Gamma^\ell f(\Delta E^\ell)}{\Gamma^\ell + \Gamma^r}\Gamma^r \Delta t. \tag{6.58}$$

On the other hand, both forward tunneling and backward tunneling events will be detected by the RF-SET. The total number of tunneling events through the left junction is:

$$\begin{aligned} n_\ell &= \Gamma^\ell P_0 f(\Delta E^\ell) + e\Gamma^\ell P_1[1 - f(\Delta E^\ell)]\Delta t \\ &= \frac{\Gamma^\ell f(\Delta E^\ell)}{\Gamma^\ell + \Gamma^r}[2\Gamma^\ell(1 - f(\Delta E^\ell)) + \Gamma^r]\Delta t \end{aligned} \tag{6.59}$$

and the tunneling events through the right junction is:

$$\begin{aligned} n_r &= \Gamma^r P_0 f(\Delta E^r) + e\Gamma^r P_1[1 - f(\Delta E^r)]\Delta t \\ &\approx \frac{\Gamma^\ell f(\Delta E^\ell)}{\Gamma^\ell + \Gamma^r}\Gamma^r \Delta t \end{aligned} \tag{6.60}$$

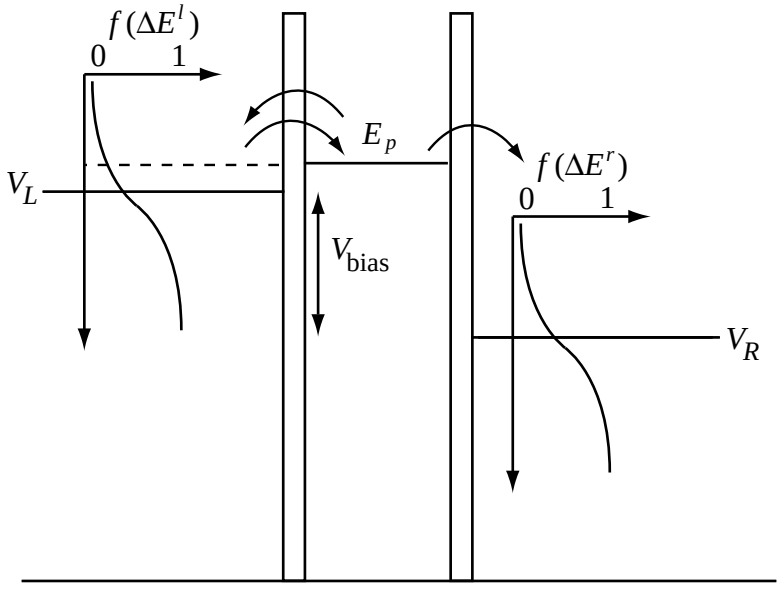

Figure 6.21: Schematic illustration of the condition in which the bias voltage V_{bias} is just below the threshold voltage. Thermally activated electrons can tunnel through the left junction. Once there, the electron can either tunnel back through the same junction or forward through the right junction.

where we have neglected terms involving $f(\Delta E^r)$. The total number of switching events is then:

$$n_C = n_\ell + n_r = 2\frac{\Gamma^\ell f(\Delta E^\ell)}{\Gamma^\ell + \Gamma^r}[\Gamma^\ell(1 - f(\Delta E^\ell)) + \Gamma^r]\Delta t \tag{6.61}$$

Comparing Eq. 6.61 with Eq. 6.58, the total tunneling events detected by the RF-SET is larger than that expected from the DC current by $\Gamma^\ell(1 - f(\Delta E^\ell))$, which is caused by backward tunneling through the left junction. This phenomena is schematically illustrated in Fig. 6.21.

If the two junctions of the dot are symmetric $\Gamma^\ell = \Gamma^r$, n_C can be twice as large as n_I, for both positive and negative biases. On the other hand, if $\Gamma^\ell \ll \Gamma^r$, n_C can be many times larger than n_I for positive bias, but roughly equal to n_I for negative bias.

For both cases, as the bias voltage increases, $f(\Delta E^{\ell})$ approaches 1 and n_C approaches n_I. In fact, $n_C \approx n_I$ soon after $\Delta E^{\ell} < 0$.

6.5 Discussion

In conclusion, we have successfully detected random-telegraph signals (RTS) using the RF-SET technique on all three samples (Samples S3, S6 and S7) for which both prerequisites that the RF-SET having high enough charge sensitivity and that a well-formed dot is present are satisfied. Gate dependence and bias dependence measurements unambiguously verified that the RTS are caused by electrons tunneling on or off the quantum dot.

Equilibrium properties of the dot have been studied when the dot is configured into a single electron box and electron can only tunnel through a single barrier. By calculating the number of switching events, a direct measurement of the tunneling rate Γ through the tunnel barrier is achieved, which is not possible by conventional DC measurements. Charge occupational probabilities around a charge degeneracy point have been calculated to follow a Fermi distribution, in agreement with a theory based on a two-level system. Spectrum analysis have indicated that tunneling in such a system is a Poisson process, agreeing with analysis of the distribution of the dwell times.

The significance of these results relates to decoherence in isolated dots, which (when arising from electron-electron interactions) has been predicted to vanish below a temperature T_c parametrically greter [112] than Δ; in our case $T_c \approx 1.9\Delta/k_B \approx 1.3\,\mathrm{K}$. A master equation was later used to address decoherence arising from other sources, *e. g.* external radiation [111]. Within this framework, the presence of decoherence (*i. e.*, inelastic transitions) within the QD would lead to tunneling between

multiple dot levels and the 2DEG. The probabilities P_{0i} and P_{1i} for each dot level i obey detailed balance. However, the total probabilities $\sum_i P_{0i}$ and $\sum_i P_{1i}$ for the dot to contain zero or one extra electron do not obey a simple relation, unless the tunneling rates Γ_i for all levels are identical. Thus, either we are observing charge fluctuations of a single quantum level that remains coherent for many microseconds, or multi-level tunneling dynamics can be described by a single time scale. While simplicity and agreement with recent theory [112] make the former interpretation attractive, we cannot rule out the latter without comparison to a more complete calculation of charge noise in QDs.

Non-equilibrium properties of the dot have also been studied by driving a current through the dot. The number of switching events rises sharply when the bias voltage approaches the threshold of the Coulomb-blockade region, agreeing with results of direct DC measurements. Unlike DC current, the electron counting measurement senses charge tunneling in both directions. As a result, a derived current based on electron counting is higher than the actual current near the threshold, but agrees better with the actual current at higher biases.

It is necessary to increase the gain of the RF-SET so that a higher signal-to-noise (S/N) ratio can be obtained to study the higher order processes such as temporal electron-electron correlation. A higher gain also means that the cut-off frequency of the low-pass filter (currently set at 1 MHz) can be increased, and faster signals can be detected. Such improvements will also make detection of larger currents possible allowing better comparison with measured DC currents.

As discussed in Section 6.2.2, by using superconducting on-chip inductors, the loss in our system may be minimized and the gain of the RF-SET may be increased by roughly a factor of 2. Even so, from Eq. 6.4, the total impedance Z_L of the LCR circuit is about $33\,\Omega$ using $L = 140\,\mathrm{nH}$, $C = 0.17\,\mathrm{pF}$ and $R_d = 25\,\mathrm{k}\Omega$, still not matched

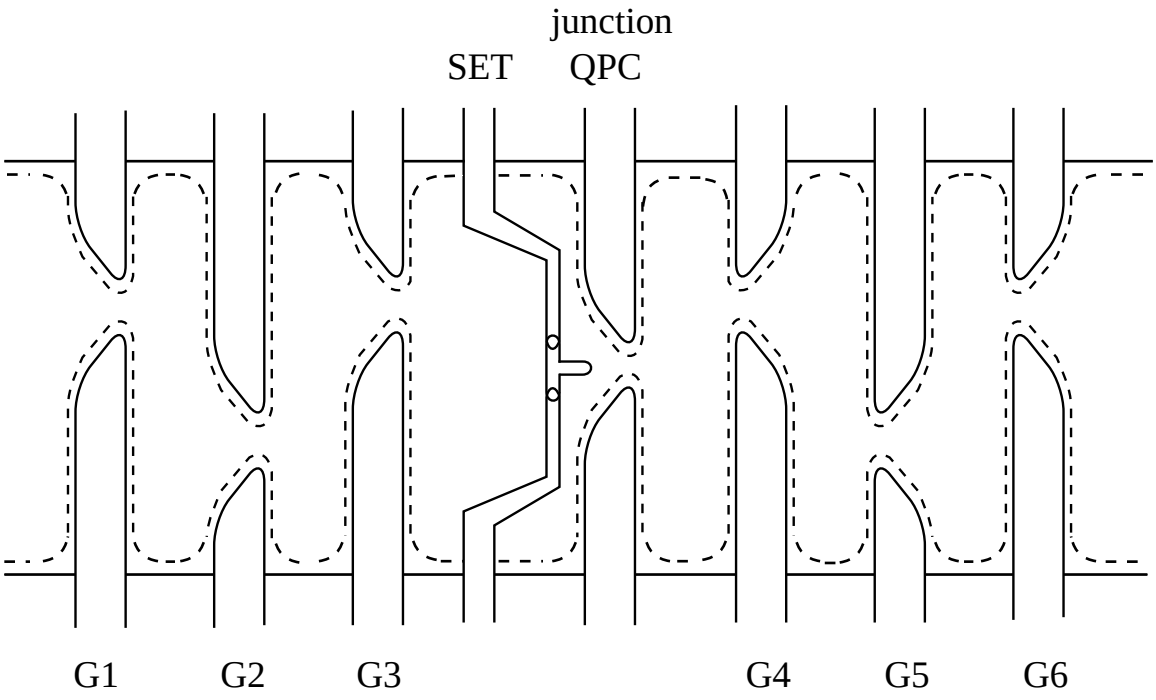

Figure 6.22: Schematic illustration of the setup for which an RF-SET is coupled to a single junction formed by a QPC. Six other QPCs serve as high impedance leads to the junction.

with the line impedance $Z_0 = 50\,\Omega$. However, if we insert a section of transmission line with a length 1/4 of that of the wavelength at ω_0, and impedance $Z_t = \sqrt{Z_L Z_0}$, it will match the resonant circuit perfectly with the line [81]. Such a "quarter-wave transformer" will effectively increase the gain of the RF-SET by another factor of $50/33 \approx 1.5$. More importantly, using the quarter-wave transformer technique, we can reduce L thereby increasing ω_0 and still achieve perfect matching with the $50\,\Omega$ line. By doing so, a higher bandwidth can be achieved. Such projects are currently underway in our group.

Finally, single-electron oscillations caused by periodic charging and discharging across a single junction at frequency $f = I/e$ have long been expected to occur [17] but

have yet to be observed experimentally. Such phenomena can only be observed when the junction is coupled to a high impedance environment so that charge equilibrium with the power supply will not be established quickly, as discussed in Chapter 4. DC measurements in which Coulomb blockade phenomena was observed have been performed for samples with long, highly resistive metal leads [114]. Such experiments are hard to carry out, since in order to make the resistance high, the lead has to be made very long; however, parasitic capacitance will then likely start to shunt the lead resistance at frequencies about a few GHz. On the other hand, from the results in Chapter 4, we find out that ballistic resistors (QPCs) act just as effectively in providing a high-impedance environment as diffusive resistors, *i. e.*, resistive metal leads. By coupling a QPC-type junction with a series of QPCs serving as a high-impedance environment, single-electron oscillations are expected to occur across the junction. Such charge oscillations can then be detected by an RF-SET. A sample design based on this concept is schematically illustrated in Fig. 6.22. In such a design, a 2DEG mesa is first etched, and six (or more) QPCs (the resistor QPCs) G1–G6 provide a high impedance environment for the tunnel junction. The voltage on the junction QPC is set higher so that its conductance $G \ll G_0$, whereas the voltages on the other QPCs are lower so that the no tunnel junction is formed by them. Ideally, the conductance of the resistor QPCs is at the last conductance plateau $G = 2G_0$, and may be achieved by adjusting a single voltage on all the gates. The RF-SET is then used to detect the charging and discharging across the junction QPC. Such a project is also currently underway in our group.

Bibliography

[1] B. L. Altshuler, P. A. Lee, and R. A. Webb (eds.), *Mesoscopic Phenomena in Solids* (Elsevier, Amsterdam, 1991).

[2] D. V. Averin and K. K. Likharev, in Grabert and Devoret [17], pp. 311–330.

[3] K. Yano, T. Ishii, T. Hashimoto, T. Kobayashi, F. Murai, and K. Seki, IEEE Trans. Electron Devices **41**, 1628 (1994).

[4] M. W. Keller, J. M. Martinis, N. M. Zimmerman, and A. H. Steinbach, Appl. Phys. Lett. **69**, 1804 (1996).

[5] D. L. Klein, R. Roth, A. K. L. Lim, A. P. Alivisatos and P. L. McEuen, Nature, **389** 699 (1997).

[6] S. J. Tans, M. H. Devoret, H. Dai, A. Thess, R. E. Smalley, L. J. Geerligs and C. Dekker, Nature, **386** 474 (1997).

[7] M. Bockrath, D. H. Cobden, P. L. McEuen, N. G. Chopra, A. Zettl, A Thess and R. E. Smalley, Science, **275** 1922 (1997).

[8] H. W. Ch. Postma, T. Teepen, Z. Yao, M. Grifoni, and C. Dekker, Science, **293** 76 (2001).

[9] J. Park, A. N. Pasupathy, J. I. Goldsmith, C. Chang, Y. Yaish, J. R. Petta, M. Rinkoski, J. P. Sethna, H. D. Abruña, P. L. McEuen and D. C. Ralph, Nature, **417** 722 (2002).

[10] W. Liang, M. P. Shores, M. Bockrath, J. R. Long and H. Park, Nature, **417** 725 (2002).

[11] A. O. Caldeira and A. J. Leggett, Phys. Rev. Lett. **46**, 211 (1981).

[12] A. O. Caldeira and A. J. Leggett, Ann. Phys. (NY) **149**, 374 (1983).

[13] A. J. Leggett, S. Chakravarty, A. T. Dorsey, M. P. A. Fisher, A. Garg, and W. Zwerger, Rev. Mod. Phys. **59**, 1 (1987).

[14] I. L. Chuang, R. Laflamme, P. W. Shor, and W. H. Zurek, Science **270**, 1633 (1995).

[15] J. I. Cirac, T. Pellizzari, and P. Zoller, Science **273**, 1207 (1996).

[16] T. Fujisawa, T. H. Oosterkamp, W. G. van der Wiel, B. W. Broer, R. Aguado, S. Tarucha, and P. Kouwenhoven, Science **282**, 932 (1998).

[17] H. Grabert and M. H. Devoret (eds.), *Single Charge Tunneling* (Plenum, New York, 1992).

[18] P. Delsing, K. K. Likharev, L. S. Kuzmin, and T. Claeson, Phys. Rev. Lett. **63**, 1180 (1989).

[19] T. Holst, D. Esteve, C. Urbina, and M. H. Devoret, Phys. Rev. Lett. **73**, 3455 (1994).

[20] R. L. Kautz and J. M. Martinis, Phys. Rev. B **42**, 9903 (1990).

[21] S. Washburn, R. A. Webb, R. G. Voss, and S. M. Faris, Phys. Rev. Lett. **54**, 2712 (1985).

[22] A. J. Rimberg, T. R. Ho, Ç. Kurdak, J. Clarke, K. L. Campman, and A. C. Gossard, Phys. Rev. Lett. **78**, 2632 (1997).

[23] E. Ben-Jacob and Y. Gefen, Physics Lett. **108A**, 289 (1985).

[24] P. D. Dresselhaus, L. J, Siyuan Han, J. E. Lukens, and K. K. Likharev, Phys. Rev. Lett. **72**, 3226 (1994).

[25] D. Berman, N. B. Zhitenev, R. C. Ashoori, and M. Shayegan, Phys. Rev. Lett. **82**, 161 (1999).

[26] Y. M. Blanter and M. Büttiker, Physics Reports **336**, 1–166 (2000).

[27] L. S. Levitov and G. B. Lesovik, JETP Lett. **55**, 555 (1992).

[28] L. S. Levitov, H. Lee and G. B. Lesovik, J. Math. Phys. **37**, 4845–4866 (1996).

[29] A. Shnirman and G. Schön, Phys. Rev. B **57**, 15400 (1998).

[30] D. Loss and D. P. DiVincenzo, Phys. Rev. A **57**, 120 (1998).

[31] J. J. Harris, J. A. Pals, and R. Woltjer, Rep. Prog. Phys. **52**, 1217 (1989).

[32] R. J. Schoelkopf, P. Wahlgren, A. A. Kozhevnikov, P. Delsing, and D. E. Prober, Science **280**, 1238 (1998).

[33] T. A. Fulton and G. J. Dolan, Phys. Rev. Lett. **59**, 109 (1987).

[34] K. K. Likharev, IBM J. Res. Dev. **32**, 144 (1988).

[35] T. A. Fulton, D. J. Bishop, L. N. Dunkleburger, and G. J. Dolan, Phys. Rev. Lett. **63**, 1307 (1989).

[36] A. M. van den Brink, A. A. Odintsov, P. A. Bobbert, and G. Schön, Z. Phys. B **85**, 459 (1991).

[37] V. Ambegaokar and A. Baratoff, Phys. Rev. Lett. **10**, 486 (1963).

[38] M. T. Tuominen, J. M. Hergenrother, T. S. Tighe, and M. Tinkham, Phys. Rev. Lett. **69**, 1997 (1992).

[39] A. Amar, D. Song, C. J. Lobb, and F. C. Wellstood, Phys. Rev. Lett. **72**, 3234 (1994).

[40] J. Siewert and G. Schön, Phys. Rev. B **54**, 7421 (1996).

[41] R. J. Fitzgerald, S. J. Pohlen, and M. Tinkham, Phys. Rev. B **57**, R11 073 (1998).

[42] Y. Nakamura, C. D. Chen, and J. S. Tsai, Phys. Rev. B **53**, 8234 (1996).

[43] M. A. Herman and H. Sitter, *Molecular Beam Epitaxy: Fundamentals and Current Status* (Springer-Verlag, Berlin, 1989).

[44] T. J. Thornton, M. Pepper, H. Ahmed, D. Andrews, and G. J. Davies, Phys. Rev. Lett. **56**, 1198 (1986).

[45] H. Z. Zheng, H. P. Wei, D. C. Tsui, and G. Weimann, Phys. Rev. B **34**, 5635 (1986).

[46] B. J. van Wees, H. V. Houten, C. W. J. Beenakker, J. G. Williamson, L. P. Kouwenhoven, D. van der Marel, and C. T. Foxon, Phys. Rev. Lett. **60**, 848 (1988).

[47] D. A. Wharam, T. J. Thornton, R. Newbury, M. Pepper, H. Ahmed, J. E. F. Frost, D. G. Hasko, D. C. Peacock, D. A. Ritchie, and G. A. C. Jones, J. Phys. Chem. **21**, L209 (1988).

[48] H. Ehrenreich and D. Turnbull (eds.), *Solid State Physics: Semiconductor Heterostructures and Nanostructures* (Academic Press Inc, San Diego, 1991).

[49] G.-L. Ingold and Yu. V. Nazarov, in Grabert and Devoret [17], pp. 21–107.

[50] M. H. Devoret, D. Esteve, H. Grabert, G.-L. Ingold, H. Pothier, and C. Urbina, Phys. Rev. Lett. **64**, 1824 (1990).

[51] S. M. Girvin, L. I. Glazman, M. Jonson, D. R. Penn, and M. D. Stiles, Phys. Rev. Lett. **64**, 3183 (1990).

[52] G. J. Dolan, Appl. Phys. Lett. **31**, 337 (1977).

[53] R. Williams, *Modern GaAs Processing Methods* (Artech House, Inc, 1990).

[54] S. Mackie and S. P. Beaumont, Solid State Technol. **28**, 117 (1985).

[55] M. J. Rooks, S. Wind, P. McEuen, and D. E. Prober, J. Vac. Sci. Technol. B **5**, 318 (1987).

[56] R. C. Richardson and E. N. Smith (eds.), *Experimental Techniques in Condensed Matter Physics at Low Temperatures* (Addison-Wesley Publishing Company, Reading, Massachusetts, 1988).

[57] J. M. Martinis, M. H. Devoret, and J. Clarke, Phys. Rev. B **35**, 4682 (1987).

[58] J. M. Martinis and M. Nahum, Phys. Rev. B **48**, 18 316 (1993).

[59] J. M. Hergenrother, M. T. Tuominen, J. G. Lu, D. C. Ralph, and M. Tinkham, Physica B **203**, 327 (1994).

[60] J. M. Hergenrother, J. G. Lu, M. T. Tuominen, and M. Tinkham, Phys. Rev. B **51**, 9407 (1995).

[61] S. Chakravarty, G. L. Ingold, S. Kivelson, and A. Luther, Phys. Rev. Lett. **56**, 2303 (1986).

[62] M. P. A. Fisher, Phys. Rev. B **36**, 1917 (1987).

[63] P. Joyez, P. Lafarge, A. Filipe, D. Esteve, and M. H. Devoret, Phys. Rev. Lett. **72**, 2458 (1994).

[64] Yu. Makhlin, G. Schön, and A. Shnirman, Nature **398**, 305 (1999).

[65] Y. Nakamura, Yu. A. Pashkin, and J. S. Tsai, Nature **398**, 786 (1999).

[66] J. E. Mooij, T. P. Orlando, L. Levitov, L. Tian, C. H. van der Wal, and S. Lloyd, Science **285**, 1036 (1999).

[67] D. Vion, A. Aassime, A. Cottet, P. Joyez, H. Pothier, C. Urbina, D. Esteve, and M. H. Devoret, Science **296**, 886 (2002).

[68] A. Shnirman, G. Schön, and Z. Hermon, Phys. Rev. Lett. **79**, 2371 (1997).

[69] Yu. Makhlin, G. Schön, and A. Shnirman, Rev. Mod. Phys. **73**, 357 (2001).

[70] R. Aguado and L. P. Kouwenhoven, Phys. Rev. Lett. **84**, 1986 (2000).

[71] S. L. Sohdhi, S. M. Girvin, J. P. Carini, and D. Shahar, Rev. Mod. Phys. **69**, 315 (1997).

[72] N. Mason and A. Kapitulnik, Phys. Rev. Lett. **82**, 5341 (1999).

[73] A. Kapitulnik, N. Mason, S. A. Kivelson, and S. Chakravarty, Phys. Rev. B **63**, 125322 (2001).

[74] W. Lu, A. J. Rimberg, and K. D. Maranowski, Appl. Phys. Lett. **81**, 4976 (2002).

[75] A. J. Rimberg and W. Lu, cond-mat/0205382.

[76] J. B. Kycia, J. Chen, R. Therrien, Ç. Kurdak, K. L. Campman, A. C. Gossard, and J. Clarke, Phys. Rev. Lett. **87**, 017002 (2001).

[77] W. Lu, A. J. Rimberg, K. D. Maranowski, and A. C. Gossard, Appl. Phys. Lett. **77**, 2746 (2000).

[78] W. Lu, K. D. Maranowski, and A. J. Rimberg, Phys. Rev. B **65**, 060501(R) (2002).

[79] G.-L. Ingold, P. Wyrowski, and H. Grabert, Z. Phys. B **85**, 443 (1991).

[80] A. A. Odintsov, G. Falci, and G. Schön, Phys. Rev. B **44**, 13 089 (1991).

[81] D. M. Pozar, *Microwave Engineering, 2nd Ed.* (John Wiley & Sons, New York, 1998)

[82] L. S. Kuzmin, Yu. V. Nazarov, D. B. Haviland, P. Delsing, and T. Claeson, Phys. Rev. Lett **67**, 1161 (1991).

[83] M. W. Keller, J. M. Martinis, and R. L. Kautz, Phys. Rev. Lett **80**, 4530 (1998).

[84] G. Schön, in *Quantum Transpor and Dissipation* (Willey-VCH, Weinheim, Germany, 1998), pp. 149-212.

[85] F. K. Wilhelm, G. Schön, and G. T. Zimányi, Phys. Rev. Lett. **87**, 136802 (2001).

[86] H. Graberg, G.-L. Ingold, and B. Paul, Europhys. Lett. **44**, 360 (1998).

[87] H. Graberg and G.-L. Ingold, Supperlattices and Microstruct. **25**, 915 (1999)

[88] R. E. Collin, *Foundation for Microwave Engineering* (McGraw-Hill, New York, 1992).

[89] E. H. Visscher, S. M. Verbrugh, J. Lindeman, P. Hadley, and J. E. Mooij, Appl. Phys. Lett. **66**, 305 (1995).

[90] V. A. Krupenin, D. E. Presnov, M. N. Savvateev, H. Scherer, A. B. Zorin, and J. Niemeyer, J. Appl. Phys. **84**, 3212 (1998).

[91] Sh. Kogan, *Electronic Noise and Fluctuations in Solids* (Cambridge University Press, Cambridge, United Kingdom, 1996).

[92] T. M. Eiles and J. M. Martinis, Phys. Rev. B **50**, 627 (1994)

[93] T. M. Eiles, J. M. Martinis, and M. H. Devoret, Phys. Rev. Lett. **70**, 1862 (1993).

[94] M. Covingon, M. W. keller, R. L. Kautz, and J. M. Martinis, Phys. Rev. Lett. **84**, 5192 (2000).

[95] D. V. Averin and V. Ya. Aleshkin, Pis'ma Zh. Eksp. Teor. Fiz. **50**, 331 (1989) [JETP Lett. **50**, 367 (1989)].

[96] V. Ya. Aleshkin and D. V. Averin, Physica B **165&166**, 949 (1990).

[97] P. Hadley, E. Delvingne, E. H. Visscher, S. Lähteenmäki, and J. E. Mooij, Phys. Rev. B **58**, 15 317 (1998).

[98] D. S. Duncan, C. Livermore, R. M. Westervelt, K. D. Maranowski, and A. C. Gossard, Appl. Phys. Lett. **74**, 1045 (1999).

[99] A. N. Korotkov, and M. A. Paalanen, Appl. Phys. Lett **74**, 4052 (1999).

[100] E. B. Foxman, P. L. McEuen, U. Meirav, N. S. Wingreen, Y. Meir, P. A. Belk, N. R. Belk, M. A. Kastner, and S. J. Wind, Phys. Rev. B **47**, 10020 (1993).

[101] N. Miyakawa, P. Guptasarma, J. F. Zasadzinski, D. G. Hinks, and K. E. Gray, Phys. Rev. Lett. **80**, 157 (1998).

[102] K. A. Matveev, M. Gisselfält, L. I. Glazman, M. Jonson, and R. I. Shekhter, Phys. Rev. Lett. **70**, 2940 (1993).

[103] P. Lafarge, P. Joyez, D. Esteve, C. Urbina, and M. H. Devoret, Phys. Rev. Lett. **70**, 994 (1993).

[104] M. Basseville and I. V. Nikiforov, *Detection of Abrupt Changes* (Prentice Hall, Englewood Cliffs, New Jersey, USA, 1993).

[105] S. Machlup, J. Appl. Phys. **25**, 341 (1954).

[106] M. J. Kirton and M. J. Uren, Adv. Phys. **38**, 367 (1989).

[107] B. Starmark, T. Henning, T. Claeson, and P. Delsing, J. Appl. Phys. **86**, 2132 (1999).

[108] Miha Furlan and Sergey V. Lotkhov, cond-mat/0212184.

[109] Toshimasa Fujisawa and Yoshiro Hirayama, Appl. Phys. Lett. **77**, 543 (2000).

[110] J. A. Folk, C. M. Marcus and J. S. Harris, Phys. Rev. Lett. **87**, 206802 (2001).

[111] E. Eisenberg, K. Held and B. L. Altshuler, Phys. Rev. Lett. **88**, 36801 (2002).

[112] B. L. Altshuler, Y. Gefen, A. Kamenev and L. S. Levitov, Phys. Rev. Lett. **78**, 2803 (1997).

[113] C. W. J. Beenakker, Phys. Rev. B **44**, 1646 (1991).

[114] A. N. Cleland, J. M. Schmidt, and John Clarke, Phys. Rev. Lett. **64**, 1565 (1990).